Indirect Wave Load Estimates Using Operational Modal Analysis

Michael Vigsø

PhD Dissertation

Department of Engineering
Aarhus University
Denmark

ISBN: 978-87-7507-473-0
DOI: 10.7146/aul.372

Indirect Wave Load Estimates Using Operational Modal Analysis

A thesis submitted to the
Faculty of Science and Technology at Aarhus University
for the degree of Doctor of Philosophy.

by
Michael Vigsø
December 14, 2019

Thesis Submitted:	December 14$^{\text{th}}$, 2019
Ph.D. Supervisors:	Prof. Christos Georgakis *Department of Engineering, Aarhus University* Prof. Rune Brincker *Department of Civil Engineering, DTU*
Ph.D. Committee:	Associate Prof. Steffen Petersen (chair) *Department of Engineering, Aarhus University* Prof. Michel Benoit *Institut de Recherche sur les Phenomenes Hors Equilibre, École Centrale de Marseille, France* Prof. Anders Brandt *Department of Technology and Innovation, SDU*
Defence date:	March 6$^{\text{th}}$, 2020 at Navitas, Aarhus, Denmark
Revision date:	April 2020
Revision comments:	*Paper VIII was published in the proceedings of the OMAE 2020 conference as opposed to EURODYN as stated in the original dissertation.*

Preface

After graduating as a civil engineer from Aalborg University in 2013, I moved to Bergen in Norway to get hands-on experience with the offshore industry. I was employed at the contracting company DOF Subsea, which delivers vessel-based support to offshore installations. The primary part of the work being performed involved commissioning, maintenance and decommissioning - most of which was done subsea, using remotely operated vehicles, also known as ROVs. After spending many days offshore in the freezing winds of the North Sea, I decided to return to the study desk once again. Certainly, the drop in crude oil price, leading to mass layoff, fueled my eagerness to pursue my academic endeavors. However, it was clear that the study should extend the experience gathered and thus be related to offshore engineering. So after three great years with the Norwegians, I returned to Denmark and began my Ph.D. study under the supervision of Christos Georgakis and Rune Brincker.

The Ph.D. study is outlined by the Danish Hydrocarbon Research and Technology Centre (DHRTC), also known as the Centre for Oil and Gas. The centre was established in 2014 as an outcome of an agreement between the DUC and the Danish government. As part of the long-term agreement for exploration and production in Denmark, the DUC donated one billion Danish kroner to research with the purpose of increasing the production in Denmark. This Ph.D. project falls under the category of "Structural Integrity and Pipeline Technology" which concerns lifetime extensions of existing structures.

This thesis is generated as "papers based" under requirements by the Graduate School of Science and Technology (GSST) for the fulfillment of the Ph.D. degree. In accordance with GSST rules, parts of this thesis were also used in the progress report for the qualifying examination.

Michael Vigsø,
Aarhus, December 14, 2019.

Acknowledgements

First and foremost, I wish to thank my two dedicated supervisors; Professor Christos Georgakis (AU) and Professor Rune Brincker (DTU) who have arranged the funding and outlined the scope of this project. They have welcomed me into the research group of structural dynamics and monitoring at Aarhus University and maintained their undivided optimism and support throughout the project. For his participation and comments on my midterm evaluation, I also wish to thank Professor Holger Koss (DTU).

Regards should also be sent abroad to Professor Carlos Ventura (UBC) who invited me to stay at the University of British Columbia in Vancouver, Canada for a period of three months in 2018. I also wish to thank Eddy Dascotte and Jim Steedman, from Dynamic Design Solutions, who introduced me to the concepts of model updating using femtools. During a period of one week in 2017, they arranged for a training program at their home in Fullerton, LA.

I will like to address my sincere thanks to my fellow Ph.D. students at Aarhus University, without whom this work probably would never have ended. In random order: Thomas Kabel, Marius Tarpø, Julie Kristoffersen, Jannick Hansen, Peter Olsen, Martin Juul, and Anders Skafte. From your support, discussions and in general colorful personalities, you guys have made this worth the effort.

Acknowledgments should be given to the kind staff at Aarhus University, in particular, Jørgen Holm, who on several occasions has helped with building physical models used for the thesis. Also the staff that I have interacted with at foreign research institutions should not be forgotten either. Here I should mention Newcastle University and LASIF in Marseille.

I acknowledge the Danish Hydrocarbon Research and Technology Centre (DHRTC) for their funding and keeping me in touch with the industry. Private funding, which has sweetened the study period and allowed for conference participation at exotic places, should not be left unmentioned either. Here,

arranged by their generosity: Foundation Idella, Thriges Fond, Frimondts Fond, GSST grant, Augustinus Fonden, Knud Højgaards Fond, Rudolph Als Fondet, Otto Mønsteds Fond, Oticon Fonden, Brorsons Rejselegat, Tranes Fond, Richters Fond, Haynmans Fond, and Familien Hede Nielsens Fond.

Finally, I am grateful for the patience and understanding from my wife and daughter, especially during the finalization of this work.

Abstract

Wave loading of offshore structures may pose a governing element to their design and drive the operational conditions. As offshore structures, such as oil rigs and wind turbines, are exposed to the harsh environment at sea, they are prone to fatigue damage, which limits their operational lifetime. Predicting the wave loading is subject to much uncertainty as it depends on the site-specific metocean conditions and surface properties of the structure. These conditions may change during the lifetime of the installations. It is thus of great interest to monitor the wave loading occurring at actual conditions to ensure that the reliability is maintained.

This thesis features methods of indirect measurements of wave loading. Since it is unfeasible to measure the loading directly, operators need to rely on indirect methods instead. This is done by utilizing the information embedded within the vibrations of the structure. By means of output-only system identification techniques, it is possible to decipher these vibrations to obtain an estimate of the loads. The thesis addresses the current state-of-the-art techniques for system identification and, successively, load identification algorithms. Solutions are evaluated in both the frequency domain as well in the time domain. The performance of load identification is demonstrated through multiple experimental campaigns in both dry and wet conditions. It is sought to determine the limitations of the methods under different loading conditions.

Attached to this thesis are eight papers which combined span the extent of this study. Chapter 6 shows the papers arranged by the suggested reading order.

Resumé

Bølgebelastning på offshore konstruktioner kan være et afgørende element for designet og diktere eventuelle operationelle begrænsninger. Idet offshore konstruktioner, som eksempelvis olierigge eller vindmøller, er eksponeret for det barske miljø på havet, vil de være tilbøjelig til at få fatigue skader, hvilket vil begrænse levetiden. At forudsige størrelsen af bølgebelastningen vil være underlagt en stor usikkerhed, idet den afhænger af lokale metocean forhold samt overfladeegenskaberne af konstruktionen. Disse er elementer, som ændrer sig igennem levetiden af installationerne. Det er derfor af stor interesse at ovevåge bølgebelastningen under de aktuelle forhold, for at sikre at reliabiliteten er overholdt.

Denne afhandling berører metoder for indirekte målinger af bølgebelastning. Siden det sjældent er muligt at måle belastningerne direkte, må man i stedet støtte sig til indirekte metoder. Dette kan gøres ved at udnytte den information, der ligger gemt i konstruktionens vibrationer. Ved hjælp af output-only system identifikationsteknikker er det muligt at afkode disse vibrationer og herved opnå et estimat på belastningen. Denne afhandling kommer omkring nogle af de aktuelle state-of-the-art system identifikationsteknikker og efterfølgende lastidentifikationsalgoritmer. Løsninger er evalueret i både frekvensdomænet samt i tidsdomænet. Metodernes performance testes igennem en serie af eksperimentelle forsøg under både tørre og våde forhold. Det søges at afdække metodernes begrænsninger igennem forskellige belastningsscenarier. Vedhæftet denne afhandling findes otte artikler, som tilsammen udspænder omfanget af dette studie. Kapitel 6 viser artiklerne arrangeret iht. anbefalet læserækkefølge.

Contents

Nomenclature

This list contains the most common nomenclatures used in the thesis. In the appended papers, however, please be aware the the symbols may deviate from the list below.

Latin symbols

c_r	Modal damping
C_d	Drag coefficient
C_m	Mass coefficient
$\underline{\underline{C}}$	Damping matrix
dt	Time increment
D	Pile diameter
$\underline{f}$ / $\underline{F}$	Load
f_n	Natural frequency
F_w	Total wave load
g	Load scaling function
h	Still water depth
$\underline{\underline{H}}$	Frequency response function or state to measurement matrix
j	Imaginary unit, $j^2 = -1$
k_r	Modal stiffness
$\underline{\underline{K}}$	Stiffness matrix or Kalman gain matrix
m_r	Modal mass
$\underline{\underline{M}}$	Mass matrix

$\underline{q}$	Modal coordinates
$\underline{\underline{Q}}$	Process error covariance matrix
Q_r	Mode shape scaling function
$\underline{\underline{R}}$	Measurement error covariance matrix
$\underline{\underline{S}}$	Load error covariance matrix
$\underline{\underline{S_a}}$	Sensor selection matrix, acceleration
$\underline{\underline{S_v}}$	Sensor selection matrix, velocity
$\underline{\underline{S_d}}$	Sensor selection matrix, displacement
s	Laplace operator
$\underline{\underline{S_p}}$	Spatial distribution matrix
t	Time
u	Water particle velocity
$\dot{u}$	Water particle acceleration
$\underline{v}$	Measurement noise (Gaussian function)
$\underline{w}$	Process noise (Gaussian function)
$\underline{x}$	State vector
$\underline{y}$ / $\underline{Y}$	Structural displacement
$\underline{\dot{y}}$ / $\underline{\dot{Y}}$	Structural velocity
$\underline{\ddot{y}}$ / $\underline{\ddot{Y}}$	Structural acceleration
$\underline{z}$	General measurements vector
$\underline{\underline{Z}}$	Impedance matrix

Greek symbols

ζ_r	Damping ratio
η	Surface elevation / Load noise (Gaussian function)
λ_r	Pole
$\underline{\underline{\Lambda}}$	Pole matrix
ρ	Fluid density
$\underline{\phi_r}$	Mode shape
$\underline{\underline{\Phi}}$	Mode shape matrix
ω	Angular frequency
ω_r	Natural angular frequency ($2\pi f_n$)
ω_{dr}	Natural (damped) angular frequency

Superscript

$\dot{x}$	Derivative with respect to time
$\dagger$	Pseudo inverse
^{H}	Hermitian transpose
^{T}	Transpose
*	Complex conjugate
^{a}	Augmented state

Subscript

Throughout this thesis (papers included), vectors will be denoted by a single underline and matrices by a double. Hence, X should be interpreted as a scalar, $\underline{X}$ as a vector and $\underline{\underline{X}}$ as a matrix.

Abbreviations

API	American Petroleum Institute
AU	Aarhus University
CFD	Computational Fluid Dynamics
COSL	China Oilfield Services Limited
DHRTC	Danish Hydrocarbon Research and Technology Centre
DNV	Det Norske Veritas
DOF	Degree Of Freedom
DTU	Technical University of Denmark
DUC	Danish Underground Consortium
EMA	Experimental Modal Analysis
ERA	Eigensystem Realization Algorithm
FDD	Frequency Domain Decomposition
FE	Finite Element
FRF	Frequency Response Function
GPS	Global Positioning System
GSST	Graduate School of Science and Technology, Aarhus University
IMAC	International Modal Analysis Conference
iomac	International Operational Modal Analysis Conference
ISOPE	The International Society of Offshore and Polar Engineers
JONSWAP	Joint North Sea Wave Project
LC	Local Correspondence
LASIF	Large Air-Sea Interaction Facility
MAC	Modal Assurance Criterion
MDOF	Multi Degree Of Freedom
MWL	Mean Water Level
NAM	Nederlandse Aardolie Maatschappij (Dutch Petroleum Company)
OMA	Operational Modal Analysis
PSD	Power Spectral Density
RMS	Root Mean Square
SD	Spectral Density
SDU	University of Southern Denmark
SEREP	System Equivalent Reduction-Expansion Process
SHM	Structural Health Monitoring
SVD	Singular Value Decomposition
UBC	University of British Columbia
UK	United Kingdom
US	United States (of America)

Chapter 1

Introduction

Since 1972 and until today, oil and natural gas have been extracted from the Danish part of the North Sea. The production of oil and gas is administrated by the Danish Underground Consortium (DUC) which consists of the major shareholders: Shell, Mærsk (now Total), Nordsøfonden and Chevron. DUC manages the concession, given to Mærsk in 1962, for the exploration and production of oil and natural gas in the Danish shelf. In 1991, the oil production exceeded the consumption and thus made Denmark self-sufficient. However,

Figure 1.1: Location of some of the oldest/largest production sites in the Danish part of the North Sea.

in 2013, this was again turned to a net consumption and this situation has remained since.

Although a transition towards renewable energy has taken much of the focus in the last decade, the billions of kroner in annual state revenue still makes oil and gas production a necessary part of the Danish economy. In 2015, more than 55 platforms were in operation in Danish waters located at roughly 200 km off the West Coast of Denmark. These are distributed among 19 fields. Figure 1.1 shows a few selected oil fields which are some of the oldest/largest in our continental shelf. Most of the remaining structures are located within 100 km of those shown in the figure.

Figure 1.2: Target structure type. Photo shows the Valdemar BA 2006 well-head platform in the North Sea. Photo courtesy of Mærsk Oil.

These assets at sea are facing challenges ahead as many of them are nearing the end of their design lifetime. This calls for decisions as to whether the structures should be decommissioned or lifetime extensions should be pursued. Lifetime extension can be granted given the operators prove that structures are still fit for operation. This can be done through inspections and repairs. The subsea inspections are challenged by the nature of the environment, where marine growth, waves, and currents complicate the operation. Another great challenge is subsidence, which means that the airgap is diminished, thus leaving the topside more exposed to the harsh environment at sea.

Many different types of structures are to be found in the North Sea, so to limit this study we will select one target structure type. This will be the tripod structure shown in Figure 1.2. Valdemar BA is a monopile structure supported by a tripod foundation. It is located at a water depth of approximately 42 m. DUC currently has 15 similar tripod supported monotowers in the North Sea.

Typical wind and wave spectra are shown in Figure 1.3 along with the first two bending modes of the Valdemar platform. Please note that the spectra are normalized and shown on a normal y axis. From the figure we can note that the main frequency content of the wave spectrum is well below the natural frequency of the platform. Hence, the expected response should be dominated by quasi-static behavior. We will however not restrict the study to this frequency regime, but rather undertake a general approach.

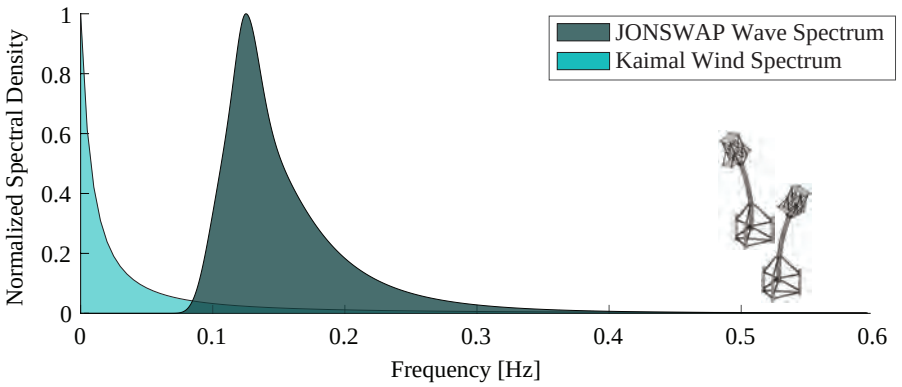

Figure 1.3: Typical wind and wave spectra from the North Sea.[14, 16] The first two bending modes of the Valdemar BA platform are pinned for reference.

Chapter 2

Motivation

The motivation for this study is based on the concerning events recently recorded in the North Sea, where unexpected large waves (rogue waves) were reported near offshore structures. In 2015, the COSL Innovator drilling rig was hit by an enormous wave which resulted in severe damage and one casualty at the Troll oilfield in Norway [30]. During a December storm with an approximately 10 m significant wave height, a rogue wave hit the platform with extensive damage to the living quarters (lower deck). The incident report states that the COSL Innovator suffered damage all the way to the main deck, which in survival mode should have a still water airgap of 24 m [49]. The windows, which were smashed, were estimated to have a breaking strength of 180 kPa. The incident raised questions as to whether the design basis for offshore structures is sufficient in these extreme events.

Extreme wave incidents, including breaking waves, have also been documented in the Danish part of the North Sea. In November 2017 at the Tyra field, a plunging breaking wave was seen. The wave event was even photographed by one of the employees. The photo is given in Figure 2.1. During the same storm, another extreme wave was reported for the area with a crest height of 17 m. From wave statistics for the area, this wave was assessed to exceed the 10 000-year return period. Breaking waves of this type were not expected to occur in these waters, and the structures were not designed against the extensive loads which plunging breaking waves induce. Luckily, no damage was caused by this storm, but these concerning events were the starting point for an intensive study on the reliability of Mærsk's offshore structures [60, 61].

The complexity of abnormal and potentially breaking waves yields uncer-

Figure 2.1: Plunging breaking wave at Tyra West, November 2017. Photo courtesy of Mærsk Oil.

tainty regarding the loading effects, and these may have severe consequences for the integrity of the structures at sea. In general, considerable uncertainty persists in the field of wave loading of offshore structures as the load models are based on scaled laboratory experiments. When the structures are in operation for decades, the conditions under which they operate are constantly changing. These changes may be in terms of operational purposes (connecting bridges, structural modifications, mass loading), or changes to the kinematics, (marine growth, seabed scour, seabed subsidence), or general structural degradation (corrosion, fatigue, ageing). Since the wave loading couples to the structure through geometry, surface roughness, and dynamics, all of these factors give rise to doubt about the basis for the design. It is therefore of great interest to monitor the loading to ensure that reliability is maintained throughout the life span.

2.1 Traditional ways of calculating wave forces

The design of offshore structures is traditionally done in accordance with the recommended practice of Det Norske Veritas (DNV) [15] or relevant standards

by the American Petroleum Institute (API). If a dynamic response is deemed likely, then a dynamic analysis shall be conducted in the time domain using stochastic modelling of the sea state, including directional spreading. If the response is dominated by quasi-static behavior, then the design is based on a deterministic approach using regular waves. The procedure for determining the wave loads on a fixed structure is hence based on a given return period. Metocean data provide a probabilistic basis for establishing a design wave height and corresponding period. The fluid acceleration and velocity are calculated using a suitable wave theory, such as the Stokes or Stream theory. For deep water design, the Airy (linear wave theory) is used.

The linear and Stoke wave theory provide wave kinematics below the mean water level (MWL). Here, stretching or extrapolation methods can estimate kinematics above the MWL [72]. The loads are consequently derived from the fluid motion using the Morison equation [43]. The Morison equation is based on empirically determined coefficients for the added mass and drag, C_m and C_d, which describe the load proportionality to fluid acceleration and squared velocity. They are dependent on the member shape and levels of surface roughness, i.e. the Reynolds number and the Keulegan Carpenter number. The resulting wave loads can hence be obtained as:

$$F_w(t) = \underbrace{\int_{-h}^{\eta(t)} \frac{\pi}{4} D^2 \rho C_m \dot{u}(z,t) \, \mathrm{d}z}_{\text{Inertia}} + \underbrace{\int_{-h}^{\eta(t)} \frac{1}{2} D \rho C_d u(z,t) |u(z,t)| \, \mathrm{d}z}_{\text{Drag}} \quad (2.1)$$

here, h is the still water level, η is the surface elevation, D is the structure diameter, ρ is the fluid density, C_m and C_d are the empirically determined mass and drag coefficients to account for different shapes and surface roughness. Finally, $\dot{u}$ and u are the fluid particle acceleration and velocity in the cross member direction.

The equation is valid for rigid slender structures in undisturbed waves. This means it does not account for coupling effects between the structure and fluid. For a floating or flexible structure, the Morison equation can be expanded by a weak coupling to account for the relative movements between the fluid and the structure. It is a weak coupling as it still assumes an independent flow field.

When waves grow sufficiently steep, they will become unstable and possibly break and/or induce slamming loads to the structure. The loads are very dependent on the type of wave breaking. A huge effort has been made in deriving methods to describe the wave kinematics and loads of breaking waves, either through adding another term to the Morison equation (slamming) or by

a numerical/CFD approach. However, the methods are most often verified by scaled laboratory experiments and scaling effects of unknown magnitude may be present when a full-scale breaking wave is impacting on a structure [13, 56]. Air entrapment, for instance, is not easily scalable.

The low order wave theory combined with the Morison equation is still widely used in the industry. This is probably due to its computational efficiency. The linear wave theory, however, is based on a linearisation of the boundary condition which does not accurately describe the kinematics in the splash zone and subsequently misjudges the loads in this region. Besides the modelling uncertainty, the load model is based on assumptions on the seabed, structural dynamics, and surface properties. These are factors that may change during the lifetime, for instance due to scour, marine growth or operational conditions.

2.2 Original contributions

A new approach, not subjected to scaling limitations for wave load quantification, is presented in this Ph.D. thesis. By monitoring the vibration response of an offshore structure, the structure itself can be used as a live, full-scale load cell. It will thus be possible to monitor the loads occurring in real conditions, with the actual level of marine growth, scour, and all structural boundary conditions, etc. This will then be a valuable input to the SHM and serve the design basis for future platforms.

At the time of initiation of this Ph.D. thesis, only limited research has been performed specifically to this application [26, 52]. Until now, more focus has been placed on indirect methods of, for example, fatigue assessment and damage detection of offshore structures [39, 47]. The load identification from the wave action is a challenging discipline to verify, and even more difficult if a dynamic response is present. This may be the reason why little work has been done in the past. This study focuses on the state-of-the-art load identification methods in structural dynamics and assesses whether these are applicable in the context of wave loading on offshore structures. It has been an essential task to modify the available methods such that they accommodate the challenges inherent in the marine environment.

The load identification procedure requires a long list of subroutines needed for a successful estimate. We will rely on the output only analysis - which does not interfere with the production. Load identification from an output only analysis is considerably more difficult compared to calibrating a model

to a known input as there are only limited means for verifying the estimates. Laboratory experiments hence form the majority of this study, which, to some extent, allows for verifying the estimated input.

Current methods are highly reliant on the model accuracy and assumptions on the location of the input. It has thus been a focus to assess the sensitivity given different assumptions. It was found that, in general, the structural accelerations are insufficient to determine the loads accurately if no additional information is available. It is thus evaluated how the algorithm stabilizes by merging it with different load models or scenarios. The study is, in general, restricted to linear models.

Chapter 3

State of the art

Since the introduction of modal analysis, identifying the input forces using the system response has been an intriguing task in structural dynamics. In continuation of modal analysis and system identification, many attempts have been made to derive methods to determine the loads in a dynamic system. As for modal analysis; load identification originates from the automotive and aircraft industries. Many researchers have explored the principles of load identification and the potential pitfalls it entails [17, 38, 58]. The first published research in this area can be traced back to the mid-70s where Flannelly et al. [6, 21, 23] performed modal testing on helicopters on behalf of the US air force. They deployed classical experimental modal analysis and made the identification by using the pseudo inverse method as described in Section 4.4. They examined the consequences of model errors by introducing mass changes into the system simulating fuel consumption. They found that when analyzed with care, the load could be identified within 20% accuracy; however, the object was a steel helicopter chassis with suspended boundary conditions.

Later, Brenda Hillary followed, with her Ph.D. thesis on indirect measurements of vibration excitation forces [24]. She studied several aspects of load identification. Also she used the pseudo inverse approach while conducting both numerical and experimental works while targeting the unsteady aerodynamic forces on a turbo blade. Although most of her work was limited to cantilever beams, she also studied how the residuals from omitted modes could affect the result.

In 1986, James Fabunmi [18] followed the studies by examining some of the challenges to the pseudo inverse method. While his focus was constrained to the

frequency domain, he introduced random errors into the mobility matrix (also known as frequency response function) and discovered that small perturbations could cause large variations in the identified load. He also studied how the method could be used to identify multiple loads, although with limited success.

In 1987, Karl Stevens [58] wrote his overview on the topic. Despite the fact that his work included neither experimental nor simulated cases, his paper is often referred to as one of the cornerstones in the history of load identification methods. He suggests that to overcome the sensitivity issues, it is necessary to aid the inverse calculations by knowledge about the nature of the load. This may involve the frequency content or spatial distribution.

After the millennium, Ma et al. made some of the first attempts in formulating a recursive model for a multi-degree-of-freedom system. They made the state-space formulation of the structural system and by using a Kalman filter [27] they obtained an estimate of the system state along with the load. The theory, which they adopted from heat transfer analysis, allows for real-time estimates of the load. Since then, many different modifications to the technique have been made. These, for instance, include merging of different sensor types, different ways of expanding the state vector, or different system models or different interstep assumptions, etc. [22, 25, 32, 37, 44].

From 2012 and onwards, Maes and Lourens devoted their studies to improving the Kalman filter-based method. They formulated the state space equations from modal parameters. This, in particular, is convenient if the system identification is based on operational modal analysis [12]. They showed various cases of application of the theory, including, for instance on footbridges [41] and monopiles [39, 42].

In Figure 3.1 some of the pioneering works on load identification are shown. Between 2012 and 2019, an exponential growth in papers per year is seen. Note that Figure 3.1 shows only a selection in these papers. Methods using artificial intelligence such as neural networks have not been in focus and are hence omitted from the literature review.

3.1 Offshore industry practice

Loland, Dodds, and Begg conducted extensive studies on vibration-based monitoring of offshore structures in the mid-70s. They examined whether damage could be detected by monitoring the changes in natural frequencies. They did both laboratory work and full-scale tests on several platforms in the North Sea [7, 34, 45]. Their motivation was to remove the continuous diver-driven inspec-

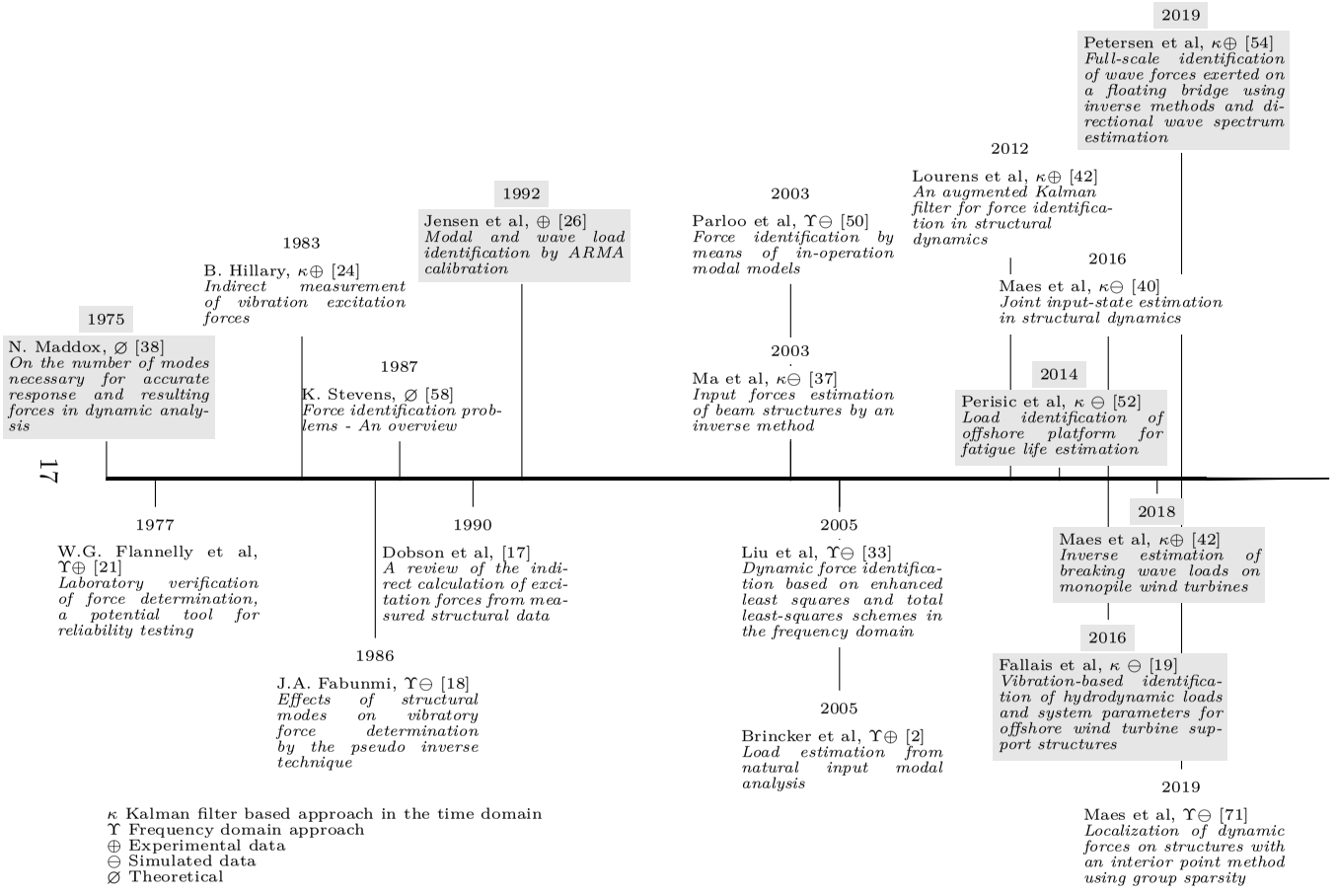

Figure 3.1: Indirect methods for load identification timeline. Grey are research related to offshore structures.

tions by introducing vibration-based structural health monitoring instead. If SHM could supersede the traditional inspection scheme, it would also become weather and sea state independent. After a considerable number of studies, they realized that there is a strong limitation to the accuracy of damage detection - especially if the location of the sensors are constrained to the topside [20].

In the early 90s, an extensive monitoring campaign was conducted by an association of major oil companies (Shell, British Petrolium, Conoco, Cheveron etc.) [4]. The study was based on the steel jacket platform, Tern, in the North Sea. Over a period of two years, they monitored the loading on the platform in order to assess current design models and statistics. The platform was equipped with strain gauges distributed to the subsea structure. These, together with an FE model, were used for determining the global loads. Wave gauges and particle velocity meters were used to assess the wave conditions. They found that, in general, the Morison equation was a good load model with little conservatism to the actual conditions. Extreme wave events were reported during the monitoring period, yet the report states nothing about the occurrence of breaking waves. The current design basis benefits from the experience gathered from this study.

With the digitalization of data acquisition, monitoring became easier and was thus reintroduced as a natural element in the offshore industry. More sophisticated and accurate data post-processing and structural modelling gave new life to structural health monitoring. The SHM is consequently introduced to both offshore wind turbines and production platforms. The monitoring process may in general cover many different aspects. Load monitoring and adaption is a natural element in the operation of wind turbines. The dynamic complexity of turbines is substantially different due to the adaptation for optimized power production and reduced loads [3, 47]. Consequently, the offshore wind industry is hence pushing the development in structural monitoring techniques. Regarding production platforms, Rambøll has put extensive effort into developing their own structural monitoring program. This program includes health monitoring and fatigue assessment and also load monitoring from indirect methods. The monitoring is based on automated OMA and FE-updating. They name the concept "digital twin". The process is based on cloud computing allowing for remote monitoring [5, 52, 53, 62, 63].

Chapter 4

Theory

Let us open this section by describing what load identification is and which challenges persist within this field of study. If we consider the general forward flow of a dynamic system, we may describe the process as schematically shown in Figure 4.1. Here, we imagine that an arbitrary input feeds the system. This input can be a single or multiple source. This consequently yields a response (output) of the system. The response depends on the characteristics of both the input and the system (and possibly coupling effects).

In the field of structural dynamics, the input corresponds to loading and the response will thus be the displacements, velocities, and accelerations of the structure. The dynamic properties will drive the behavior of the system. These may be described in terms of natural frequencies, mode shapes, and

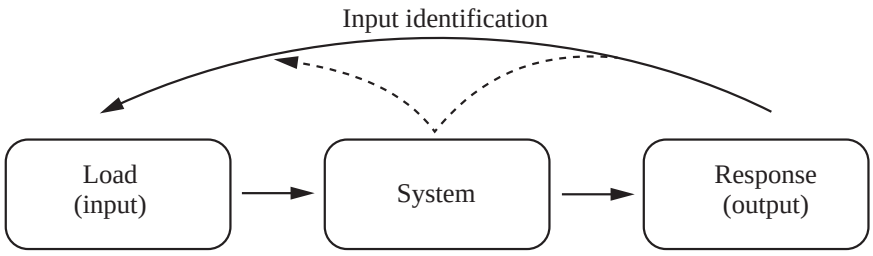

Figure 4.1: General principle of load identification.

damping ratio. These modal parameters relate to the geometry, mass, and stiffness of the structure and are thus independent to the input. (This is only valid for linear systems and in real-life situations this decoupling between the three components may not be as straightforward.) Naturally, the system may be linear or nonlinear, but we shall confine our discussion to the linear systems and assume time-invariant behavior.

The art of input identification will now be the reverse order of this flow. This implies that the response of the structure is measured, and we aim to decipher these measurements in order to identify the load which caused this response. This is why input identification may also be referred to as indirect load measurements. Generally, it is impossible to relate the response directly to the input without knowledge of the system.[1] We thus need to use system identification as a stepping stone in order to achieve what we desire - the load.

4.1 System identification

Modal analysis is a very commonly used approach in extracting the system properties in an experimental framework. Traditional Experimental Modal Analysis (EMA), also known as input-output identification, has proven successful in the field of automotive and aviator industries for decades. Yet, when it comes to application in large civil engineering structures, EMA has some limitations. EMA relies on a known input, either force or forced vibration. Artificial excitation of large structures is very difficult if not impossible and requires a large experimental setup. This may interfere with daily operations, which cannot be allowed in the context of offshore structures where access time may be restricted and where operational downtime is unacceptable. Another approach in modal testing saw the light no more than a few decades ago. This technique is based on an output-only approach. It is called Operational Modal Analysis (OMA) and has become well established for testing of civil engineering structures [11, 55]. As the name indicates, the method relies on operational loading, i.e. ambient excitation. If it can be assumed that the loading is close to Gaussian white noise, i.e. excitation at all frequencies and all locations of the structure, the response from this random excitation can be used to identify the modal parameters. We thus assume that the physical properties are independent of the loading and that the correlation time of the load is limited.

[1] Some methods, which use neural networks, actually aim to make the identification without the need for the system description. These methods rely on training data instead. We will, however, not pursue this approach further.

The convenience of output-only analysis is a double-edged sword, meaning it is quick and reliable, but is misses the information on the scaling of the mode shapes as the input is unknown. The scaling of the mode shapes or rather the modal mass is an essential ingredient in load identification. Despite this flaw to the method, OMA has been the key approach in this thesis. The scaling issue can be mitigated by different approaches. For instance, the mass change method can be applied [10, 28], or introducing a harmonic vibration force [9] or, finally, from an FE model [1]. The latter is used as it does not interfere with operations.

4.2 Response measurement

The response of the structure may be measured by accelerometers. These are the most common instrumentation used offshore. The measurements may be supported by GPS measurements to compensate for the static/quasi-static displacements. The sensor installation for offshore structures is often restricted to the topside, which puts the subsea structure out of reach. This is obvious due to the harsh environment which surrounds the offshore structures. Subsea monitoring is both a great challenge for the sensor installation and the lifetime of the sensors is greatly reduced. However, it is possible to indirectly estimate the response at remote locations.

Several different methods for estimating the response at unmeasured locations (Virtual sensing) exist. For the sake of this study, the modal expansion technique is used. The general principle is that the response is transformed into modal domain by the experimentally obtained mode shapes $\underline{\underline{\Phi_A}}$ as:

$$\underline{\hat{q}}(t) = \underline{\underline{\Phi_A}}^{\dagger} \underline{y_A}(t) \tag{4.1}$$

here, $\underline{y_A}(t)$ is the measured response and $\underline{\hat{q}}(t)$ is the estimated modal coordinates. The response is transformed back to the physical domain using a set of expanded mode shapes $\underline{\underline{\Phi_B}}$. This consequently provides interpolated/extrapolated values of the response.

$$\underline{y_B}(t) = \underline{\underline{\Phi_B}}\, \underline{\hat{q}}(t) \tag{4.2}$$

The number of modes (i.e. columns) in $\underline{\underline{\Phi_A}}$ and $\underline{\underline{\Phi_B}}$ must be the same, while the increase in mode shape resolution will drive the expansion. The mode shapes in $\underline{\underline{\Phi_B}}$ may be obtained from a finite element model. The mode

shapes can either be linear combinations for a best fit [48, 57] or they can be directly taken from the FE model. In order to obtain a meaningful expansion (and thus avoiding over-fitting) the best result is achieved if the FE model is updated such that experimental mode shapes and the finite element mode shapes are well correlated. The virtual sensing is in practice limited to the global behavior of the structure, especially if sensors are located far away from the points of interest.

Once the response is estimated at all positions in the structure, it allows for load identification at these locations. The need for transfer functions between a measurement point and a load source is hence eliminated.

4.3 Input identification

This section will describe the load identification process. In this thesis, mainly two approaches are evaluated in this regard. Sections 4.4 and 4.5 outline the principles of identification in the frequency domain and Section 4.6 outlines the principles of identification in the time domain. It will be shown how the formulae in both cases descend from Newton's equation, which for a multiple degree of freedom (MDOF) system is commonly written as:

$$\underline{\underline{M}}\,\underline{\ddot{y}}(t) + \underline{\underline{C}}\,\underline{\dot{y}}(t) + \underline{\underline{K}}\,\underline{y}(t) = \underline{f}(t) \tag{4.3}$$

here, $\underline{\underline{M}}$, $\underline{\underline{C}}$, and $\underline{\underline{K}}$ are the system mass-, damping-, and stiffness matrices respectively. The system response is described by the three vectors $\underline{\ddot{y}}(t)$, $\underline{\dot{y}}(t)$, and $\underline{y}(t)$, which correspond the system acceleration, velocity, and displacement. Finally, $\underline{f}(t)$ is the load. Here, we assume that the system matrices remain linear, symmetric, and constant in time.

Now, the response from a dynamic system can be evaluated as the convolution between the impulse response function and the load.

$$\underline{y}(t) = \underline{\underline{h}}(t) \circledast \underline{f}(t) \tag{4.4}$$

$$\triangleq \int_{-\infty}^{\infty} \underline{\underline{h}}(t-\tau)\underline{f}(t)\mathrm{d}\tau \tag{4.5}$$

here, $\underline{\underline{h}}(t)$ is the impulse response function and τ is the time lag between the response function and the load. Assuming that the MDOF equation of motion shown in Eq. (4.3) can be decoupled into a series of N uncoupled equations by using modal decomposition, the time domain response is then obtained from the Duhamel integral, which in the modal coordinates reads:

$$q_r(t) = \frac{1}{m_r \omega_{d,r}} \int_{-\infty}^{\infty} p_r(\tau) e^{-\zeta_r \omega_r (t-\tau)} \sin\left(\omega_{d,r}(t-\tau)\right) \mathrm{d}\tau \tag{4.6}$$

where m_r is the modal mass, $\omega_{d,r}$ is the damped natural frequency, p_r is the modal load, ω_r is the undamped natural frequency, ζ_r is the damping ratio, all for mode r. In practice the integral is truncated to $[0; t]$.

To obtain an estimate on the modal load, it requires a deconvolution between the response function and the response measurements. A deconvolution is an aggravating task to handle for most applications, but as a convolution between two functions in the time domain corresponds to a point-wise multiplication in the frequency domain, the problem is conveniently analyzed in here. Likewise we note that the impulse response function and the frequency response function are mutual Fourier transforms.

4.4 Identification in the frequency domain

To derive the frequency response function for an MDOF system, it is common to start out in the Laplace domain where Eq. (4.3) transforms into[2]:

$$\left[s^2 \underline{\underline{M}} + s \underline{\underline{C}} + \underline{\underline{K}}\right] \underline{Y}(s) = \underline{F}(s) \tag{4.7}$$

From here, we can define $\underline{\underline{Z}}(s)$ as the system impedance matrix, which is:

$$\underline{\underline{Z}}(s) = \left[s^2 \underline{\underline{M}} + s \underline{\underline{C}} + \underline{\underline{K}}\right] \tag{4.8}$$

We wish to obtain a relation between the input and the output. So inserting the definition of impedance and rewriting, Eq. (4.3) becomes:

$$\underline{\underline{H}}(s)\, \underline{F}(s) = \underline{Y}(s) \tag{4.9}$$

where

$$\underline{\underline{H}}(s) = \underline{\underline{Z}}(s)^{-1} \tag{4.10}$$

Finally, to obtain the frequency response function, we adhere to the imaginary axis in the s-plane by putting $s = j\omega$, which yields:

$$\underline{\underline{H}}(j\omega)\, \underline{F}(j\omega) = \underline{Y}(j\omega) \tag{4.11}$$

[2]The derivation shown in this section can be found in most dynamic textbooks e.g. [8] or [11].

where $\underline{\underline{H}}(j\omega)$ is the frequency response function, often written as $\underline{\underline{H}}(\omega)$. The frequency response function (FRF) can be written in terms of displacements, velocities or accelerations. It may consequently be referred to as dynamic flexibility, mobility, or accelerance. A transformation from one type to another merely requires a multiplication of $j\omega$.

Frequency response function from OMA

The system identification - OMA - yields modal parameters rather than complete system matrices, so it is convenient to derive an expression for the frequency response function based on the output from the modal analysis. Starting from Eq. (4.8) and Eq. (4.10):

$$\left[s^2\underline{\underline{M}} + s\underline{\underline{C}} + \underline{\underline{K}}\right] = \underline{\underline{H}}(s)^{-1} \tag{4.12}$$

Pre- and post multiplying by the mode shape matrix $\underline{\underline{\Phi}}^T$ and $\underline{\underline{\Phi}}$ respectively gives:

$$\underline{\underline{\Phi}}^T \left[s^2\underline{\underline{M}} + s\underline{\underline{C}} + \underline{\underline{K}}\right] \underline{\underline{\Phi}} = \underline{\underline{\Phi}}^T \underline{\underline{H}}(s)^{-1} \underline{\underline{\Phi}} \tag{4.13}$$

This operation diagonalizes the system matrices given that the system is proportionally damped and the mode shapes are orthogonal. We consequently define $\underline{\underline{\Lambda}}(s)$ as the pole matrix.

$$\underline{\underline{\Lambda}}(s) = \begin{bmatrix} s^2m_1 + sc_1 + k_1 & \dots & 0 \\ \vdots & \ddots & \vdots \\ 0 & \dots & s^2m_n + sc_n + k_n \end{bmatrix} \tag{4.14}$$

where, m_r, c_r and k_r are the modal- mass, damping, and stiffness. n is the number of modes in the system. The polynomials can be factored into a function of their roots, which come in pairs of complex conjugates:

$$\Lambda_{rr} = s^2m_r + sc_r + k_r \tag{4.15}$$

$$= m_r\left(s - \lambda_r\right)\left(s - \lambda_r^*\right) \tag{4.16}$$

where

$$\lambda_r = -\zeta_r\,\omega_r \pm j\omega_r\sqrt{1 - \zeta_r{}^2} \tag{4.17}$$

here, ζ_r is the damping ratio for mode r and ω_r is natural angular frequency for mode r:

$$\omega_r^2 = \frac{k_r}{m_r} \quad \text{and} \quad \zeta_r = \frac{c_r}{2\sqrt{m_r k_r}} \tag{4.18}$$

With the introduction of the pole matrix $\underline{\underline{\Lambda}}(s)$, Eq. (4.13) becomes:

$$\underline{\underline{\Lambda}}(s) = \underline{\underline{\Phi}}^T \underline{\underline{H}}(s)^{-1} \underline{\underline{\Phi}} \tag{4.19}$$

Next, we can take the inverse of both sides, which yields:

$$\hat{\underline{\underline{\Lambda}}}(s) = \underline{\underline{\Phi}}^{-1} \underline{\underline{H}}(s) \left(\underline{\underline{\Phi}}^T \right)^{-1} \tag{4.20}$$

Here, $\hat{\underline{\underline{\Lambda}}}(s)$ is the inverse pole matrix. Since the pole matrix is diagonal, the inverse corresponds to the reciprocal value of each element along the diagonal. Again premultiplying by the mode shape matrix and postmultiplying by the transposed mode shape matrix we obtain:

$$\underline{\underline{H}}(s) = \underline{\underline{\Phi}} \hat{\underline{\underline{\Lambda}}}(s) \underline{\underline{\Phi}}^T \tag{4.21}$$

We note that this corresponds to a sum of N modal contributions, which we can be split by partial fraction expansion. Meanwhile we again adhere to the frequency domain by letting $s = j\omega$ and hence obtain a very useful expression for the frequency response function:

$$\underline{\underline{H}}(\omega) = \sum_{r=1}^{N} \frac{Q_r \, \underline{\phi_r} \, \underline{\phi_r}^T}{j\omega - \lambda_r} + \frac{Q_r^* \, \underline{\phi_r}^* \, \underline{\phi_r}^H}{j\omega - \lambda_r^*} \tag{4.22}$$

Here, $\underline{\phi_r}$ is the mode shape vector and Q_r is a scaling constant, both for mode r. Superscript * and ^{H} means the complex conjugate and Hermitian transpose respectively. The nominator in the equation, i.e., the outer vector product between a set of scaled mode shapes is known as the pole residue.

The mode shape scaling constant Q_r is obtained in the following manner:

$$Q_r = \frac{1}{j\, 2 \omega_{dr} \, m_r} \tag{4.23}$$

where, ω_{dr} is the damped natural frequency and m_r is the modal mass, both for mode r. It is common to scale the mode shapes according to the mass of system such that we obtain unity modal mass. The roots to the polynomials in $\underline{\underline{\Lambda}}(s)$, λ_r are also referred to as poles of the system as they correspond to points of resonance.

The expression shown in Eq. (4.22) is based on system displacements, i.e., the receptance or dynamic flexibility. Following Maxwell's reciprocity theorem, the FRF matrix is a symmetric square matrix. Its size depends on the number of degrees of freedom i.e., the length of the mode shape vector. Meanwhile, we note that the rank of the response function will be equal to the number of modes N, given that the mode shapes are orthogonal.

Load identification

If we recall the flow in Figure 4.1 along with Eq. (4.11), the tempting first approach to determining the unknown load is to premultiply by the inverse FRF matrix on both sides such that:

$$\underline{\hat{F}}(\omega) = \underline{\underline{H}}(\omega)^{-1}\,\underline{Y}(\omega) \tag{4.24}$$

However, since the FRF matrix is often ill-conditioned and thus close to singular, the inverse matrix is prone to large numerical errors. The ill-condition may descend from rank deficiency, which occurs if the number of independent modes is less than the length of the mode shape vector. A workaround for this singularity issue can be through the Moore-Penrose pseudo inverse [51] or inverse using the singular value decomposition. The Moore-Penrose inverse of a matrix $\underline{\underline{A}}$ may be obtained as:

$$\underline{\underline{A}}^{\dagger} = \left(\underline{\underline{A}}^{H}\,\underline{\underline{A}}\right)^{-1}\underline{\underline{A}}^{H} \tag{4.25}$$

here, superscript ^{H} is the Hermitian transpose and † is the pseudo inverse. This approximation can be made even though $\underline{\underline{A}}$ is a non-square matrix.

The inverse using the singular value decomposition (SVD) is performed in the following manner: The singular value decomposition of a matrix $\underline{\underline{A}}$ factorizes it such that:

$$\underline{\underline{A}} = \underline{\underline{U}}\,\underline{\underline{\Sigma}}\,\underline{\underline{V}}^{*} \tag{4.26}$$

where $\underline{\underline{U}}$ and $\underline{\underline{V}}$ contain the left and right singular vectors and $\underline{\underline{\Sigma}}$ contains the singular values on the diagonal in descending order. The inverse of $\underline{\underline{A}}$ will hence be:

$$\underline{\underline{A}}^{\dagger} = \underline{\underline{V}}\,\underline{\underline{\Sigma}}^{\dagger}\,\underline{\underline{U}}^{*} \tag{4.27}$$

Since $\underline{\underline{\Sigma}}$ is diagonal, its inverse corresponds to the reciprocal in all non-zero elements. The SVD approach can be used to remove noise by setting a threshold on the singular values. With the introduction of the pseudo inverse, Eq. (4.24) now becomes:

$$\underline{\hat{F}}(\omega) = \underline{\underline{H}}(\omega)^{\dagger}\,\underline{Y}(\omega) \tag{4.28}$$

This evades the singularity issue, but the truncation errors still persist, which can yield large numerical errors. This is shown in paper II.

To ensure a consistent result from this relation, the solution must be constrained. This can be done by defining loading scenarios implemented as a

factorization of the load into m different sources, each with a fixed spatial distribution $\underline{S_p}$ and a corresponding scaling function $g(\omega)$:

$$\underline{\hat{F}}(\omega) = \underline{S_p}^{(1)} g(\omega)^{(1)} + \underline{S_p}^{(2)} g(\omega)^{(2)} \ ... + \underline{S_p}^{(m)} g(\omega)^{(m)} \tag{4.29}$$

$$= \underline{\underline{S_p}}\, \underline{g}(\omega) \tag{4.30}$$

here, $\underline{\underline{S_p}}$ is the spatial distribution matrix, where the columns contain the spatial distribution from each source. $\underline{g}(\omega)$ consequently becomes a vector with the scaling function for each source. If the spatial distribution is known, this definition can be inserted into Eq. (4.11) and the equation can be solved for the scaling functions.

$$\underline{Y}(\omega) = \underline{\underline{H}}(\omega)\, \underline{\underline{S_p}}\, \underline{g}(\omega) \tag{4.31}$$

$$\underline{\hat{g}}(\omega) = \left(\underline{\underline{H}}(\omega)\, \underline{\underline{S_p}} \right)^{\dagger} \underline{Y}(\omega) \tag{4.32}$$

This shows the general approach with several load sources. In practice, this will only work if a single or few sources are present at the same time. If a single load source drives the response, the expression simplifies as $\underline{\hat{g}}(\omega)$ becomes a scalar such that

$$\hat{g}(\omega) = \left(\underline{\underline{H}}(\omega)\, \underline{\underline{S_p}} \right)^{\dagger} \underline{Y}(\omega) \tag{4.33}$$

Example I

Here we will make an example with dual input on a uniform plane cantilever beam. We will consider a six DOF system with a load acting on the middle and top node, i.e., in DOF 3 and 5, see Figure 4.2. The figure shows the input and corresponding response for each node in the cantilever beam model.

The load identification will be based on a truncated FRF matrix including only the first three bending modes ($f_n = 3,\ 19,\ 53\,\text{Hz}$). The FE model provides the modal parameters without any error. The response due to the loading history is simulated using a Newmark solver. Noise is subsequently added to the response and thus considered as the "measured" signal. We will assume that the displacements are measured at all six DOFs.

The load identification will be split in two; one following Eq. (4.28) and one following Eq. (4.32). The estimate from Eq. (4.28) corresponds to an unknown load position while the estimate from Eq. (4.32) corresponds to a known spatial

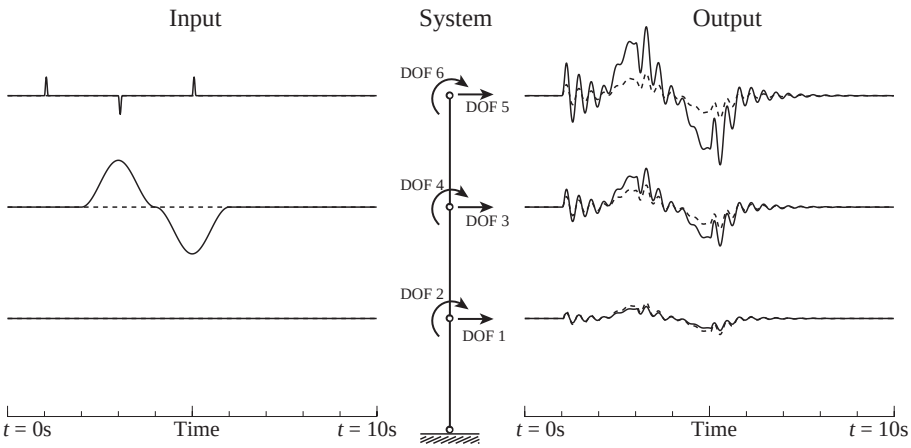

Figure 4.2: Simulated system for example. The dashed lines indicate moment and corresponding rotations while the solid lines indicate the force and corresponding displacements. A flat line corresponds to zero loading and zero response.

distribution. The spatial distribution matrix in the latter case becomes:

$$\underline{\underline{S_p}} = \begin{bmatrix} 0 & 0 \\ 0 & 0 \\ 1 & 0 \\ 0 & 0 \\ 0 & 1 \\ 0 & 0 \end{bmatrix} \tag{4.34}$$

The result is shown in Figure 4.3, where the value from knowing the spatial distribution is evident. NB, an unknown spatial distribution corresponds to having $\underline{\underline{S_p}}$ equal to the identity matrix. A more detailed study of the modal truncation and errors in modal parameters is given in papers II and III.

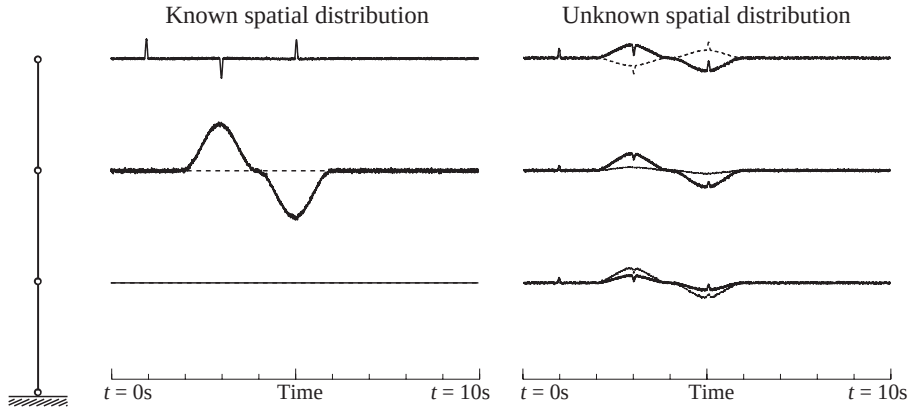

Figure 4.3: Estimated input forces. The dashed lines indicate moment, and the solid lines indicate the force. A flat line corresponds to zero loading. The FRF matrix is in this example truncated to three modes.

4.5 Identification in the modal domain

This section is dedicated to load identification in the cases of random loading. Through having a well-defined system subjected to (perfect) white noise input, it is possible to derive an expression for a load estimate based on the variance of the response. The theoretical response variance of a linear SDOF system subjected to white noise forced excitation is given by the integral of the squared response function and scaled by the load density [46]:

$$\mathrm{E}[y^2(t)] = \int_{-\infty}^{\infty} |H(\omega)|^2 S_0 \, \mathrm{d}\omega = \frac{\pi S_0}{kc} \tag{4.35}$$

where, $\mathrm{E}[y^2(t)]$ is the variance of the zero mean response, S_0 is the constant spectral density of the load ($S_0(\omega) = S_0$), k and c are the stiffness and damping coefficients of the system respectively.

The expression in Eq. (4.35) may be considered as a single mode of resonance in a linear MDOF system. It should thus be possible to estimate the spectral density of the modal load for an MDOF system subjected to random loading. The problem is thus transformed into the modal domain through modal decomposition. First, we have the response in modal coordinates:

$$\underline{q}(t) = \underline{\underline{\Phi}}^{\dagger} \underline{y}(t) \tag{4.36}$$

The response variance in modal coordinates follows mode by mode as $\mathrm{E}[q_r^2(t)]$.

It is now possible to rearrange the expression in Eq. (4.35) to obtain an estimate on the modal load density which for mode r reads:

$$\hat{S}_{0r} = \frac{\mathrm{E}[q_r^2(t)] \; k_r \; c_r}{\pi} = \frac{\mathrm{E}[q_r^2(t)] \; 2 \; \omega_r^3 \; \zeta_r}{\pi} \tag{4.37}$$

Here we assume that the mode shapes in $\underline{\underline{\Phi}}$ are mass-normalized. ω_r is the natural angular frequency and ζ_r is the damping ratio, both for mode r.

The estimates on the constant spectral modal load, $\hat{S}_{0r}$, should be considered as diagonal values in the estimated power spectral density matrix of the modal load:

$$\underline{\underline{\hat{G}_{qx}}}(\omega) = \begin{bmatrix} \hat{S}_{01} & 0 & \dots & 0 \\ 0 & \hat{S}_{02} & \dots & 0 \\ \vdots & \vdots & \ddots & \vdots \\ 0 & 0 & \dots & \hat{S}_{0n} \end{bmatrix} \tag{4.38}$$

Example II

Again, considering a cantilever beam with a total of 6 DOFs as shown in Figure 4.4. (Please be aware that the dynamic properties differ from the model shown in Example I). The beam is subjected to zero-mean uncorrelated random loading at all DOFs and the response is recorded in terms of displacements. The power spectral density of the input load is shown in Figure 4.4. Here we verify that the load is uncorrelated among the different DOFs (yielding a zero cross spectrum). The spectral density matrix of the load $\underline{\underline{G_{xx}}}(\omega)$ (in physical coordinates) is obtained from the magnitude squared of the Fourier transform and normalized with the signal length, thus leaving the auto spectra on the diagonal and the cross spectra on the off diagonals. The spectra shown in Figure 4.4 to 4.6 are all averaged using the principles of Welch segmenting. The indices used on the spectral densities x, y, q indicate input, output and modal transformation respectively.

For the system at hand the size of $\underline{\underline{\Phi}}$ is 6×6. The response is now projected onto these six modes and the power spectral density of the response can be obtained in modal coordinates. The auto spectra are shown in Figure 4.5. We note that for each of the modal lines, the area underneath corresponds to the variance of the response for that mode. Once the modal variance is calculated for all modes, r, an estimate on the spectral density of the modal load is obtained from Eq. (4.37).

The estimates of $\hat{S}_{0r}$ are shown in Figure 4.6 as the solid black lines. The result is plotted at an arbitrary frequency band near the resonance frequency

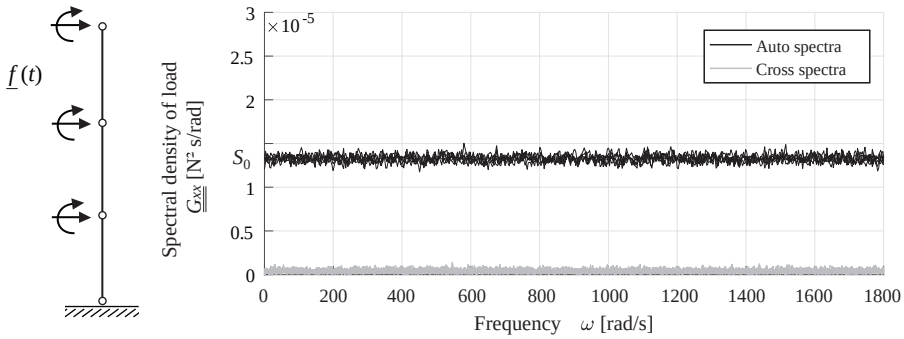

Figure 4.4: Single-sided load power spectral density in physical domain.

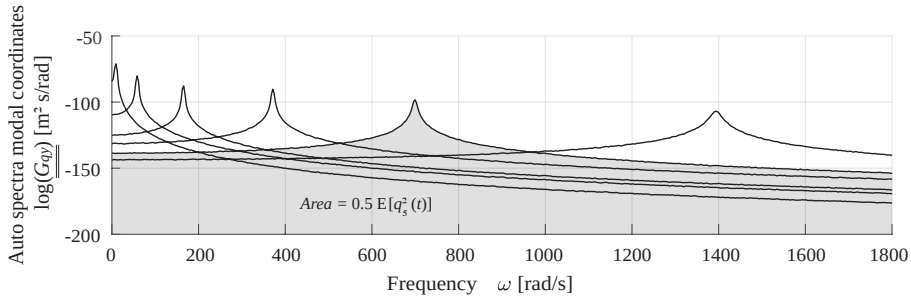

Figure 4.5: Single-sided response autopower spectral density in modal domain.

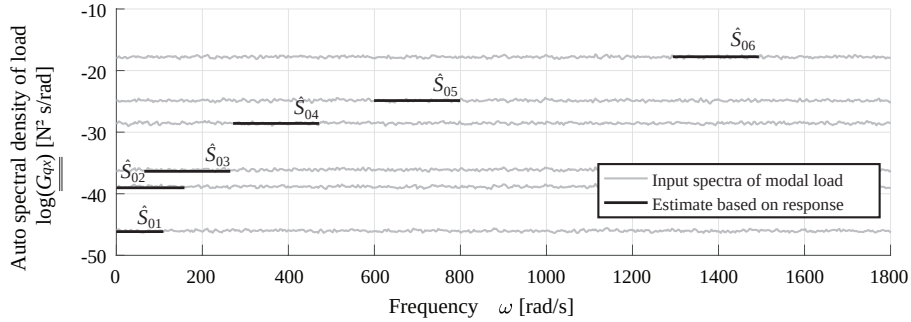

Figure 4.6: Single-sided load autopower spectral density in modal domain.

but should in principle be considered as a constant value for all frequencies $\hat{S}_{0r}(\omega) = \hat{S}_{0r}$. The underlying grey lines in Figure 4.6 are the diagonal values of the true input spectra in modal coordinates composed from any of the following:

$$\underline{\underline{G_{qx}}}(\omega) = \text{PSD}\left(\underline{q_x}(t)\right) = \text{PSD}\left(\underline{\underline{\Phi}}^T \ \underline{f}(t)\right) = \underline{\underline{\Phi}}^T \underline{\underline{G_{xx}}}(\omega) \ \underline{\underline{\Phi}} \tag{4.39}$$

here, $\underline{q_x}(t)$ contains the modal load, $\underline{f}(t)$ is the load vector for the MDOF system in the time domain. The PSD should be considered a transformation into power spectral densities.

By this example, we have shown that it is possible to estimate the constant load spectra in the modal domain for a linear MDOF system. However, challenges remain as a transformation back into the physical domain is deceitful.

Despite the load cross spectra being zero in the physical domain, as was shown in Figure 4.4, and hence reducing the spectral density matrix, $\underline{\underline{G_{xx}}}(\omega)$, to a diagonal matrix, this is not the case in the modal domain as $\underline{\underline{G_{qx}}}(\omega)$ is not diagonal as it was assumed in Eq. (4.38). Therefore a transformation back to the physical domain is not feasible:

$$\underline{\underline{G_{xx}}}(\omega) \neq \left(\underline{\underline{\Phi}}^T\right)^\dagger \underline{\underline{\hat{G}_{qx}}}(\omega)\underline{\underline{\Phi}}^\dagger \tag{4.40}$$

Sadly, it has not been possible to derive an expression for the off-diagonal values in $\underline{\underline{\hat{G}_{qx}}}(\omega)$ which imprisons us in the modal domain. It was thus chosen to conclude this study and not proceed with cases of colored input or truncated response functions.

4.6 Identification in the time domain

In recent decades, much attention has been given to identification in the time domain using a Kalman filter [27] and other adaptive filters. This section will outline some of the basic principles for this technique. The main difference is that the input is derived recursively along with an estimate on the system state.

The formulae can be found in numerous works, but an excellent reference is Lourens et al. [35, 36]. The derivation presented in this section will originate from the system matrices, but can be formulated from modal parameters as is shown in paper VI.

State space formulation

We start out from the equation of motion:

$$\underline{\underline{M}}\,\underline{\ddot{y}}(t) + \underline{\underline{C}}\,\underline{\dot{y}}(t) + \underline{\underline{K}}\,\underline{y}(t) = \underline{f}(t) \tag{4.41}$$

As for the frequency domain approach, the load $\underline{f}(t)$ is separated into a spatial distribution and the scaling as

$$\underline{f}(t) = \underline{\underline{S_p}}\,\underline{g}(t) \tag{4.42}$$

Every column in $\underline{\underline{S_p}}$ is the spatial distribution for the corresponding element in $\underline{g}(t)$. If only a single input is present, $\underline{\underline{S_p}}$ becomes a vector and $\underline{g}(t)$ a scalar. The spatial distribution may vary in time as well although this is omitted from this section. A convenient representation of Eq. (4.41) is also: (which we will return to later on.)

$$\underline{\ddot{y}}(t) = -\underline{\underline{M}}^{-1}\underline{\underline{C}}\,\underline{\dot{y}}(t) - \underline{\underline{M}}^{-1}\underline{\underline{K}}\,\underline{y}(t) + \underline{\underline{M}}^{-1}\underline{\underline{S_p}}\,\underline{g}(t) \tag{4.43}$$

The system response can be written in state space format by defining the state vector:

$$\underline{x}(t) = \begin{bmatrix} \underline{y}(t) \\ \underline{\dot{y}}(t) \end{bmatrix} \tag{4.44}$$

which means that Eq. (4.43) can be written in a first order state space form:

$$\underline{\dot{x}}(t) = \begin{bmatrix} \underline{\underline{0}} & \underline{\underline{I}} \\ -\underline{\underline{M}}^{-1}\underline{\underline{K}} & -\underline{\underline{M}}^{-1}\underline{\underline{C}} \end{bmatrix} \underline{x}(t) + \begin{bmatrix} \underline{\underline{0}} \\ \underline{\underline{M}}^{-1}\underline{\underline{S_p}} \end{bmatrix} \underline{g}(t) \tag{4.45}$$

$$= \underline{\underline{A_c}}\,\underline{x}(t) + \underline{\underline{B_c}}\,\underline{g}(t) \tag{4.46}$$

Subscript c indicates that the equation is on continuous form. A discrete state prediction can be obtained from the state space equation. This is made from a zero-order hold assumption which presumes a constant load throughout a time step.

$$\underline{x}_{k+1} = \underline{\underline{A}}\,\underline{x}_k + \underline{\underline{B}}\,\underline{g}_k + \underline{w}_k \tag{4.47}$$

where

$$\underline{\underline{A}} = e^{\underline{\underline{A_c}}\,dt} \tag{4.48}$$

and

$$\underline{\underline{B}} = \left(\underline{\underline{A}} - \underline{\underline{I}}\right) \underline{\underline{A_c}}^{-1} \underline{\underline{B_c}} \tag{4.49}$$

Here, dt is the sampling time step. We include the process noise $\underline{w}_k$ to account for discrepancies in the relation. More about this noise model later on.

Measurements

Before proceeding to the Kalman filter and load identification, a measurement model must be formed. The measurements are stored in a vector $\underline{z}(t)$. It may be composed of different types of sensors. We consequently need to establish a link between the measurements and the system, so the sensor selection matrices are introduced:

$$\underline{z}(t) = \underline{\underline{S_a}}\,\underline{\ddot{y}}(t) + \underline{\underline{S_v}}\,\underline{\dot{y}}(t) + \underline{\underline{S_d}}\,\underline{y}(t) \tag{4.50}$$

For example, if a displacement sensor is placed in DOF 2 and an accelerometer is placed in DOF 3 this yields the following selection matrices: (Assume that the system has six DOFs in total similar to the model in Examples I and II)

$$\underline{z}(t) = \begin{bmatrix} 0 & 0 & 1 & 0 & 0 & 0 \\ 0 & 0 & 0 & 0 & 0 & 0 \end{bmatrix} \underline{\ddot{y}}(t) + \begin{bmatrix} 0 & 0 & 0 & 0 & 0 & 0 \\ 0 & 1 & 0 & 0 & 0 & 0 \end{bmatrix} \underline{y}(t) \tag{4.51}$$

The size of $\underline{z}(t)$ will then be equal to the number of sensors while the size of the selection matrices depends on the number of sensors and DOFs in the system; $n_{sen} \times n_{dof}$. Next, we need to link the state vector $\underline{x}(t)$ to the measurements $\underline{z}(t)$. This is done by inserting Eq. (4.43) into Eq. (4.50) and rewriting into state space format:

$$\begin{aligned} \underline{z}(t) &= \left[\underline{\underline{S_d}} - \underline{\underline{S_a}}\,\underline{\underline{M}}^{-1}\underline{\underline{K}} \quad , \quad \underline{\underline{S_v}} - \underline{\underline{S_a}}\,\underline{\underline{M}}^{-1}\underline{\underline{C}}\right] \underline{x}(t) + \underline{\underline{S_a}}\,\underline{\underline{M}}^{-1}\underline{\underline{S_p}}\,\underline{g}(t) + \underline{v}(t) \\ &= \underline{\underline{G_c}}\,\underline{x}(t) + \underline{\underline{J_c}}\,\underline{g}(t) + \underline{v}(t) \end{aligned} \tag{4.52}$$

This is often referred to as the observation equation. Again the measurement noise $\underline{v}(t)$ is included to account for discrepancies in the relations.

The transformation from continuous time to discrete time is straightforward by changing the $t = k\ dt$. The matrices, $\underline{\underline{G_c}}$ and $\underline{\underline{J_c}}$ remain the same.

$$\underline{z}_k = \underline{\underline{G_c}}\ \underline{x}_k + \underline{\underline{J_c}}\ \underline{g}_k + \underline{v}_k \tag{4.53}$$

Augmented state space

Since the load scaling, $\underline{g}(t)$, is the target for this exercise, it needs to be merged into the state vector (as this is the output estimate from the Kalman filter). This is done by expanding the discrete state vector as follows:

$$\underline{x}^a_k = \begin{bmatrix} \underline{x}_k \\ \underline{g}_k \end{bmatrix} \tag{4.54}$$

here, superscript a indicates augmented/expanded state vector. Eq. (4.47) can now be rewritten in augmented form as:

$$\underline{x}^a_{k+1} = \begin{bmatrix} \underline{\underline{A}} & \underline{\underline{B}} \\ \underline{\underline{0}} & \underline{\underline{I}} \end{bmatrix} \underline{x}^a_k + \begin{bmatrix} \underline{w}_k \\ \underline{\eta}_k \end{bmatrix} \tag{4.55}$$

$$= \underline{\underline{A}}^a\ \underline{x}^a_k + \underline{\zeta}^a_k \tag{4.56}$$

The size of the null matrix, $\underline{\underline{0}}$ is $n_{loads} \times 2n_{dof}$. Here, we assume that the load is constant throughout the time step and that variations only come from the noise process $\underline{\eta}_k$. That is:

$$\underline{g}_{k+1} = \underline{g}_k + \underline{\eta}_k \tag{4.57}$$

Here, $\underline{\eta}_k$ is also assumed to be a Gaussian variable leaving Eq. (4.57) similar to a random walk. In case of a single input, $\underline{g}_k$ and $\underline{\eta}_k$ thus become scalars.

The measurement transformation matrices $\underline{\underline{G_c}}$ and $\underline{\underline{J_c}}$ also need to be rewritten into augmented form.

$$\underline{z}_k = \begin{bmatrix} \underline{\underline{G_c}} & , & \underline{\underline{J_c}} \end{bmatrix} \underline{x}^a_k + \underline{v}_k \tag{4.58}$$

$$= \underline{\underline{H}}^a\ \underline{x}^a_k + \underline{v}_k \tag{4.59}$$

here, $\underline{\underline{H}}^a$ is the augmented state to measurement matrix.

Noise

As promised, we now turn our focus to the noise models. To accommodate the format of the Kalman filter, we need to establish the covariance matrices for the noise processes. Normally we assume uncorrelated Gaussian noise for all processes, in the sense that each process is uncorrelated with the other processes and each instance of time is uncorrelated to the other instances of time for each noise process. However, the noise/random walk for the load may show correlation with previous time steps, but let us just assume that it does not. The covariance matrix for the augmented state noise $\underline{\underline{Q}}^a$ reads:

$$\underline{\underline{Q}}^a = \mathrm{E}\left[\underline{\zeta}_k^a \, \underline{\zeta}_k^{aT}\right] \tag{4.60}$$

$$\approx \begin{bmatrix} \underline{\underline{Q}} & \underline{\underline{0}} \\ \underline{\underline{0}} & \underline{\underline{S}} \end{bmatrix} \tag{4.61}$$

The $\underline{\underline{Q}}$ part relates to the state process noise and the $\underline{\underline{S}}$ relates to the load noise. $\underline{\underline{Q}}$ and $\underline{\underline{S}}$ are both diagonal matrices since the noise processes are assumed to be uncorrelated. The magnitude of $\underline{\underline{S}}$ must be much greater than $\underline{\underline{Q}}$ in order for the filter to perform well on load identification when sharp variations may be present. The covariance matrix for the measurement noise likewise becomes:

$$\underline{\underline{R}} = \mathrm{E}\left[\underline{v}_k \, \underline{v}_k^T\right] \tag{4.62}$$

here, $\underline{\underline{R}}$ is also a diagonal matrix. The magnitude of $\underline{\underline{R}}$ should be ranging between $\underline{\underline{Q}}$ and $\underline{\underline{S}}$ depending on the sensor noise level and model accuracy.

Kalman filter implementation

The linear Kalman filter [27] is used for the state estimate given a response measurement. Figure 4.7 shows the loop within the Kalman filter algorithm. The augmented state matrix $\underline{\underline{A}}^a$ and measurement transformation matrix $\underline{\underline{H}}^a$ remain constant for all time steps k. Meanwhile the Kalman gain matrix $\underline{\underline{K}}_k^a$ and error covariance matrix $\underline{\underline{P}}_k^a$ are updated for each time step.

Regarding the initial conditions - if no knowledge exists on the content of the system state $\underline{x}_0^a$ at time zero, the initial error covariance matrix $\underline{\underline{P}}_0^a$ should be increased, giving more emphasis to the measurement for the first time steps. We do not want to go into detail on the derivation of the Kalman filter, but it is worth mentioning that only the system state at one previous time step is

used along with the system matrices. This approach allows for a computational efficient and real-time implementation.

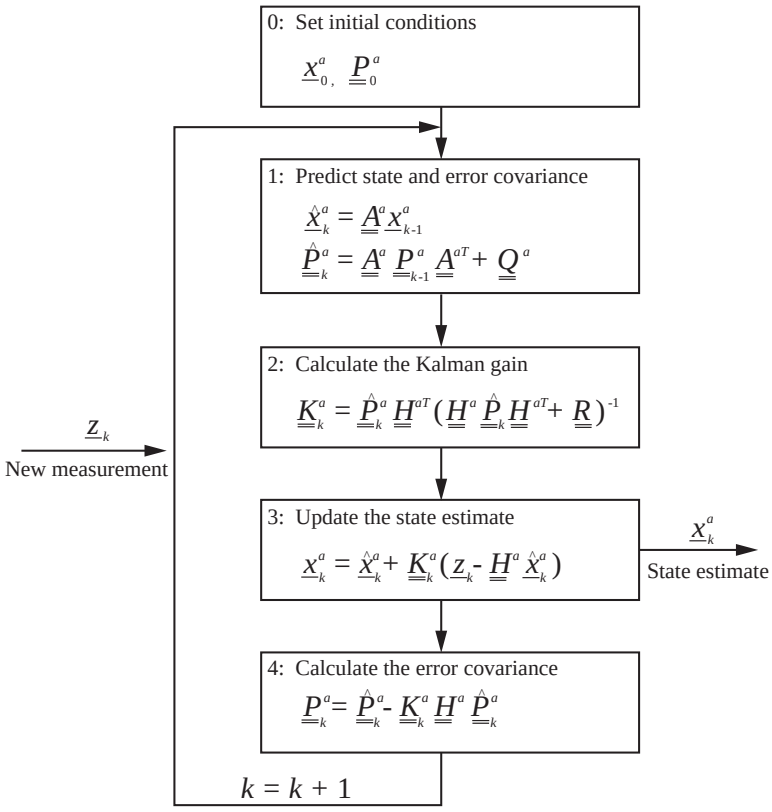

Figure 4.7: Linear Kalman filter with augmented state vector. The figure is made with inspiration from [29].

Example III

Here, an example will be introduced using the augmented state estimation method as presented in Section 4.6. The same six-DOF cantilever beam as introduced in Example I will be reused. Here a scenario with loading at a single node will be considered as shown in Figure 4.8. Again, the FE model provides the mass-, stiffness- and damping matrices. The loading is selected such that both a dynamic and quasi-static response occur. The response due to a loading history is simulated using a Newmark solver and noise is added to the response and thus considered as the "measured" signal. In this example, we will assume that only the translations are measured at each node.

We will assume that the spatial distribution of the load is known. Since only one load source is present, the load spatial distribution matrix becomes a vector:

$$\underline{S_p} = [\, 0\ 0\ 1\ 0\ 0\ 0\,]^T \tag{4.63}$$

Displacements sensors are located at DOF 1, DOF 3 and DOF 5, which yields

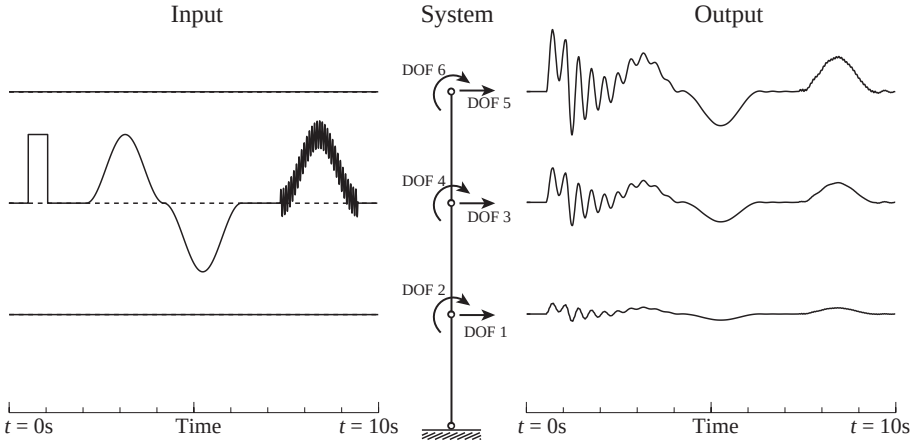

Figure 4.8: Simulated system for example. The dashed lines indicate moment while the solid lines indicate the force and corresponding displacements. A flat line corresponds to zero loading and zero response. Only the horizontal translations are measured and hence the nodal rotations are not shown in the output.

the displacement selection matrix:

$$\underline{\underline{S_d}} = \begin{bmatrix} 1 & 0 & 0 & 0 & 0 & 0 \\ 0 & 0 & 1 & 0 & 0 & 0 \\ 0 & 0 & 0 & 0 & 1 & 0 \end{bmatrix} \tag{4.64}$$

The acceleration and velocity selection matrices will be zero-matrices with the same size as $\underline{\underline{S_d}}$. This yields an (augmented) state-to-measurement transformation matrix as

$$\underline{\underline{H}}^a = \begin{bmatrix} 1 & 0 & 0 & 0 & 0 & 0 & 0 & 0 & 0 & 0 & 0 & 0 & 0 \\ 0 & 0 & 1 & 0 & 0 & 0 & 0 & 0 & 0 & 0 & 0 & 0 & 0 \\ 0 & 0 & 0 & 0 & 1 & 0 & 0 & 0 & 0 & 0 & 0 & 0 & 0 \end{bmatrix} \tag{4.65}$$

Here, $\underline{\underline{H}}^a \in \mathbb{R}^{n_{sen} \times (2n_{dof} + n_{loads})}$, where n_{sen} is the number of sensors, n_{dof} is the number of degrees of freedom in the system and n_{loads} is the number of load sources.

The augmented noise covariance matrix is a user input and may be based on experience. In this case we will assume that the noise is uncorrelated yielding a diagonal covariance matrix.

$$\underline{\underline{Q}}^a = \begin{bmatrix} 10 & 0 & 0 & 0 & 0 & 0 & 0 \\ 0 & 10 & 0 & 0 & 0 & 0 & 0 \\ 0 & 0 & 10 & 0 & 0 & 0 & 0 \\ 0 & 0 & 0 & 10 & 0 & 0 & 0 \\ 0 & 0 & 0 & 0 & 10 & 0 & 0 \\ 0 & 0 & 0 & 0 & 0 & 10 & 0 \\ 0 & 0 & 0 & 0 & 0 & 0 & S \end{bmatrix} \tag{4.66}$$

Here, $\underline{\underline{Q}}^a \in \mathbb{R}^{(n_{dof} + n_{loads}) \times (n_{dof} + n_{loads})}$. The last element, S, is the covariance on the load. In comparison to the modelling noise, this must be selected high in order to identify sharp variations in the load. The result will be presented from three different choices of this value.

The measurement covariance is selected as follows:

$$\underline{\underline{R}} = \begin{bmatrix} 10^3 & 0 & 0 \\ 0 & 10^3 & 0 \\ 0 & 0 & 10^3 \end{bmatrix} \tag{4.67}$$

where, $\underline{\underline{R}} \in \mathbb{R}^{n_{sen} \times n_{sen}}$. Along with the system matrices, $\underline{\underline{M}}$, $\underline{\underline{C}}$ and $\underline{\underline{K}}$, these are all the information needed for the load identification. These are fed into the

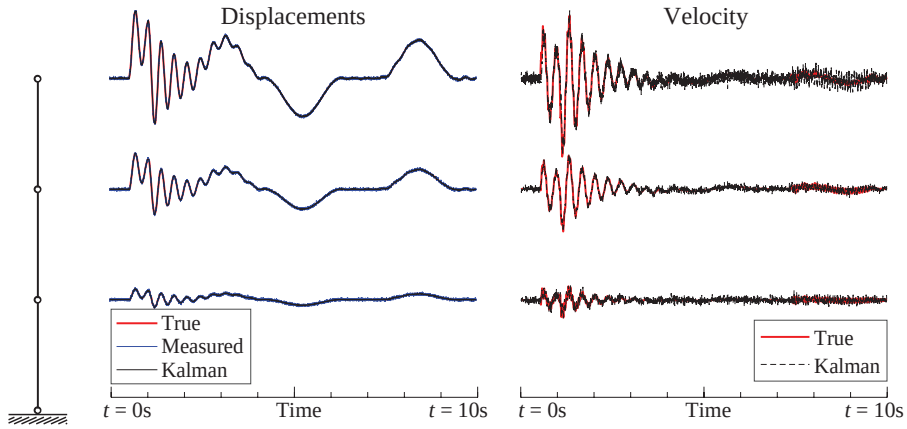

Figure 4.9: State estimate using a Kalman filter.

Kalman filter and an augmented state estimate is returned real-time. Besides the load estimate, the state vector also includes displacements and velocities. These are plotted in Figure 4.9 along with the true value. The load estimate is shown in Figure 4.10 for three different values of the load covariance, S. It

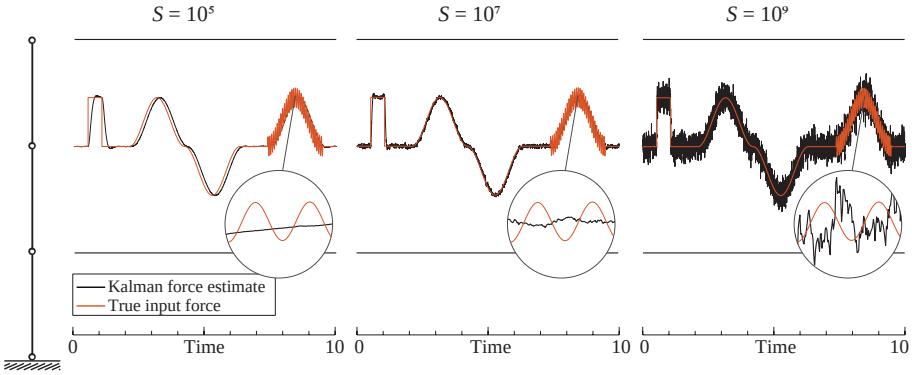

Figure 4.10: Identified load from the augmented state identification method using different magnitudes of the load covariance S. All are based on a known spatial distribution and complete system matrices.

is seen that the Kalman filter smoothens the estimates, which yields a poor estimate on the high frequency harmonic load. (Load frequency between 1^{st} and 2^{nd} mode) A small time lag between the input load and the estimated load is also observed. The method, however, is computational efficient and handles measurement noise well. The greatest benefit, however, is the capability of merging different sensors.

4.7 Principle of wave load identification

The load identification outlined in Sections 4.3 to 4.6 shows the principles in a general framework. This section will describe how the identification process can be implemented for an offshore structure. Imagine that we wish to include wave load identification as part of an SHM procedure for an existing platform such as the wellhead structure, Valdemar BA in the North Sea. The implementation of the load identification procedure is shown by two separated workflows given by Figure 4.11 and Figure 4.12. The first step is system identification, and the second step is load identification. The two steps are carried out under different environmental conditions as symbolized by the photos in the left-hand side of the flow charts. NB, the images show two different platforms. These are merely showcasing the principle of varying loading conditions. The load identification must naturally be conducted on the same structure as was used for the system identification.

Step 1/2: The system response is measured under operational conditions suited for OMA. This implies that the loading must be random both in terms of time and space. The ambient vibration will here be caused by waves, wind, and other operational sources. Once sufficient data are collected, OMA can be performed and modal parameters, such as mode shapes, natural frequencies, and damping ratios can be obtained. Ideally, this is implemented in an automated fashion allowing for continuous system identification.

Valdemar BA 2006
Danish continental shelf, Mærsk.
Photo courtesy of Mærsk Oil

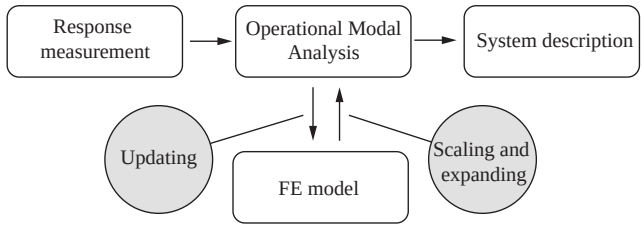

Figure 4.11: Step 1/2: Flowchart for the system identification process.

There are three immediate challenges which must be considered. 1) Often, the sensor layout will be limited by the number of sensors and be restricted to the topside. 2) Scaling of the mode shapes is unavailable from classical OMA. 3) If accelerometers are used, noise may mask the low-frequency movements. The first two can be mitigated by the use of a surrogate FE model. The model can be used for optimal sensor positioning, and it can be used for scaling and expansion of the mode shapes, thus allowing for an estimation of the subsea response. The FE model must be continually updated to reflect the dynamics of the structure, including the added effect from the sea, e.g., mass loading. The third challenge concerning the static displacements is not covered in this work, but sensor fusion using GPS is seen as mitigation.

At the end of this procedure, verified modal parameters for the actual conditions are available, and an identification modelling can be initiated.

Step 2/2: At a later stage in time, the structure may experience storm conditions yielding wave loading that we wish to quantify. We assume that the system parameters that we previously obtained are still valid during the storm and that the response is linear. The vibration response is then measured while the system description is used to deconvolute the response into an estimate on the load. Due to the underdetermined nature of the problem, the load identification must be constrained. Accordingly, this is performed by introducing a load model. This load model may be formed based on the given situation. For wave loading, the model can be based on information on the

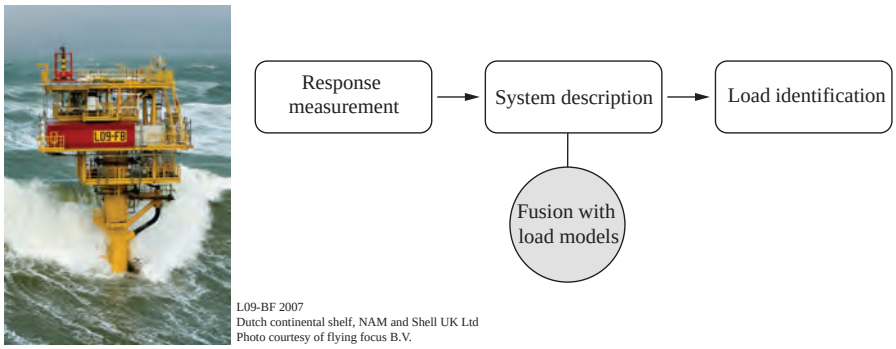

Figure 4.12: Step 2/2: Flowchart for the wave load identification.

sea elevation, frequency content, or semi-analytical models using wave theory. The load models can be supported by other sensors like wave gauges, Radar, LIDAR, or velocimeter depending on the nature of the problem. The attached papers addressing specifically the wave load identification are: Papers V, VI, VII, and VIII.

Chapter 5

Conclusion

In this study, indirect methods for wave load identification have been examined. It was chosen to rely on output-only system identification, which allows for easy implementation offshore. During the work, different aspects of the application were studied in detail. Although we did not manage to cover all aspects, some conclusions can still be drawn. When structures are placed in the sea, the dynamics will be affected by interaction effects. Some of the interaction effects were shown in paper IV. Here it was presented how the modal parameters changed due to the influence of water. The presence of surrounding water, however, did not affect all modes equally, which caused reordering in some cases. When affected modes were transcending the unaffected modes, we saw exchanges within the subspace of their mode shapes. In paper VII, the interaction effect through the dynamic pressure distribution on the flexible cantilever was studied. It was seen that the analytical formulae deviate once interaction effects are present.

For offshore structures, the wave loading occurs in the splash zone or subsea while the sensors are safely located at the topside. This calls for a transfer function to interpret the link between the load and the response measurements. This was solved by expanding the mode shapes and thus obtaining means for estimating the response at the subsea location. Having this "virtual sensing" omitted the need for analytical transfer functions. The task of identifying the input loads has been targeted from three different domains: The estimates obtained in the frequency domain require that the complete time series is available before the identification can be made. If the input includes both low- and high-frequency content, then the frequency domain approach was most consis-

tent. The method originates from the automotive and aviator industry and can be established from both EMA or OMA. The method can be computationally demanding when treating a large system at long time signals. A noise filter should typically assist the process.

In modern identification problems, identification in the time domain has become wildly used. The method extends the state estimation technique where a Kalman filter combines a predicted system state with measurements and provides a joint estimate considering the uncertainty of both model and measurements. The state-space formulation and state-to-measurement transformation allow merging of different sensors into a combined state estimate. The formulation is rewritten such that the load scalar becomes part of the state vector. The method is then renamed as augmented state estimate. This method performs the state estimate (and hence the load estimate) one time step at a time. The process can accordingly be implemented at real-time with little computational strain. The estimates following this method are a mix between a predicted and a measured and consequently assigned to the same properties as of a lowpass filter.

When monitoring an offshore structure to determine the wave loads, discretization must be considered. The structure will have an infinite number of degrees of freedom. The response (vibrations) are perhaps measured at a few tens of locations. This yields an incomplete description of the structural behavior. The loads, on the other hand, may act on the entire structure, or may work at a single location. The exact location is, in most cases, unknown. The underdeterminacy of the problem produces multiple solutions (load estimates), which yield nearly the same response - or at least within the noise level and truncated sensor resolution.

> *"In actual fact we should recognise the general principle that a lack of information cannot be remedied by any mathematical trickery"* - Cornelius Lanczos [31]

The inverse problem was supported by assuming a fixed spatial distribution of the load. This hence reduced the identification problem to determining a scalar function. For wave loading, the spatial distribution was derived from wave gauges and supported by wave theory. We have shown that wave loads can be identified with reasonable accuracy for a few selected cases (papers V-VIII). However, for full-scale implementation, a verification program should be considered - for instance, a pull-test or similar artificial excitation, which can

verify the indirect estimates.

In theory, if a complete system description is available, loads can be determined at perfect accuracy using indirect methods. In practice, however, there is a limitation to this accuracy. When noise and modal truncation errors are introduced, the accuracy drops dramatically. In paper VII, a complicated case study revealed that even under ideal conditions, indirect methods could not distinguish between an equivalent point load and distributed line loads. The indirect load estimate, thus remain an estimate for all practical purposes concerning wave loading on offshore structures.

5.1 Future work

The work covered by this thesis does not encompass all aspects of (wave) load identification. This section will outline some of the most fundamental assumptions or limitations to the study and which could be considered for future works.

The proposed implementation of the load identification is based on two separate parts: a system identification step and a load identification step. One of the two most significant assumptions is that the structure does not change between the two stages. It is known that a structure which experiences changes in temperature will also yield a change in dynamic behavior. This change, if present, may influence the dynamics. In extreme cases, wave loading may introduce non-stationary added mass and damping. The effect from this is of unknown magnitude and should be evaluated. Likewise, for extreme cases, the response may not be linear, which is the second fundamental assumption. Tilting effects and large deflections may also challenge the measurements.

The structural system which has been studied assembles a monopile structure. More complex structures, where several members are loaded by wave forces with a difference in phase, may yield an interesting case study. This will be the natural conditions for jacket structures or multi-legged structures.

The coupling effect between the sea and the structure should be evaluated further, and more work should be put into determining the load distribution. Cases of multidirectional loading should also be evaluated while emphasis should be placed into identifying impact wave loads from a random sea.

Finally, considerations should be put towards the automation of the process with quantification of the uncertainty.

Bibliography

[1] Aenlle, M. and Brincker, R. [2013], 'Modal scaling in operational modal analysis using a finite element model', *International Journal of Mechanical Sciences* **76**, 86–101. 21

[2] Aenlle, M., Brincker, R. and Canteli, A. [2005], 'Load estimation from natural input modal analysis', *Proceedings of the International Modal Analysis Conference, IMAC* . 17

[3] Antoniadou, I., Dervilis, N., Papatheou, E., Maguire, A. and Worden, K. [2015], 'Aspects of structural health and condition monitoring of offshore wind turbines', *Philosophical Transactions of the Royal Society A: Mathematical, Physical and Engineering Sciences* **373**. 18

[4] Atkins, N., Lyons, R. and Rainey, R. [1995], 'Summary of findings of wave load measurements on the tern platform', *UK Health and Safety Executive Report, OTH 467* . 18

[5] Augustyn, D., Tygesen, U., Ulriksen, M. and Sørensen, J. [2019], 'Data-driven design and operation of offshore wind structures', *Proceedings of the International Ocean and Polar Engineering Conference, ISOPE* . 18

[6] Bartlett, F. and Flannelly, W. [1979], 'Model verification of force determination for measuring vibratory loads', *Journal of the American Helicopter Society* **24**(2), 10–18. 15

[7] Begg, R., Mackenzie, A., Dodds, C. and Loland, O. [1976], 'Structural integrity monitoring using digital processing of vibration signals', *Proceedings of the Offshore Technology Conference, Houston, Texas* . 16

[8] Brandt, A. [2011], *Noise and Vibration Analysis*, John Wiley and Sons, Ltd, West Sussex, UK. 23

[9] Brandt, A., Berardengo, M., Manzoni, S. and Cigada, A. [2017], 'Scaling of mode shapes from operational modal analysis using harmonic forces', *Journal of Sound and Vibration* **407**, 128–143. 21

[10] Brincker, R. and Andersen, P. [2003], 'A way of getting scaled mode shapes in output only modal testing', *Proceedings of the International Modal Analysis Conference, IMAC* pp. 141–145. 21

[11] Brincker, R. and Ventura, C. [2015], *Introduction to Operational Modal Analysis*, John Wiley and Sons, Ltd, Chichester, West Sussex, UK. 20, 23

[12] Brincker, R., Ventura, C. and Andersen, P. [2003], 'Why output-only modal testing is a desirable tool for a wide range of practical applications', *Proceedings of the Internatinoal Modal Analysis Conference IMAC* . 16

[13] Chella, M. A., Tørum, A. and Myrhaug, D. [2012], 'An overview of wave impact forces on offshore wind turbine substructures', *Energy Procedia* . 12

[14] Det Norske Veritas [2010*a*], *Offshore Standard, DNV-OS-J101, Design of Offshore Wind Turbine Structures.* 7

[15] Det Norske Veritas [2010*b*], *Recomended Practice, DNV-RP-C205, Enviromental Conditions and Enviromental Loads.* 10

[16] Det Norske Veritas [2011], *Recomended Practice, DNV-RP-H103, Modelling and Analysis of Marine Operations.* 7

[17] Dobson, B. and Rider, E. [1990], 'A review of the indirect calculation of excitation forces from measured structural data', *Proceedings of the Institution of Mechanical Engineers, Part C: Mechanical Engineering Science* **204**, 69–75. 15, 17

[18] Fabunmi, J. [1986], 'Effects of structural modes on vibratory force determination by the pseudoinverse technique', *American Institute of Aeronautics and Astronautics Journal* **24**, 504–509. 15, 17

[19] Fallais, D., Voormeeren, S. and Lourens, E. [2016], 'Vibration-based identification of hydrodynamic loads and system parameters for offshore wind turbine support structures', *Proceedings of Deep Sea Offshore Wind R&D Conference, EERA DeepWind 2016, Trondheim, Norway* . 17

[20] Farrar, C. and Worden, K. [2013], *Structural Health Monitoring*, John Wiley and Sons, Ltd, Chichester, West Sussex, UK. 18

[21] Flannelly, W., Bartlett, F. and Fonsberg Jr, T. [1977], *Laboratory Verification of Force Determination, A Potential Tool for Reliability Testing*, Kaman Aerospace Corporation, Old Windsor Road, Bloomfield Conn. 15, 17

[22] Fritzen, C. and Klinkov, M. [2014], 'Load identification for structural health prognosis', *North Atlantic Treaty Organization, NATO - Science and Technology Organization* . 16

[23] Giansante, N., Jones, R. and Calapodas, N. [1982], 'Determination of in-flight helicopter loads', *Journal of the American Helicopter Society* **27**(3), 58–64. 15

[24] Hillary, B. [1983], *Indirect Measurement of Vibration Excitation Forces*, PhD Thesis, Imperial College of Science and Technology, London. 15, 17

[25] Hwang, J., Kareem, A. and Kim, W. [2009], 'Estimation of modal loads using structural response', *Journal of Sound and Vibration* **326**, 522–539. 16

[26] Jensen, J., Kirkegaard, P. H. and Brincker, R. [1992], 'Modal and wave load identification by ARMA calibration', *Journal of Engineering Mechanics* . 12, 17

[27] Kalman, R. [1960], 'A new approach to linear filtering and prediction problems', *Journal of Basic Engineering* **82**, 35–45. 16, 34, 37

[28] Khatibi, M., Ashory, M. and Malekjafarian, A. [2010], 'Mass-stiffness change method for scaling of operational mode shapes: Experimental results', *Proceedings of the International Modal Analysis Conference, IMAC* pp. 1569 – 1577. 21

[29] Kim, P. [2011], *Kalman filter for beginners - with Matlab examples*, CreateSpace Independent Publishing Platform, Scotts Valley, California , US. 38

[30] Kvitrud, A. and Løland, A. [2018], 'Observed wave actions on norwegian semi-submersible and tlp decks', *Proceedings of the 37th International Conference on Ocean, Offshore and Arctic Engineering, OMAE* . 9

[31] Lanczos, C. and Malley, R. O. [1961], *Linear Differential Operators*, 1st edn, D.Van Nostrand Company Inc. 48

[32] Liu, J., Ma, C., Kung, I. and Lin, D. [2000], 'Input force estimation of a cantilever plate by using a system identification technique', *Computer Methods in Applied Mechanics and Engineering* **190**, 1309–1322. 16

[33] Liu, Y. and Shepard, W. [2005], 'Dynamic force identification based on enhanced least squares and total least-squares scheme in the frequency domain', *Journal of Sound and Vibration* **282**, 37–60. 17

[34] Loland, O. and Dodds, C. [1976], 'Experiences in developing and operating integrity monitoring systems in the North Sea', *Proceedings of the Offshore Technology Conference, Houston, Texas* pp. 313–319. 16

[35] Lourens, E. and Fallais, D. [2019], 'Full-field response monitoring in structural systems driven by a set of identified equivalent forces', *Mechanical Systems and Signal Processing* **114**, 106–119. 34

[36] Lourens, E., Reynders, E., De Roeck, G., Degrande, G. and Lombaert, G. [2012], 'An augmented Kalman filter for force identification in structural dynamics', *Mechanical Systems and Signal Processing* **27**, 446–460. 34

[37] Ma, C., Chang, J. and Lin, D. [2003], 'Input forces estimation of beam structures by an inverse method', *Journal of Sound and Vibration* **259**, 387–407. 16, 17

[38] Maddox, N. R. [1975], 'On the number of modes necessary for accurate response and resulting forces in dynamic analyses', *Journal of Applied Mechanics* **42**, 516–517. 15, 17

[39] Maes, K., Iliopoulos, A., Weijtjens, W., Devriendt, C. and Lombaert, G. [2016], 'Dynamic strain estimation for fatigue assessment of and offshore monopile wind turbine using filtering and modal expansion algorithms', *Mechanical Systems and Signal Processing* **76-77**, 592–611. 12, 16

[40] Maes, K., Smyth, Q., De Roeck, G. and Lombaert, G. [2016], 'Joint input-state estimation in structural dynamics', *Mechanical Systems and Signal Processing* **70-71**, 445–466. 17

[41] Maes, K., van Nimmen, K., Lourens, E., Rezayat, A., Guillaume, P. and Roeck, G. D. [2016], 'Verification of joint input-state estimation for force

identification by means of in situ measurements on a footbridge', *Mechanical Systems and Signal Processing* **75**, 245–260. 16

[42] Maes, K., Weijtjens, W., de Ridder, E. and Lombaert, G. [2018], 'Inverse estimation of breaking wave loads on monopile wind turbines', *Ocean Engineering* **163**, 544–554. 16, 17

[43] Morison, J., O'Brien, M., Johnson, J. and Schaaf, S. [1950], 'The force exerted by surface waves on piles', *Petroleum Transactions, American Institute of Mining Engineers* pp. 149–154. 11

[44] Naets, F., Cuadrado, J. and Desmet, W. [2015], 'Stable force identification in structural dynamics using Kalman filter and dummy-measurements', *Mechanical Systems and Signal Processing* **50-51**, 235–248. 16

[45] Nataraja, R. [1983], 'Structural integrity monitoring in real seas', *Proceedings of the Offshore Technology Conference, Houston, Texas* pp. 221–228. 16

[46] Newland, D. E. [1993], *An Introduction To Random Vibrations, Spectral and Wavelet Analysis*, 3rd edn, Dover Publications, Inc. 30

[47] Noppe, N., Iliopoulos, A., Weijtjens, W. and Devriendt, C. [2016], 'Full load estimation of and offshore wind turbine based on SCADA and accelerometer data', *Journal of Physics Conference Series* **753**. 12, 18

[48] O'Callahan, J., Avitabile, P. and Riemer, R. [1989], 'System equivalent reduction expansion process', *Proceedings of the International Modal Analysis Conference, IMAC* . 22

[49] Ollestad, I., Andersen, T., Orma, N. and Zachariassen, S. [2016], 'Investigation of an incident with fatal consequences on coslinnovator, 30 december 2015', *Petroleumstilsynet report* p. Activity number 418005005. 9

[50] Parloo, E., Verboven, P., Guillaume, P. and van Overmeire, M. [2003], 'Force identification by means of in-operation modal models', *Journal of Sound and Vibration* **262**, 161–173. 17

[51] Penrose, R. [1955], 'A generalized inverse for matrices', *Mathematical Proceedings of the Cambridge Philosophical Society* **51**, 406–413. 26

[52] Perisic, N., Kirkegaard, P. H. and Tygesen, U. [2014], 'Load identification of offshore platform for fatigue life estimation', *Structural Health Monitoring* **5**, 99–109. 12, 17, 18

[53] Perisic, N. and Tygesen, U. [2014], 'Cost-effective load monitoring methods for fatigue life estimation of offshore structures', *Proceedings of the International Conferences on Ocean, Offshore and Arctic Engineering OMAE* . 18

[54] Petersen, W., Øiseth, O. and Lourens, E. [2019], 'Full-scale identification of wave forces exerted on a floating bridge using inverse methods and directional wave spectrum estimation', *Mechanical Systems and Signal Processing* **120**, 708–726. 17

[55] Rainieri, C. and Fabbrocino, G. [2014], *Operational modal analysis of civil engineering structures*, Springer, New York. 20

[56] S.Hallowell, Myers, A. and Arwade, S. [2016], 'Variability of breaking wave characteristics and impact loads on offshore wind turbines supported by monopiles', *Wind Energy* **19**, 301–312. 12

[57] Skafte, A., Tygesen, U. and Brincker, R. [2014], 'Expansion of mode shapes and responses on the offshore platform valdemar', *Proceedings of the Internatinoal Modal Analysis Conference IMAC* **4**, 35–41. 22

[58] Stevens, K. [1987], 'Force identification problems - an overview', *Proceedings of the SEM Spring Conference on Experimental Mechanics* pp. 838–844. 15, 16, 17

[59] Tarpø, M., Vigsø, M. and Brincker, R. [2018], 'Modal truncation in experimental modal analysis', *Proceedings of the International Modal Analysis Conference, IMAC* pp. 143–152. 59

[60] Tychsen, J. and Dixen, M. [2016], 'Wave kinematics and hydrodynamic loads on intermediate water depth structures inferred from systematic model testing and field observations – tyra field extreme wave study 2013-15', *Offshore Structural Reliability Conference, OSRC* . 9

[61] Tychsen, J., Risvig, S., Hansen, H., Hansen, N. and Stevanto, F. [2016], 'Summary of the impact on structural reliability of the findings of the tyra field extreme wave study 2013-15', *Offshore Structural Reliability Conference, OSRC* . 9

[62] Tygesen, U., Jepsen, M., Vestermark, J., Dollerup, N. and Pedersen, A. [2018a], 'The true digital twin concept for fatigue re-assessment of marine structures', *Proceedings of the 37th International Conference on Ocean, Offshore and Arctic, ASME* . 18

[63] Tygesen, U., Worden, K., Rogers, T., Manson, G. and Cross, E. J. [2018b], 'State-of-the-art and future directions for predictive modelling of offshore structure dynamics using machine learning', *Proceedings of the International Modal Analysis Conference, IMAC* . 18

[64] Vigsø, M., Brincker, R. and Georgakis, C. [2019], 'Evaluating the effect of modelling errors in load identification using classical identification methods', *Shock and Vibration* **2019**, Article ID 9490760. 59

[65] Vigsø, M. and Georgakis, C. [2020], 'Estimating loads from breaking waves using operational modal analysis', *Proceedings of the International Conferences on Ocean, Offshore and Arctic Engineering OMAE* p. 19170. 59

[66] Vigsø, M., Kabel, T., Tarpø, M., Brincker, R. and Georgakis, C. [2018], 'Operational modal analysis and fluid-structure interaction', *Proceedings of the International Conference on Noise and Vibration Engineering, ISMA* . 59

[67] Vigsø, M., Tarpø, M., Hansen, J., Brincker, R. and Georgakis, C. [2018], 'Scenario based approach for load identification', *Proceedings of the International Modal Analysis Conference, IMAC* pp. 117–125. 59

[68] Vigsø, M., Brincker, R. and Georgakis, C. [2019*a*], 'The effect of modal truncation and spatial distribution in load identification', *Proceedings of the International Operational Modal Analysis Conference, iomac* . 59

[69] Vigsø, M., Brincker, R. and Georgakis, C. [2019*b*], 'Identifying wave loads during random seas using structural response', *Proceedings of the International Ocean and Polar Engineering Conference, ISOPE* . 59

[70] Vigsø, M., Kristoffersen, J., Brincker, R. and Georgakis, C. [2018], 'Indirect wave load estimates using operational modal analysis – preliminary findings', *Proceedings of the International Ocean and Polar Engineering Conference, ISOPE* . 59

[71] Wambacq, J., Maes, K., Rezayat, A., Guillaume, P. and Lombaert, G. [2019], 'Localization of dynamic forces on structures with an interior point

method using group sparsity', *Mechanical Systems and Signal Processing* **115**, 593–606. 17

[72] Wheeler, J. [1969], 'Method for calculating forces produced by irregular waves.', *Offshore Technology Conference* **1**, 83 – 94. 11

Chapter 6

Publications

6.1 Reading guide

In total eight publications are attached to this thesis. They are written in whole or in part by the author. A short summary and their context relations are outlined prior to each paper. The papers are not listed by chronological order, but as they are intended to be read.

I	Scenario based approach for load identification [67]
II	Evaluating the effect of modelling errors in load identification using classical identification methods [64]
III	Modal truncation in experimental modal analysis [59]
IV	Operational modal analysis and fluid-structure interaction [66]
V	Indirect wave load estimates using operational modal analysis [70]
VI	Identifying wave loads during random seas using structural response [69]
VII	Estimating wave load distribution from structural response
VIII	Estimating loads from breaking waves using operational modal analysis [65]

In addition, following publications were produced yet not attached to this thesis.

IX	The effect of modal truncation and spatial distribution in load identification [68]

Chapter 7

Identifying impact loads

Paper I

"Scenario based approach for load identification"

Michael Vigsø, Marius Tarpø, Jannick Hansen, Rune Brincker and Christos Georgakis

Published in Proceedings of the 36$^{\text{th}}$ International Modal Analysis Conference, IMAC, Orlando, 2018

This chapter presents the author's first study on load identification. The identification is driven by scenarios and once the correct loading scenario is identified, then the loading can be quantified. The author has performed the main part of the ideation, experiments, analysis and the writing of the paper. Marius Tarpø contributed to the success of the experiments while Rune Brincker contributed to the ideation. The paper has been formatted with minor grammatical adjustments to suit this thesis.

Scenario based approach for load identification

Michael Vigsø[a,*], Marius Tarpø[a], Jannick B. Hansen[a], Rune Brincker[b], Christos Georgakis[a]

[a] *Aarhus University, Inge Lehmanns Gade 10, 8000 Aarhus, Denmark*
[b] *Technical University of Denmark, Brovej 118, 2800 Kgs. Lyngby, Denmark*

Abstract

In output only analysis, the load identification has been a puzzle for several years. Different techniques have been proposed to cope with the inversion problem that lies within this field. However, it has been shown that most methods struggle to obtain robust and consistent results in cases of modal truncation and noise contaminated signals. In light of these challenges, a scenario based method is proposed. This approach utilizes model updating along with mode shape expansion to obtain a reliable numerical model of the given structure. Then, by evaluating a series of rational load scenarios, it is possible to obtain a reasonable input identification – both the spatial distribution and the temporal variation of the load. The method is demonstrated numerically and experimentally.

Keywords: System identification, Operational modal analysis, Response estimation, Modal truncation, FE updating

Nomenclature

Vectors are noted by a single underline and matrix by a double underline. Superscript* indicates complex conjugated while superscript ˆ is an approximation.

$\dagger$	Moore Penrose pseudo inverse	$\underline{y}(t)$	Displacements
ω_r	Natural frequency of mode r	$\underline{q}(t)$	Modal coordinates
ζ_r	Damping ratio of mode r	$\underline{Y}(\omega)$	Fourier transformed of $\underline{y}(t)$
$\underline{\underline{\Phi}}$	Mode shapes arranged in columns	$\underline{C}(\omega)$	Fourier transformed of $\underline{c}(t)$
λ_r	Pole of mode r	$G(\omega)$	Fourier transformed of $g(t)$
ε	RMS error	$\underline{\underline{H}}(\omega)$	Frequency response function
Q_r	Modal scaling constant for mode r		
$\underline{f}(t)$	Force		
$\underline{f}_0$	Spatial distribution of load		
$g(t)$	Scaling function of load		
$\underline{\underline{h}}(t)$	Impulse response function		

*Corresponding author
Email addresses: mvigso@eng.au.dk (Michael Vigsø), martar@eng.au.dk (Marius Tarpø), jbha@ase.au.dk (Jannick B. Hansen), runeb@byg.dtu.dk (Rune Brincker), cg@eng.au.dk (Christos Georgakis)

1. Introduction

Being able to determine the dynamic loading of a mechanical system is of interest in many contexts. In most civil engineering structures, however, it is not feasible to get direct measurements of the dynamic loading and one must rely on indirect methods by measuring the response. Often, however, either due to inaccessibility or to limited amount of sensors, the response of the structure is hardly ever available at all desired locations, which increases the complexity of the problem [1].

Utilizing the concepts of Operational Modal Analysis, OMA, on a structure, it is possible to extract key parameters of the system, which can be used to reconstruct a model representation [2]. Then, by carefully expanding the mathematical formulation of the system, it is possible to estimate the response at locations where it is not feasible to get measurements. By using the expanded mode shapes along with the frequencies and damping ratios obtained from the OMA, one can establish a frequency response function of the system. This yields an inverse identification problem where the number of unknowns exceeds the number of equations and a unique solution cannot be achieved. Methods to cope with this inversion instability have been proposed, either through least square schemes [3] or filtering using singular value decomposition [4]. Since complete dynamic characteristics of the system are rarely available, truncation errors and noise can cause the input estimates to be rather non-physical.

This paper presents a way to improve the load estimate by constraining the inversion problem by evaluating a set of pre-defined load scenarios. The hypothesis is that when evaluating the "correct" load scenario it yields a minimum error. The mode shape expansion provides the option to detect loads at locations where the response is not originally recorded. The method is developed for time invariant systems with linear assumption and small damping.

2. Concept

The main idea in this approach is to assume the load can be written as a product of a spatial distribution, $\underline{f_0}$, and a time dependent scaling function, $g(t) \in \mathbb{R}$.

$$\underline{f}(t) = \underline{f_0}\, g(t) \tag{1}$$

There is nothing novel in making this separation of variables as several authors have already published papers including this approach, e.g. [5–10]. However, the assumption proves to yield robust solutions for load identification. In the time domain, the response of a multi-degree-of-freedom system can be found as a convolution between the impulse response function and the load.

$$\underline{y}(t) = \underline{\underline{h}}(t) \circledast \underline{f}(t) \tag{2}$$

Given that the load, $\underline{f}(t)$, can be written as in equation (1), the response can then be approximated as:

$$\underline{\hat{y}}(t) = \left(\underline{\underline{h}}(t)\ \underline{f_0}\right) \circledast g(t) \tag{3}$$

$$= \underline{\underline{c}}(t) \circledast g(t) \tag{4}$$

The easiest way to evaluate this convolution is in the frequency domain, so by means of the Fourier transform, equation (3) becomes:

$$\hat{\underline{Y}}(\omega) = \left(\underline{\underline{H}}(\omega)\ \underline{f_0}\right)\ G(\omega) \tag{5}$$

$$= \underline{C}(\omega)\ G(\omega) \tag{6}$$

It is then possible to obtain a least square solution for the scaling function, $G(\omega)$.

$$\hat{G}(\omega) = \underline{C}^{\dagger}(\omega)\ \underline{Y}(\omega) \tag{7}$$

By making this formulation, one is omitting the challenges associated with inverting the frequency response function $\underline{\underline{H}}(\omega)$, which very well may be ill posed [1, 4]. Then, by evaluating Eq. (7) and back substituting into Eq. (5), it is possible to obtain an estimate of the response of the system given the load distribution, $\underline{f_0}$, which was chosen initially. This can then be compared to the recorded response and $\underline{f_0}$ can be changed until the error has been minimized.

3. Simulation case

A simulation case is made on a plane cantilever beam. The Bernoulli-Euler beam element formulation is used with two degrees of freedom at each node and a distributed mass. Assuming that the cantilever beam is subjected to loading approaching Gaussian white noise, the modal parameters can be extracted using common OMA approaches [2]. Mode shapes, $\underline{\underline{\Phi}}$, associated frequencies, ω_r, and damping rations, ζ_r, are extracted from the model and are assumed to be of high quality. For the sake of convenience, the damping ratio is assumed to be the same for all modes. Table 1 shows the extracted modal parameters for the first eight modes and their associated damping ratio.

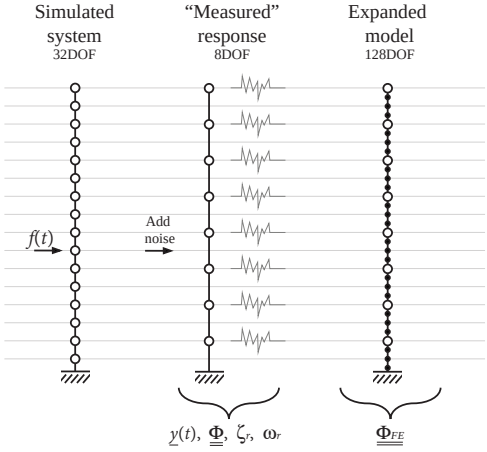

Figure 1: Simulation case setup. Note: only every second node is visible on the expanded model.

Table 1: Extracted modal parameters.

Mode	1	2	3	4	5	6	7	8
Frequency [Hz]	8.32	52.1	146	286	473	707	988	1320
Damping ratio [%]	1.0	1.0	1.0	1.0	1.0	1.0	1.0	1.0

In the current simulation case, the model is subjected to a load at a single node as shown in Figure 1. Responses are extracted from a limited number of nodes in the model, which are considered "measured" or "experimental" responses. Noise is added to the "measured" response in order to stress the algorithm. The level of noise in this case is 100dBW and no filtering is performed.

Often, the load source will be located at a point where no response is recorded. This is also chosen to be the case in this simulation, where the load is acting exactly between two experimental nodes, see Figure 1. In order to estimate the loads at locations where data is not available, the measured response must be expanded to the unknown locations. This is done by a transformation into modal coordinates as follows:

$$\underline{\hat{q}}(t) = \underline{\underline{\Phi}}^{\dagger}\ \underline{y}(t) \tag{8}$$

$$\underline{y_{FE}}(t) = \underline{\underline{\Phi_{FE}}}\ \underline{\hat{q}}(t), \tag{9}$$

where index FE indicates expanded response using Finite Element mode shapes. Several other expansion techniques are available for this task, e.g. SEREP [11] or LC [12], but in this case the FE mode shapes are adopted presuming high correlation between the FE model and the physical model. The size of $\underline{\underline{\Phi_{FE}}}$ is determined by the desired resolution during load identification, but it is limited to the same number of experimentally determined mode shapes.

A new receptance FRF matrix is formed based on the obtained information from the OMA and an updated FE model.

$$\underline{\underline{H}}(\omega) = \sum_{r=1}^{N} \left(\frac{Q_r\, \underline{\psi_r}\ \underline{\psi_r}^T}{i\omega - \lambda_r} + \frac{Q_r^*\, \underline{\psi_r^*}\ \underline{\psi_r^*}^T}{i\omega - \lambda_r^*} \right) \tag{10}$$

where Q_r is a modal scaling constant and $\underline{\psi_r}$ is the expanded and mass normalized mode shape r.

The loading scenarios are now defined as a set of different load distributions, $\underline{f_0}$, and stored in $\underline{\underline{F_0}}$. The distributions can be chosen arbitrarily but for this case say that $\underline{\underline{F_0}}$ is equal to the identity matrix meaning that each column corresponds to a single localized force or moment. That is

$$\underline{\underline{F_0}} = \left[\underline{f_0}^{(1)}, \underline{f_0}^{(2)} \ldots \underline{f_0}^{(N)} \right] = \begin{bmatrix} 1 & 0 & \ldots & 0 \\ 0 & 1 & \ldots & 0 \\ \vdots & \vdots & \ddots & \vdots \\ 0 & 0 & \ldots & 1 \end{bmatrix}_{N \times N} \tag{11}$$

where N is the total number of free degrees of freedom in the system. Then, by evaluating the different distributions, $\underline{f_0}$, one by one, it is possible to get an estimate of the approximated response

corresponding to that distribution, Eq. (5) to (7). Letting the error on the estimate, ε, be quantified as the difference between the measured response and the synthesized:

$$\varepsilon = \sum_{all\ DOFs} RMS\left(\underline{y}(t) - \underline{\hat{y}}(t)\right) \tag{12}$$

In Figure 2, the error for each load scenario is shown. The curve for the rotational DOFs is included merely for academic interest as the most likely physical input will be a force rather than a moment. In this case, a clear minimum is observed at a force acting at node 28. From Figure 1 it can be seen that node 28 in the expanded model coincides with the position of the load. By selecting the load distribution, $\underline{f}_0$, causing the minimum error and multiplying by the scaling function, $g(t)$, associated with this distribution, it is then possible to get an estimate of the load, $\underline{f}(t)$. The result is shown in Figure 3. In the time domain, small fluctuations around the true value is seen. These are caused by the added noise in the response signal. In the frequency domain, this yields a noise floor under which the load cannot be reconstructed.

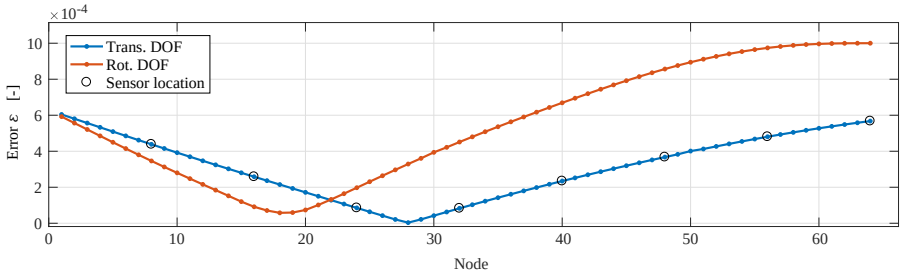

Figure 2: Calculated error. Each datapoint corresponds to a load scenario in $\underline{\underline{F}}_0$. Every second is loading to a translational DOF and rotational DOF, respectively, hence the separation of curves.

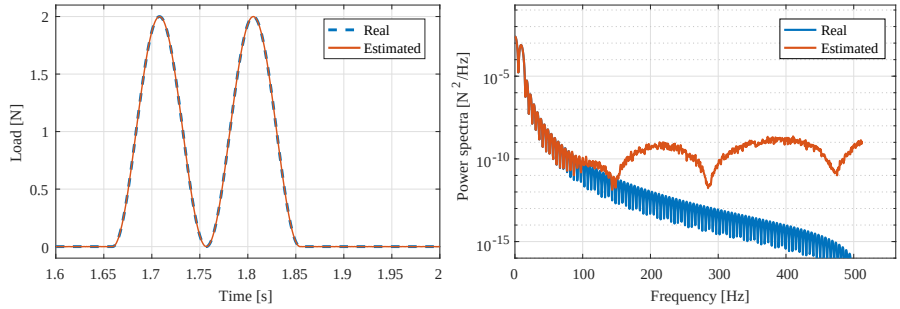

Figure 3: Time- and frequency domain estimate. Five modes were included to establish the frequency response function. The power spectra are computed using Welch averaging with a block size of 2^{11} corresponding to 2s.

4. Experimental case

An experimental case study has been performed at the facility at Aarhus University. A cantilever T-structure made from RHS $40 \times 40 \times 2$ is used for the experiment. The T measures 1.5 m in height and is 1 m wide. The T is clamped to the floor through the base plate seen in Figure 4. Ten uni-axial accelerometers are distributed as shown in Figure 4. Accelerometers used are Brüel & Kjær type 4508-B 100mV/g.

First, a test with random excitation from compressed air is recorded from which modal parameters are extracted. The identification technique used for this task is the frequency domain decomposition, FDD, [13]. The response is recorded for 300 seconds at a sampling frequency of 1652 Hz. The recordings from the test are represented in terms of singular values from the spectral density matrix, see Figure 5. Note the harmonic peaks at 50 Hz and 100 Hz caused by the power grid. The damping ratio for the first mode is estimated to 0.25% and is assumed to be applicable for all modes. Ten modes were identified in the frequency band of 0-350 Hz and their frequencies are listed in Table 2.

Secondly, an impact hammer is used to generate and record loading of the structure. A Brüel & Kjær impact hammer type 8206 22.5mV/N is used for the experiment. The hammer is equipped with a soft tip and an impact is made between sensor S03 and S07 in the y direction. The exact position is 12 cm below the sensor S03, i.e. 1/4 of the distance between the two sensors, see Figure 4.

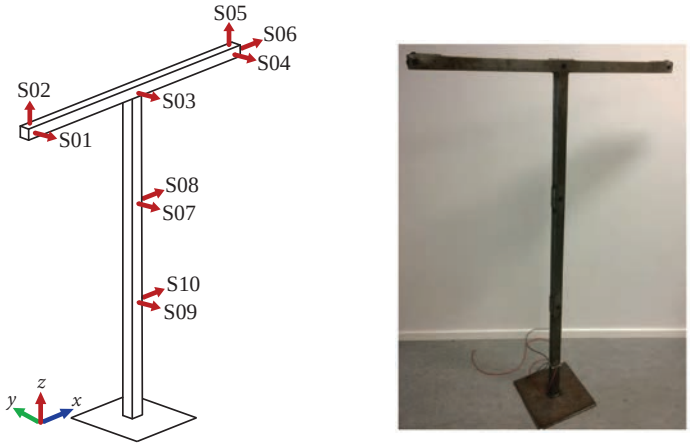

Figure 4: Left: Schematic sensor layout. Right: Photo of test subject.

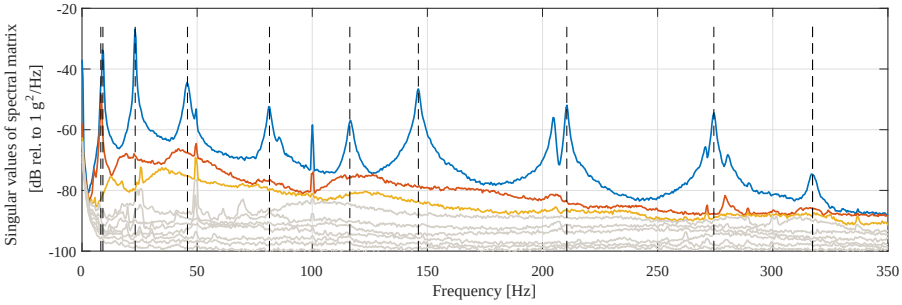

Figure 5: Singular value decomposition of the response from random loading. The spectral matrix is computed using Welch averaging with a block size of 2^{12} which corresponds to 2.5s.

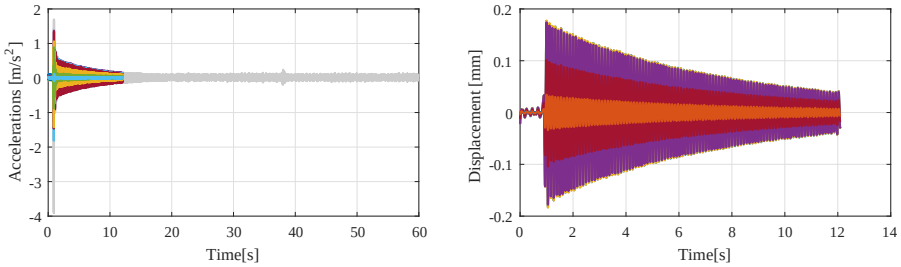

Figure 6: Impact response shown for all channels.

Figure 6 shows the raw acceleration response recorded during the impact. The accelerations are integrated twice in the frequency domain to obtain the displacements. During integration, a highpass filter of 5 Hz is used. In order to improve computational efficiency, only 12/60 s are included in the analysis. In addition, the signal is decimated with a factor four pushing the Nyquist frequency down to 207 Hz [14].

An FE model is made and updated to increase the correlation of frequencies and mode shapes. The model is made from Bernoulli beam elements with six degrees of freedom at each node and distributed mass. Meshing of the structure is done so that the sensor locations match an FE node. The number of FE nodes is chosen with respect to convergence of the modes of interest and the desired spatial resolution for the successive load identification. The mesh density may be seen in Figure 9. The model is then updated in two subsequent steps. 1) Material density is increased until the total weight of the FE model corresponds to the physical model. 2) The rotational stiffnesses at the base of the T, Rx, Ry, Rz, are updated until a best fit for the first 10 modes is achieved. The MAC matrix (after updating) can be seen in Figure 7. The MAC matrix is computed using DOF pairs between the FE model and the experimental DOFs.

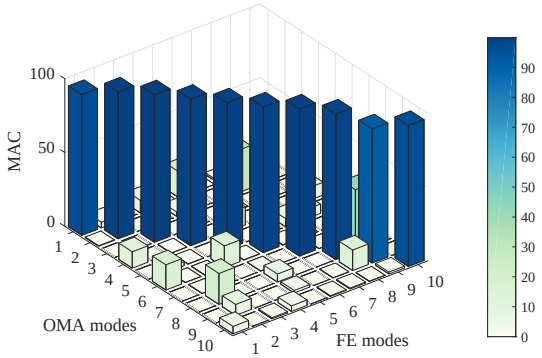

Figure 7: Modal Assurance after updating.

Table 2: Natural frequencies.

Mode	1	2	3	4	5	6	7	8	9	10
Frequency OMA [Hz]	8.17	9.08	23.1	44.8	81.4	116	146	211	274	317
Frequency FE [Hz]	8.34	8.83	24.6	45.3	81.1	116	147	207	277	315

Once the FE model is updated to an acceptable level, the frequency response function can yet again be formed using equation (10). The mass normalized mode shapes from the updated FE model are used along with the eigenfrequencies identified from the OMA. All ten mode shapes are included in the process.

When defining the set of possible load distributions, $\underline{\underline{F_0}}$, again the identity matrix is used as a basis. However, this time, omitting the rotational DOFs. Since the expanded model contains 41 nodes, (including the fixed node at the base), this yields in total 120 different load scenarios to be evaluated. The error associated with each load scenario is shown in Figure 8. The results have been broken into three groups depending on their direction. As seen in Figure 8, impact in the y-direction yields substantially less error than for the other directions. The minimum is more indistinct compared to the simulated case study in Figure 2. However a minimum is observed at the location of impact - node 23. Since the load distributions used in this case consist of localized forces acting at one node at a time, the errors associated with each distribution can be assimilated with a spatial position and provide a visual feedback on where an impact was most likely to have happened. This is shown in Figure 9.

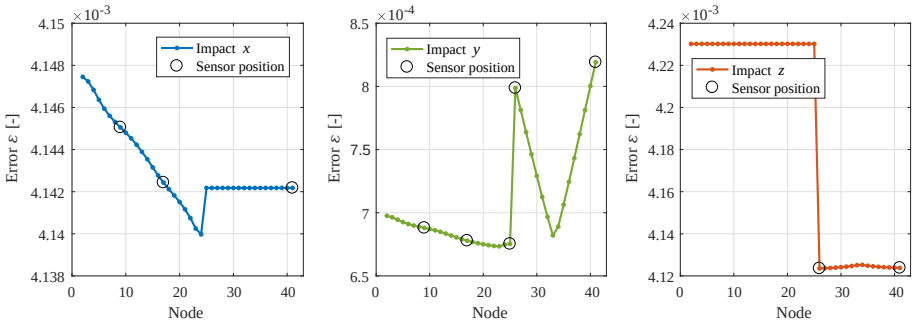

Figure 8: Calculated error. Node 1 is located at the base of the T and node 25 is located at the joint.

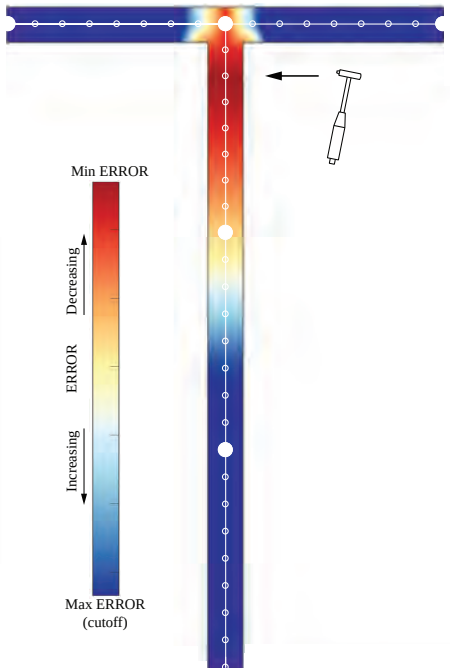

Figure 9: Re-representation of the calculated error from Figure 8 - y-direction impact. The figure indicates at which position the impact was most likely to occur with linear interpolation between nodes. The bold dots indicate sensor position whereas the open dots represent the FE nodes.

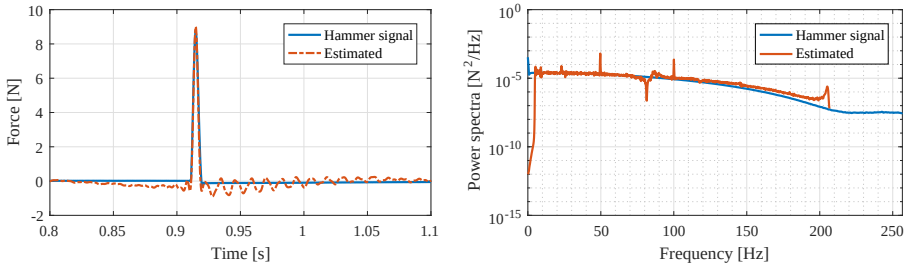

Figure 10: Identified load. The power spectra are computed using Welch averaging with a block size of 2^{11}.

The load distribution causing the minimum error can be multiplied by its scaling function and an estimate for the temporal variation can be obtained as it was done in the simulation case study. The result of the load estimate is shown in Figure 10. In the time domain, the estimate follows the trend of the hammer with a peak deviation of three percent. It is observed that a negative load is estimated prior to the impact and some ringing afterwards. Looking at the response data in Figure 6, it is observed that the structure is not at complete rest at the time of impact. Since the load estimate is directly related to the response of the structure, any ambient vibration will skew the identification of hammer input. In the frequency domain, the estimate shows some discrepancy around the resonance frequencies. This may be due to the assumption that all modes bear the same damping ratio. Noise spikes are observed at 50 and 100 Hz; these are a remaining product of the harmonic noise in the response signal.

5. Conclusion

A method for indirect load identification has been presented. The method is titled "scenario based" as a keystone to success is having a set of good load distributions to select from. The method was demonstrated by a numerical simulation and a physical experiment. Some of the main observations are recaptured here:

By use of expanded mode shapes, the method shows potential in load identifications, even at locations where the response is not recorded immediately. In the two cases, the method proves not to yield any false-positive estimates for the position of the impact load although the estimated location of impact is more outspoken for the numerical study than for the physical experiment. The rank deficiency of the FRF matrix is mitigated by assuming a load distribution prior to making a least square fit. This makes the method insensitive to modal truncation, but it remains reliant on a well-updated FE model. The noise and harmonic disturbance to the recorded response signal is causing the load identification to deviate, but the algorithm remains stable.

Obviously, one of the shortcomings of this method is the need for engineering judgement in order to develop a set of reasonable load distributions. Since this method is scenario based, it is crucial that a fairly good distribution has been foreseen prior to the analysis, otherwise the estimate may be erroneous.

Another challenge to this method arises if the distribution changes with time. Segmenting the response may improve this limitation but further work is needed in this area.

It is fundamental that the response is recorded at the time of loading, i.e. the structure must be at rest at the beginning of a time series, otherwise this may alter the load estimates. This assumption seems to be violated to some extent in the physical experiment presented in this paper. From Figure 6 it seems like the T was vibrating from excitation not caused by the hammer.

6. Future work

In principle, there are no limitations to the load distribution and the method could be applied to other cases, where some prior knowledge on loading pattern exists. For instance, wave loading on an offshore structure.

Some limiting factors which have not been covered in great detail could be a basis for further work. For example, what is the sensitivity of the estimated modal parameters and how will a small change influence the load identification process or how this method will perform on highly damped systems.

Acknowledgments

The authors acknowledge the funding received from the Centre for Oil and Gas – DTU/Danish Hydrocarbon Research and Technology Centre (DHRTC).

References

[1] K. Stevens, Force identification problems - an overview, Proceedings of the SEM Spring Conference on Experimental Mechanics (1987) 838–844.
[2] R. Brincker, C. Ventura, Introduction to Operational Modal Analysis, John Wiley and Sons, Ltd, Chichester, West Sussex, UK, 2015.
[3] Y. Liu, W. Shepard, Dynamic force identification based on enhanced least squares and total least-squares scheme in the frequency domain, Journal of Sound and Vibration 282 (2005) 37–60.
[4] M. Aenlle, R. Brincker, P. Fernández, A. Fernández, Load estimation from modal parameters, Proceedings of the International Operational Modal Analysis Conference, iomac 1 (2007) 39–50.
[5] P. Léger, J. M. Ricles, L. J. Robayo, Reducing modal truncation error in the wave response analysis of offshore structures, Communications in applied numerical methods 6 (1990) 7 – 16.
[6] K. Maes, A. Iliopoulos, W. Weijtjens, C. Devriendt, G. Lombaert, Dynamic strain estimation for fatigue assessment of and offshore monopile wind turbine using filtering and modal expansion algorithms, Mechanical Systems and Signal Processing 76-77 (2016) 592–611.
[7] K. Maes, Q. Smyth, G. De Roeck, G. Lombaert, Joint input-state estimation in structural dynamics, Mechanical Systems and Signal Processing 70-71 (2016) 445–466.
[8] E. Parloo, P. Verboven, P. Guillaume, M. van Overmeire, Force identification by means of in-operation modal models, Journal of Sound and Vibration 262 (2003) 161–173.
[9] B. Wang, C. Chiu, Determination of unknown impact force acting on a simply supported beam, Mechanical Systems and Signal Processing 17 (3) (2003) 683–704.
[10] E. Lourens, E. Reynders, G. D. Roeck, G. Degrande, G. Lombaert, An argumented Kalman filter for force identification in structural dynamics, Mechanical Systems and Signal Processing 27 (2012) 446–460.
[11] J. O'Callahan, P. Avitabile, R. Riemer, System equivalent reduction expansion process, Proceedings of the International Modal Analysis Conference, IMAC (1989).
[12] R. Brincker, A. Skafte, M. Anelle, A. Sestieri, W. D'Ambrogio, A. Canteli, A local correspondence principle for mode shapes in structural dynamics, Mechanical Systems and Signal Processing Vol: 45 (2014) 91–104.
[13] R. Brincker, L. Zhang, P. Andersen, Modal identification from ambient responses using frequency domain decomposition, Proceedings of the International Modal Analysis Conference, IMAC (2000) 625–630.
[14] R. Lyons, Understanding Digital Signal Processing, Pearson Education, 2011.

Chapter 8

Model uncertainty

Paper II

"Evaluating the effect of modelling errors in load identification using classical identification methods"

Michael Vigsø, Rune Brincker and Christos Georgakis

Published in Journal of Shock and Vibration, 2019

This chapter presents the study on uncertainties when conducting load identification using the pseudo inverse method. We imagine that load identification follows modal identification such as OMA, and we then introduce errors into the identified modal parameters and show how they influence the load identification. The study is based on a simulated case. The author has performed the main part of the ideation, experiments, analysis and the writing of the paper. The paper has been formatted with minor grammatical adjustments to suit this thesis.

Evaluating the effect of modelling errors in load identification using classical identification methods

Michael Vigsø[a,*], Rune Brincker[b], Christos Georgakis[a]

[a] *Aarhus University, Inge Lehmanns Gade 10, 8000 Aarhus, Denmark*
[b] *Technical University of Denmark, Brovej 118, 2800 Kgs. Lyngby, Denmark*

Abstract

Load identification, or input identification as the more general term, is a field of study that requires a wide set of disciplines, which suffers from uncertainties caused by the challenges within each discipline. When making load identification, several different approaches exist. For all (or at least most) methods, however, some sort of system model is required. This model may be simple or complex depending on the system at hand. Typically, if the identification process is vibration fed, the system model will be created from modal parameters. These parameters, however, are often subject to uncertainty and thus may be considered as stochastic variables. In this paper, the root causes of uncertainty for load identification are demonstrated using classical identification techniques. From a numerical perspective, uncertainty is quantified through Monte Carlo simulations. Two results are outlined: one where the identification process is completely blindfolded in its most naive form, and one where the spatial distribution of the load is predefined. In general, it is found that fixing the spatial distribution of the load can compensate for truncation errors in the modal parameters.

Keywords: Load identification, Uncertainty modelling, Modal truncation, Load spatial distribution

1. Introduction

Modal analysis is a convenient and efficient method for retrieving the dynamic properties of a civil engineering structure in a condensed form. Traditionally, two methods exist for modal analysis - experimental modal analysis (EMA) and operational modal analysis (OMA). The return from a modal analysis consists of the following modal parameters: mode shapes, natural frequencies and modal damping [1]. Modal analysis is a commonly used approach, yet the confidence in the extracted modal parameters will depend on the quality of excitation and response measurement. Although new methods are continuously surfacing to overcome some of the challenges, a remaining uncertainty on the estimates persists. In the application for civil engineering structures, another range of challenges may arise, for instance, when the stationary assumption is violated through variations in environmental conditions such as temperature or mass loading.

*Corresponding author
Email addresses: mvigso@eng.au.dk (Michael Vigsø), runeb@byg.dtu.dk (Rune Brincker), cg@eng.au.dk (Christos Georgakis)

Published in Journal of Shock and Vibration, Article ID 9490760
This paper has been formatted to suit this thesis *October 2019*

The exertion of indirect load identification may be a successive step to the modal analysis. If the retrieved modal parameters accurately and in whole can describe the dynamics of the system, they can be used in the inverse calculation needed when doing indirect load measurements. The principle is that if a dynamic model is available (from EMA or OMA) and the response of the system is measured, then an estimate of the load can be obtained through deconvolution. Load identification has been in focus in the recent decade, and many attempts have been made in order to obtain a stable and accurate method. In recent years, identification techniques in real-time using Kalman filters have proven successful in certain cases [2–7]. Besides the recursive model description, another benefit from these methods is the capability to merge different sensor type information. For these filters to perform well, however, several noise models must be determined, which may be difficult. Aucejo et al. [8] thoroughly examined how the different fitting parameters may influence the performance of identification though they omitted model errors from their analysis. Using identification techniques in the time domain, Wang et al. [9–11] studied the interval envelope on the load estimation given uncertainty in the response measurements and integration errors.

Another approach is to deconvolute the response in the frequency domain. [12–15]. This was the main approach from the early days in the automotive and aviation industry [16, 17]. The method is based on establishing the relation between the system response and force at different frequencies. The technique requires a recording time, which is why the method does not perform well in real-time applications. Comparative studies between the two approaches are also seen in e.g. [18]. The response measurements are often recorded in terms of displacements, velocities, accelerations, or strains. These can be obtained through attached sensors (invasive) or from noninvasive techniques such as lasers, digital image correlation, or even by acoustics [19, 20].

For every method referred to above, a system model is needed. This model may be derived from a finite element (FE) model or from modal parameters directly obtained from the EMA or OMA. Now, an obvious question arises: how accurate must the modal parameters be in order for the load identification to be satisfying? Although some authors already have addressed some of these questions [21–24], this paper will revisit some of the fundamental challenges from a visual point of view. By studying a practical example, the sensitivity of estimation errors will be demonstrated through a Monte Carlo simulation. In order not to disappoint the reader, we note that this paper deals merely with the consequence and not mitigation of the estimation errors in modal parameters.

2. Simulation setup

A plane cantilever beam will host the basis for this study. The beam is made from Euler-Bernoulli beam elements with two degrees of freedom (DOFs) at each node - a translational and a rotational as indicated in Figure 1. We assume that the beam is proportionally damped through the Rayleigh coefficients α and β. The mass is assumed to be distributed along the elements. The beam is discretized by three elements and fixed at the bottom node which yields, in total, six free DOFs and hence six modes of vibration. We note that the FE model has not yet fully converged for all modes at this nodal resolution; however, this is not of importance for the given study.

The beam model is then subjected to a loading history from which the dynamic response is simulated at a sampling frequency of 1 kHz. The loading time history is selected so that both dynamic response and quasi-static response will be visible within the output. The load is composed of a square impulse followed by a low-frequency wave, again followed by a superimposed high-frequency wave train (15 Hz). Figure 1 shows the system in focus for this current study. The four-noded cantilever beam constitutes the system model. The loading history (input) is shown in

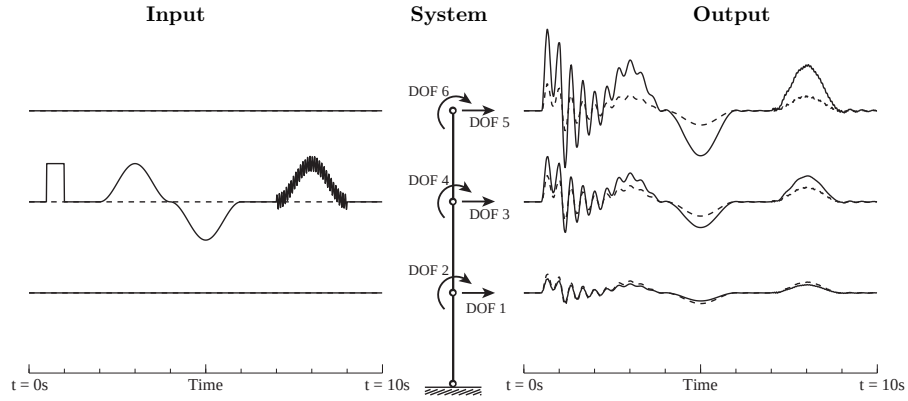

Figure 1: Simulated system. Left shows the input: 10 s load history applied at each node. Right shows the corresponding response. Dashed lines are the moment and corresponding nodal rotation. Solid lines are the force and the corresponding nodal displacement.

the left-hand side of the figure. Each line corresponds to a load time series for the corresponding node, i.e., a flat line resembles zero loading. The solid lines are the horizontal force, whereas the dashed lines are the moment. The loading is set to act at one node only - the second node from the top. The right-hand side shows the corresponding response (output) for each node. Solid lines are the horizontal displacements, and the dashed lines show the rotation of the nodes. Amplitude scaling is irrelevant as the system is linear.

The process of load identification will hence be the reverse order of the process shown in Figure 1. First, the response of the structure is measured. Then, if the dynamic properties of the system are known, we can make an inverse calculation and thus estimate the load causing the measured response. Before proceeding to the load identification, a small amount of noise is added to the system response and hereafter considered as the measured signal (100 dB Gaussian white noise is added).

3. Load identification process

In order to assess the sensitivity of the load estimate given the variations in the estimated modal parameters, a method must be chosen. For this paper, two methods will be outlined - both operating in the frequency domain. We have selected two methods that easily can be applied using the results from an EMA or OMA[1]. The methods originate from the automotive and aviator industry [22, 23] and are often referred to as the 'transfer path analysis matrix inversion' or just 'pseudo inverse technique'.

[1]Typically, if modal parameters are obtained from an OMA, problems persist as the modal mass and hence the mode shape scaling is unknown. For now, we will ignore this challenge and assume that the mode shapes obtained are correctly scaled.

3.1. Method 1

The first method, referred to as Method 1, is the most simple and straightforward. This method might be a tempting first approach, but it shall be demonstrated later on why it could lead to unfortunate results. Consider the response of a linear, time-invariant system which, in the frequency domain, is given as follows:

$$\underline{Y}(\omega) = \underline{\underline{H}}(\omega)\underline{F}(\omega) \tag{1}$$

where, $\underline{Y}(\omega)$ is the system response, $\underline{\underline{H}}(\omega)$ is the frequency response function (FRF), and $\underline{F}(\omega)$ is the load, all given at the discrete frequency ω. This process resembles very well what has been illustrated in Figure 1. The FRF matrix can be computed as a sum of N modal contributions as follows:

$$\underline{\underline{H}}(\omega) = \sum_{r=1}^{N} \left(\frac{Q_r \, \underline{\phi_r} \, \underline{\phi_r}^T}{i\omega - \lambda_r} + \frac{Q_r^* \, \underline{\phi_r}^* \, \underline{\phi_r}^H}{i\omega - \lambda_r^*} \right) \tag{2}$$

where, $\underline{\phi_r}$ is the mode shape vector, Q_r is the mode scaling function, and λ_r is the complex pole, all for mode r. Superscript ^{T} is the transpose, * is the complex conjugate and ^{H} is the Hermitian transpose. See [25] for the derivation of this formula.

Now, we presume that the output $\underline{Y}(\omega)$ is available through measurements - both the translation and the rotation of all DOFs. All that is left to do is to calculate the inverse of the FRF and premultiply on both sides in order to obtain an estimate on the load $\underline{\hat{F}}(\omega)$.

$$\underline{\hat{F}}(\omega) = \underline{\underline{H}}^{\dagger}(\omega)\underline{Y}(\omega) \tag{3}$$

Since errors or modal truncation can cause the inversion of the FRF to become singular, the inversion is performed using the Moore-Penrose pseudo inverse. [26] Method 1 has been used in [15, 27, 28] with the minor change that the inversion of the FRF matrix is performed through a singular value decomposition technique. Regularization techniques have also shown to reduce the sensitivity in the matrix inversion [29].

3.2. Method 2

Another method, Method 2, will be added for comparison. This method resembles Method 1 to a high degree with only one minor, yet important, difference. In Method 1, there were no restrictions to the solution and the load estimate $\underline{\hat{F}}(\omega)$ could be distributed to any DOF in the system. If the spatial distribution of the load is known (and unchanging), this can be incorporated into the identification process through a separation of variables as follows:

$$\underline{F}(\omega) = \underline{f_0} \, g(\omega) \tag{4}$$

where $\underline{f_0}$ constitutes the spatial distribution of the load and $g(\omega)$ is its scaling function. If the given loading scenario allows this separation and if $\underline{f_0}$ is known, Eq (1) and Eq. (3) can be rewritten as

$$\underline{Y}(\omega) = \underline{\underline{H}}(\omega) \, \underline{F}(\omega) \tag{5}$$

$$= \underline{\underline{H}}(\omega) \, \underline{f_0} \, g(\omega) \tag{6}$$

$$= \underline{c}(\omega) \, g(\omega) \tag{7}$$

Which then can be solved for the scaling constant $g(\omega)$:

$$\hat{g}(\omega) = \underline{c}^{\dagger}(\omega)\, \underline{Y}(\omega) \tag{8}$$

and the final load estimate then reads

$$\underline{\hat{F}}(\omega) = \hat{g}(\omega)\, \underline{f_0} \tag{9}$$

Methods to derive the distribution $\underline{f_0}$ in a similar system have been shown in [13, 30–32], but for this study let us assume that the distribution is a known quantity; hence, $\underline{f_0} = [0\ 0\ 1\ 0\ 0\ 0]^T$.

The equations, Eq. (1 - 9), describing Method 1 and Method 2 directly yield a frequency-domain estimate of the load. All the following figures in this paper will show the load estimate as a time history in line with the input (left-hand side) in Figure 1. The equivalent time-domain representation is obtained by means of the inverse Fourier transformation.

3.3. Condition of the frequency response function

The condition number may be a measure of how sensitive the matrix is to inversion, where a large condition number indicates an ill-conditioned matrix and vice versa [33]. Singular value decomposition may separate the FRF matrix into singular vectors and singular values. Letting the condition number be defined as the ratio between the largest and smallest singular value, we thus obtain a quantitative measure on the sensitivity. Since the FRF matrix, $\underline{\underline{H}}(\omega)$ is defined for a range of frequencies, each frequency will be inherent to a condition number. The condition number(s) for the full rank FRF matrix is shown in Figure 2 as a function of frequency. Here, it is seen how the condition number increases at the resonance frequencies.

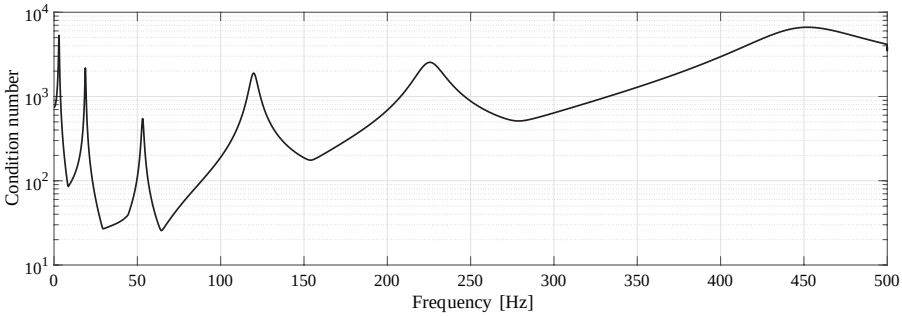

Figure 2: Condition number for the full rank frequency response function at different frequencies.

There is no sharp limit to assess whether a condition number will yield a stable inversion, but a condition number larger than 100 should call for immediate concern which is the case for most frequencies in our case [33]. Since the FRF matrix is constructed from a set of modal contributions, the rank of the FRF matrix will depend on the number of independent modes. If modal truncation is present, this causes the FRF matrix to be rank deficient, which means that the smallest singular value becomes close to zero and consequently yields a condition number going to infinity.

$$\text{cond}\left(\underline{\underline{H}}(\omega)\right) \to \infty \mid \text{rk}\left(\underline{\underline{H}}(\omega)\right) < \min(m, n) \tag{10}$$

where, m and n are the number of rows and columns in $\underline{\underline{H}}(\omega)$ while cond$(\cdot)$ and rk$(\cdot)$ indicates the condition number and rank respectively.

If the FRF matrix is constrained by a spatial distribution vector $\underline{f_0}$ as it is done in Method 2, the product reduces to the vector $\underline{c}(\omega)$. Singular values of an $m \times 1$ nonnull vector is a single non-zero element arranged in an $m \times 1$ vector [34]. This consequently provides a condition number of unity, which means that the "inversion" will be stable for all frequencies.

$$\text{cond}\left(\underline{\underline{H}}(\omega)\,\underline{f_0}\right) \equiv 1 \tag{11}$$

4. Modal truncation

The number of DOFs in a real structure will, of course, be approaching infinity, but the modes which can be identified are depending on the sensor distribution and capability. Consequently, truncation of the modal space will always be present in real-life situations, which is why this section is included [35, 36].

From Eq. (2), it is seen that the response of a system is a linear contribution from all modes in the system. If modes are omitted from this sum, this will truncate the response function. Figure 3 and Figure 4 show how this modal truncation affects the estimate on the load estimate from the inverse calculations. One additional mode is removed for every case. All modal parameters are treated as deterministic and at their true values, i.e., the only error in the FRF is the higher modes being omitted.

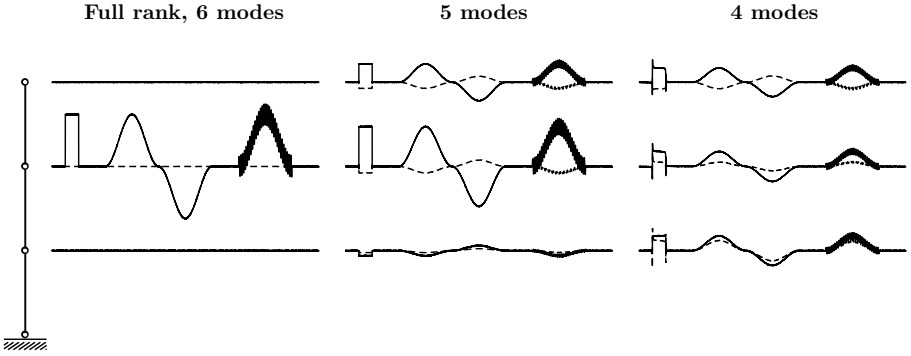

Figure 3: Load estimate using Method 1. The figure shows the time domain load estimate based on the number of modes included in the FRF matrix. Each time series shown has a 10 sec. duration. Solid lines show the force [N] and the dashed lines show the moment [Nm].

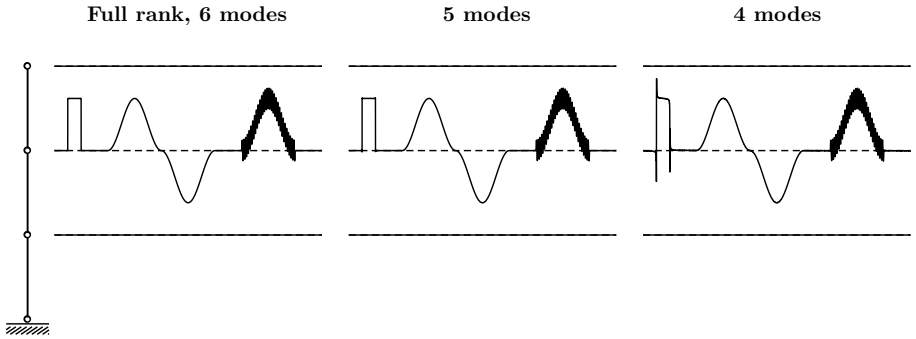

Figure 4: Load estimate using Method 2. The figure shows the time domain load estimate based on the number of modes included in the FRF matrix. Each time series shown has a 10 sec. duration. Solid lines show the force [N] and the dashed lines show the moment [Nm].

As seen in Figure 3, the load estimate is acceptable when all six modes are used despite the small content of noise on the response measurements. However, when omitting modes from the FRF matrix, the load estimate from Method 1 quickly becomes erroneous, both in terms of distribution and magnitude. Even though the resonance frequency of the modes omitted may be far from the frequency of the load, this truncation still makes a great impact. Meanwhile, in Figure 4, it is seen that Method 2 retrieves more consistent estimates on the load. Any DOF, besides DOF 3, obtains a zero-load estimate following the definition of the spatial distribution given in Eq. (9). For both methods, it is seen that the estimate for the square impulse overshoots at the discontinuities caused by the Gibbs phenomena for the truncated modal space [37].

If we consider the resynthesized response $\underline{\hat{Y}}(\omega)$ from the load estimates $\underline{\hat{F}}(\omega)$ from either Method 1 or Method 2 and the truncated response function $\underline{\underline{\hat{H}}}(\omega)$, we observe

$$\underline{\hat{Y}}(\omega) = \underline{\underline{\hat{H}}}(\omega)\underline{\hat{F}}(\omega) \tag{12}$$

$$\epsilon\left(\underline{Y}(\omega), \underline{\hat{Y}_1}(\omega)\right) < \epsilon\left(\underline{Y}(\omega), \underline{\hat{Y}_2}(\omega)\right) \tag{13}$$

Here, ϵ is an arbitrary error function between the measured response $\underline{Y}(\omega)$ and the re-synthesized response $\underline{\hat{Y}}(\omega)$. The solution from Method 1 will yield a better response approximation than Method 2. This means that Method 1 is a more mathematically accurate solution. Yet, when comparing Figure 3 and Figure 4 it is clear that in a physical sense Method 2 is more consistent. This is one of the major challenges when making load identification solely based on the response using a least-square approach. Consequently, the load estimate may return as an equivalent loading rather than the actual, as seen in Figure 3.

For the given simulation, the load is conveniently acting at a point where the response is being "measured". In other cases one might not be this lucky and expansion is needed in order to estimate the response at locations that were not recorded originally. Several expansion techniques (/virtual sensing techniques) exist for this [38, 39], but effectively, similar truncation errors will be introduced as no new modes are added during the expansion.

5. Stochastic modelling

The modal parameters needed to establish the response function may be obtained through an experimental identification process - either EMA or OMA. The parameters obtained in this process will always be subject to variations. The variations can originate from physical causes such as influence from temperature, operational mass loading, or other nonanticipated nonlinearities violated by the model description. Also, nonphysical uncertainties related to data postprocessing and pole extraction are known to exist [40–43]. These magnify if the excitation of the structure is unfortunate or if the sensor resolution and location is poorly chosen. Noise and other limitations on the sensor may also be a cause of uncertainty.

The variations in the modal parameters can be implemented from many different uncertainty models. The most common is probabilistic, where a probability density function is used to describe the statistical variations. Other formulations such as the fuzzy-set model or a nonprobabilistic interval method could also have been utilized. For this study, however, we will rely on the probabilistic approach and assume that all these aforementioned causes of uncertainty effectively can be modelled as an uncorrelated stochastic variation in each of the estimated modal parameters. The uncertainty in natural frequencies is assumed to follow a normal distribution given a coefficient of variation; hence, estimates for the lower frequencies are the most certain. The coefficient of variance is chosen as $cv = 2\,\%$ for all frequency estimates. The stochastic model for the natural frequency of mode r hence reads

$$\Omega_r \sim \mathcal{N}(\mu, \sigma) \tag{14}$$

where, the expectation μ is assumed to be in line with the true natural frequency for mode r, i.e., $\mu = \omega_r$. The standard deviation is derived from the coefficient of variation as $\sigma = cv\ \omega_r$.

Damping estimates are known to be the most uncertain parameters to quantify. Since the damping typically involves fairly low values - say a few percents - and the estimates are subjected to a vast amount of uncertainty, it must have some skewness in order to avoid negative estimates. The study [44] also noted a positive skewness in damping estimates, yet the distribution fit was not studied. For this simulation, we assume that the distribution can be modelled as a standard gamma distribution with a shape parameter α. The stochastic damping parameter model for mode r hence reads

$$Z_r \sim \Gamma(\alpha) \tag{15}$$

were the shape parameter is assumed to be equal to the true damping ratio for mode r (in percent). That is, $\alpha = \zeta_r$ which yields a mean $\mathrm{E}[Z_r] \approx \zeta_r$.

We assume that mode shapes always will be real following the proportionally damped system. The variations in mode shapes are implemented as a stochastic process described by a spatially uncorrelated variation in individual DOFs and a variation in scaling of the mode shape. For mode r this means

$$\underline{\Phi_r} = \underline{\underline{\Sigma}}\ \underline{\phi_r}\ \kappa \tag{16}$$

were, $\underline{\phi_r}$ is the true mode shape for mode r, $\underline{\underline{\Sigma}}$ is a diagonal matrix whose entries contain the uncorrelated noise on individual DOFs, and κ is the scaling of the mode shape. Both noise models are assumed to be normally distributed with a mean μ and standard deviation σ as

$$\underline{\underline{\Sigma}}_{ii} \sim \mathcal{N}\left(1,\ 5 \times 10^{-3}\right) \tag{17}$$

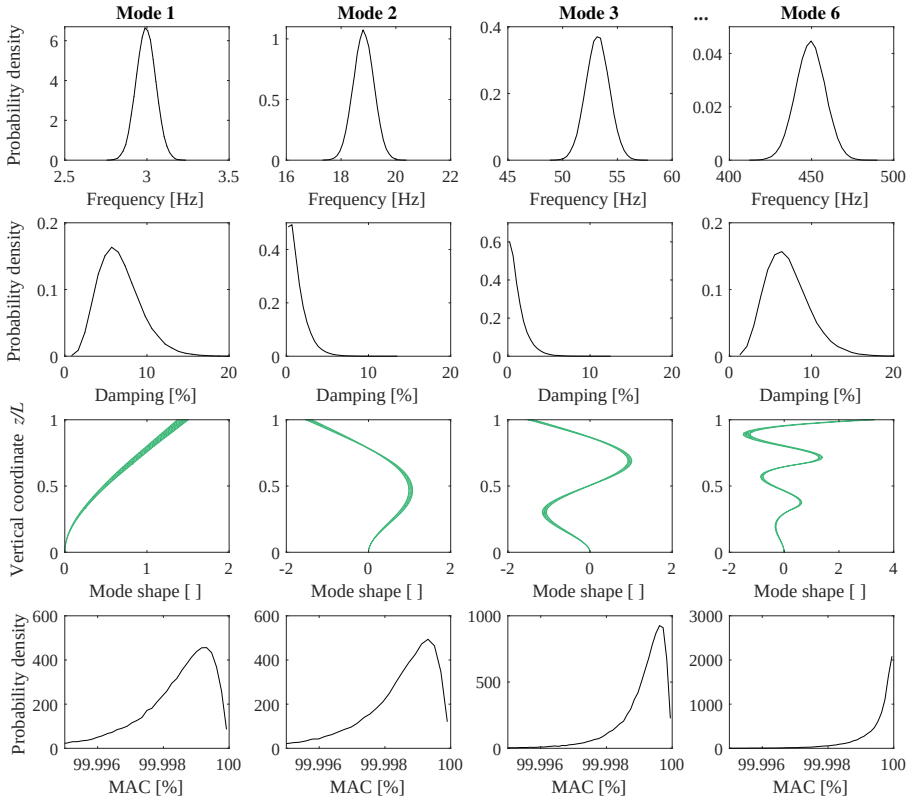

Figure 5: Realization of the different modal parameters from 100 000 Monte Carlo simulations. The mode shape uncertainty band is shown for the 98% quantile using cubic interpolation.

$$\kappa \sim \mathcal{N}\left(1,\ 1 \times 10^{-2}\right) \tag{18}$$

The mode shapes are assumed to be mass normalized. Thus, the alteration in mode shapes will affect the modal mass as well. The spatially uncorrelated alterations may violate the mode shape orthogonality, but only to a small degree as the error standard deviation for the mode shapes' DOFs is set at 0.5 %. The consequences of omitting modes have already been shown; hence, only small variations are now included.

Using the principles of Monte Carlo simulation, a realization of the stochastic modelling is shown in Figure 5 for the first three and the last mode. The uncertainty band for the mode shapes is shown using cubic interpolation in order to show the rotational DOFs. The modal assurance

criterion (MAC) [45] between the true mode shape and the stochastically altered is shown for each mode. We note that the variations in MAC values are small compared to what may be experienced from experimental work.

6. Results

Before turning to the identification process, let us have a look at the FRF matrix. The stochastic variables shown in Figure 5 are fed into Eq. (2) through a Monte Carlo simulation, and a sample of the FRF matrix is shown in Figure 6. For the 100 000 Monte Carlo simulations, the upper and lower 98% quantiles are indicated in the figure as the hatched green area. The black solid line is the mean value. The consequences of missing modes in the FRF matrix were studied by Maes et al. [46] and shall not be repeated here.

In order to evaluate the sensitivity in load estimates, the frequency response function is now considered as a stochastic process given the natural variation in modal parameters. Keep in mind that the "measured" system response is kept the same for all simulations and at its true value with a minimum of noise added. In the following three sections, the parameter variations are introduced a little at a time so that it will be more clear what happens to the estimates. Since the mean value of the modal parameters is in line with the true values, the averaged value of the estimates converges towards the true value as well. All six modes will be used in the making of the FRF matrix.

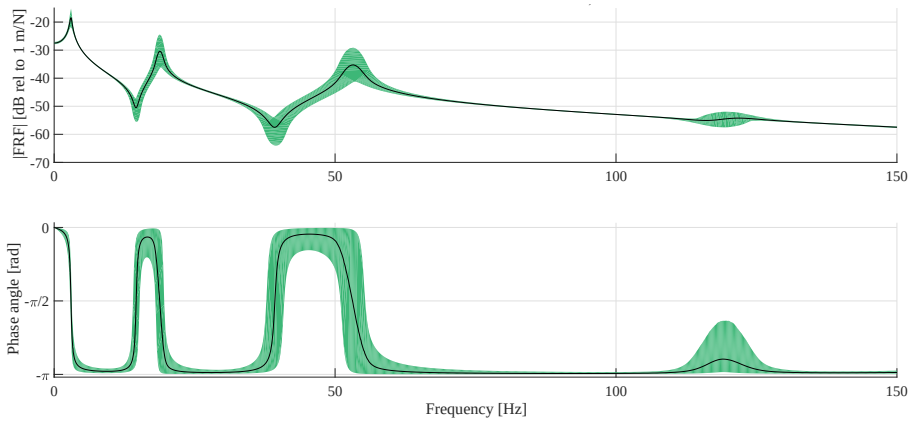

Figure 6: Sample frequency response function (dynamic flexibility) for DOF 3 given an input in DOF 3. Figure shows the upper and lower 98 % uncertainty band, given the modal parameters presented in Figure 5. Solid black line indicates the mean value.

6.1. Natural frequencies

First, only the natural frequencies are treated as stochastic variables, and the remaining modal parameters are kept as deterministic and exact. For the 100 000 Monte Carlo simulations, the FRF is synthesized, and a load estimate for each simulation is obtained through both methods. Figure 7

shows the upper and lower 98 % quantiles for the time-domain load estimates. It is seen that both methods yield a reasonably stable result despite variation in natural frequencies. Three points in time (a, b, and c) are extracted to highlight the error distribution on the estimate. The relative error for the two methods is given by the error standard deviation and summarized in Table 1.

6.2. Natural frequencies and damping ratios

Next, in addition to variations in natural frequency, the damping ratios are also treated as stochastic variables. That means only the mode shapes are left deterministic. The variation in the estimated load is shown for the two methods in Figure 8. As expected, the uncertainty bound for the estimates increases as the damping ratios are also treated as stochastic parameters. Method 1 seems to outperform Method 2, given this level of uncertainty in the modal parameters and noise in the output signal. A ringing effect in the estimate is observed at the discontinuities near the square impulse. In Method 1, however, it is seen how the load estimates are spreading to different nodes to compensate for the errors in the FRF matrix.

6.3. Natural frequencies, damping ratio and mode shapes

Finally, all modal parameters are now considered as stochastic processes, and the consequent result for the estimated load is given in Figure 9. Although the mode shapes are altered by values down to one or two percent for each node, the uncertainty in the load estimates for Method 1 shows an exponential growth. When mode shape errors occur, Method 1 fails to predict the load distribution and consequently the scaling of the load. For reference, the sample FRF shown in Figure 6 host the basis for the load estimate given in Figure 9. Note that in Figure 9 the error probability density is unequally scaled for Method 1 and Method 2.

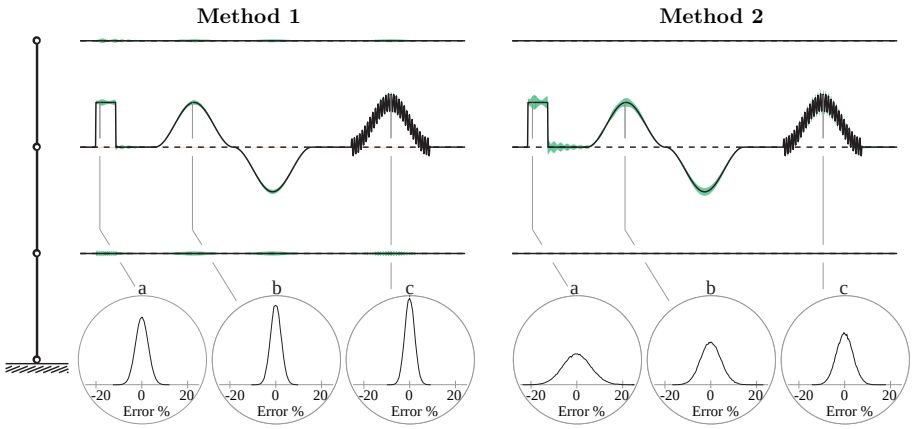

Figure 7: Natural frequencies are introduced as stochastic variables. The figure consequently shows the time history of the identified load using Method 1 and Method 2. Each time series shown has a 10 sec. duration. The solid lines are the mean values of the estimated force [N] and the dashed lines are the mean values of the estimated moment [Nm]. The hatched green area indicates uncertainty on the force while the hatched orange area is the uncertainty of the moment. Both are shown using the upper and lower 98 % quantiles. Three selected points in time show the error probability density (in percent) for the estimated load in DOF 3.

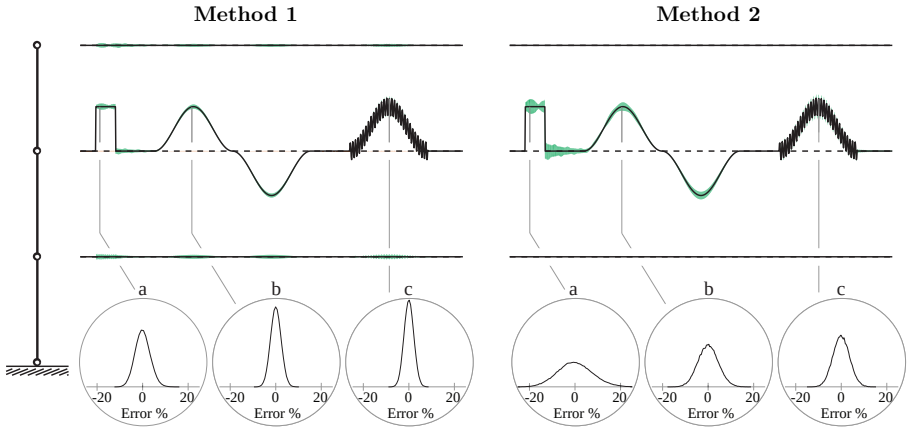

Figure 8: Natural frequencies and damping ratios are introduced as stochastic variables. The figure consequently shows the time history of the identified load using Method 1 and Method 2. Each time series shown has a 10 sec. duration. The solid lines are the mean values of the estimated force [N] and the dashed lines are the mean values of the estimated moment [Nm]. The hatched green area indicates uncertainty on the force while the hatched orange area is the uncertainty of the moment. Both are shown using the upper and lower 98% quantiles. Three selected points in time show the error probability density (in percent) for the estimated load in DOF 3.

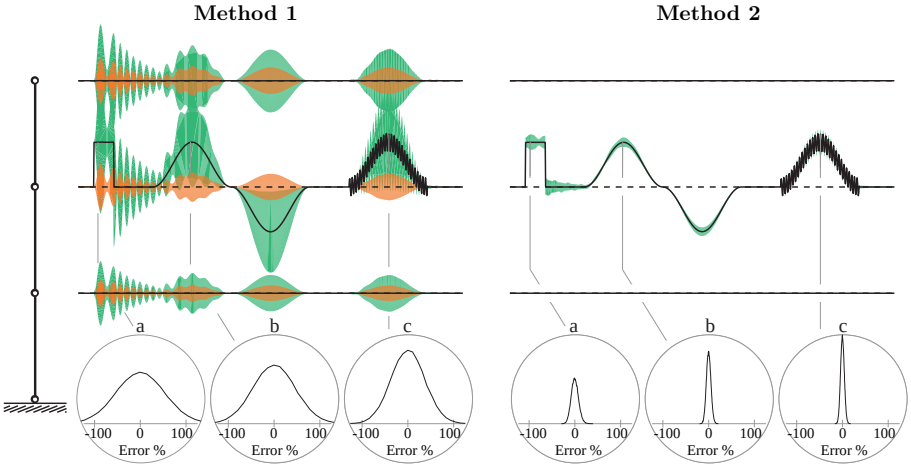

Figure 9: Natural frequencies, damping ratios and mode shapes are introduced as stochastic variables. The figure consequently shows the time history of the identified load using Method 1 and Method 2. Each time series shown has a 10 sec. duration. The solid lines are the mean value of the estimated force [N] and the dashed line is the mean value of the estimated moment [Nm]. The hatched green area indicates uncertainty on the force while the hatched orange area is the uncertainty of the moment. Both are shown using the upper and lower 98% quantiles. Three selected points in time show the error probability density (in percent) for the estimated load in DOF 3. Note that the probability density is scaled differently between Method 1 and Method 2.

Each of the load estimates shown by Figures 7 to 9 has three highlighted points in time, where an error probability density is shown. The corresponding standard deviation (std) is given in Table 1. We note that Method 1 seems to perform better than Method 2 as long as the mode shapes are intact. However, when introducing minor changes to the mode shapes, Method 1 cannot fully predict to which node the load is applied, which results in a poor estimate on DOF 3.

Table 1: Error standard deviation for different levels of uncertainty and for three selected points in time. All based on the force estimate in DOF 3.

Uncertainties introduced	Method 1			Method 2		
	Error std [%]			Error std [%]		
	a	b	c	a	b	c
Natural frequencies	2.73	2.29	2.13	6.08	4.39	3.64
Natural frequencies and damping ratios	3.28	2.31	2.12	7.67	4.45	3.64
Natural frequencies, damping ratio and mode shapes	53.1	46.3	36.9	7.96	4.94	4.10

7. Discussion

We have studied the performance of the two methods given the natural variation in the modal parameters used for the model description. The load estimates when using Method 1, shown in Figure 3 and Figure 9, are not as diverse as they might appear at first glance. If the resulting force is considered instead of every single entry in the estimated load vector, this leads to a more appealing result. First, reexamining the estimates shown in Figure 9 and by summarizing the contributions from each DOF, an equivalent baseline load is obtained. This resulting load estimate is compared with the true baseline load and shown in Figure 10. Now, it is seen how the uncertainty band is narrowed down. For this static system, an equivalent global loading can be estimated using Method 1 despite the stochastic variations in modal parameters as long as all modes are represented.

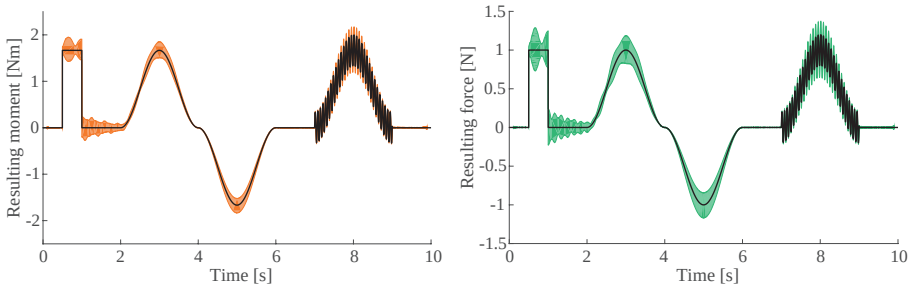

Figure 10: Estimated resulting baseline forces given stochastic modelling used for Figure 9 for Method 1. The black line is the true baseline force and the hatched area shows the upper and lower 98% uncertainty bounds for the estimated moment and force, respectively.

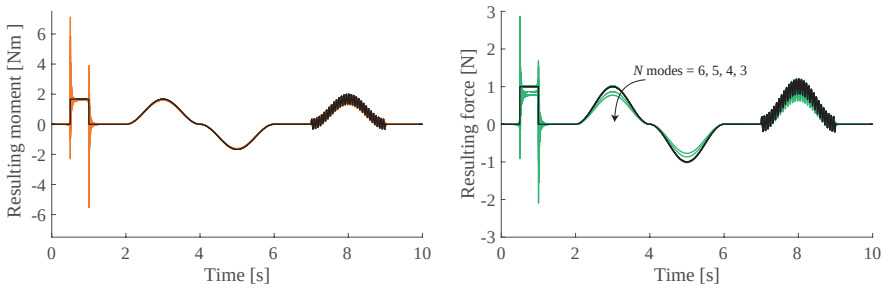

Figure 11: Resulting baseline forces given the different levels of modal truncation for Method 1. Every coloured line corresponds to an estimate given a number of modes, while the black lines are the true input.

Returning to the modal truncation example in Section 4, we once again compute the resulting load estimate from Method 1 as previously shown in Figure 3. Using the same analogy as explained above, a resulting baseline load is estimated for different number of modes included in the FRF. As the estimates from the truncation study are deterministic, we choose to plot each result on top of each other in Figure 11 together with the true baseline load. We see that the overturning moment is fairly accurate regardless of the number of modes included, while the shear force is drifting when modes are being omitted. When modes are omitted, Method 1 fails to estimate the point of attack and thus the scaling of the load, as it is seen in Figure 11. It should be noted that the degree of overshooting at the impulse is increased as modes are being omitted. Whether the resulting moment estimate remains stable is likely dependent on the static system.

There are some items which have not been covered by this study and which should be mentioned as they limit the conclusions.

- We have chosen a simple static system with plane deformation. The system is blessed by not having any closely spaced modes and is behaving perfectly linear. Now, if the system is more complex, which may be the case for most civil engineering structures, the generalization of the number of modes needed and the precision on the modal parameters may differ.
- We have not touched upon multiple load sources or a moving load.
- For this paper, the response function is driven by displacement measurements. It has not been assessed whether acceleration or strain measurements would have yielded different results.
- Only one noise level on the output signal has been studied.
- From Figure 8 it may seem like the variation in damping ratios and frequency yields nearly no effect on the load estimate. If the system is subjected to a harmonic load at a frequency near a natural frequency, these modal values may be vital for the load estimate.

8. Conclusion

The sensitivity in load identification following the uncertainty in modal parameters has been studied for two different methods. The uncertainties have been introduced stepwise into the system to demonstrate the influence of different parameters. It was found that fixing the spatial distribution of the load can compensate for the modal truncation in the response function. If one mode is dominating in the response, parameter estimation following this mode is crucial for the following load identification. However, modes with a resonant frequency above the frequency of the load still contribute to the quasi-static response, and omitting these modes will cause an error. A possible idea is to compensate through static deflection shapes / Ritz vector in the FRF matrix, but this has not been included. The spatial distribution of the load was fixed in Method 2 through the distribution vector $\underline{f_0}$. If the assumption regarding the load distribution $\underline{f_0}$ is not correct, this will introduce some systematic errors in the load estimate. Demonstrating this has been omitted from this paper.

Whether or not the stochastic modelling outlined in Section 5 is appropriate for a real-life structure will be left for the reader to decide. However, it has been demonstrated how variations in these parameters may alter the estimates on the loading, and shown how a sensitivity analysis may reveal flaws in the algorithm.

As a general observation, when doing vibration-based load identification, the algorithm for estimating the input must be supported by additional information besides the system response. This additional information may be in terms of the spatial distribution of the load - which was shown with Method 2 - or it may be other load models which are driven by wind speed measurements, wave gauge readings, local pressure measurements, or possibly information about the frequency content of the loading. Without aiding the inverse calculations with one of these, the uncertainty of the estimate will exceed what is acceptable. For most of the successful methods available in the literature, the spatial distribution of the load is also defined as a fixed measure, which leaves room for further research in this field.

Acknowledgments

The authors acknowledge the funding received from the Centre for Oil and Gas – DTU/Danish Hydrocarbon Research and Technology Centre (DHRTC).

Appendix A. Examining different loading positions

In order to demonstrate that the sensitivity is not uniquely related to the position of the load, a few additional cases are included in this appendix.

Appendix A.1. Case I

For the first case, the load is moved to the top node at DOF 5 (see Figure 1). Any other settings are the same as described previously. We jump to the result, where all modal parameters are treated as stochastic variables. The results are shown in Figure A.12, and again three selected points in time are highlighted. The error standard deviations are given in Table A.2. Note that for Method 2, we once again assume that the distribution is correctly foreseen i.e., $\underline{f_0} = [0\ 0\ 0\ 0\ 1\ 0]^T$.

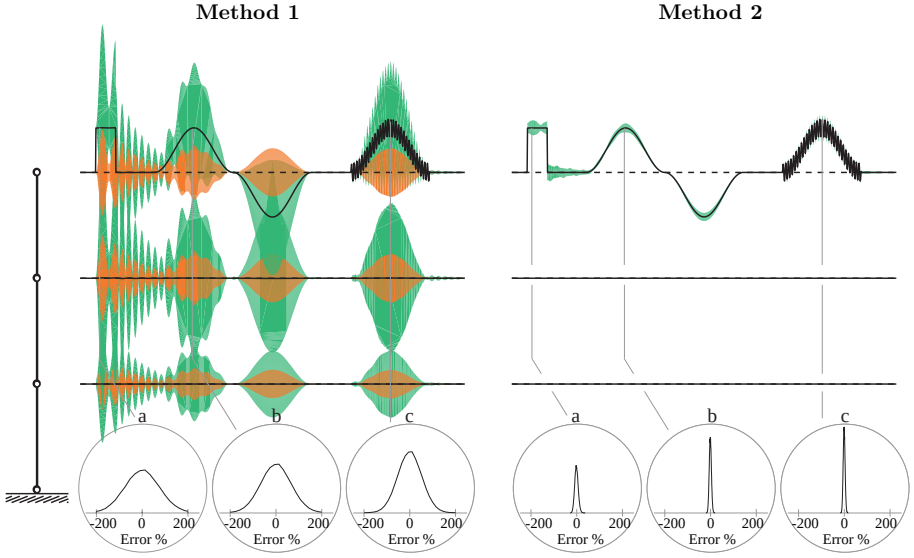

Figure A.12: The loading is applied at DOF 5. Natural frequencies, damping ratios and mode shapes are introduced as stochastic variables. The figure consequently shows the time history of the identified load using Method 1 and Method 2. Each time series shown has a 10 sec. duration. The solid lines are the mean values of the estimated force [N] and the dashed lines are the mean values of the estimated moment [Nm]. The hatched green area indicates uncertainty on the force while the hatched orange area is the uncertainty of the moment. Both are shown using the upper and lower 98% quantiles. Three selected points in time show the error probability density (in percent) for the estimated load in DOF 5. Note that the probability density is scaled differently between Method 1 and Method 2.

Table A.2: Error standard deviation for different levels of uncertainty and for three selected points in time. All based on the force estimate in DOF 5.

Uncertainties introduced	Method 1			Method 2		
	Error std [%]			Error std [%]		
	a	b	c	a	b	c
Natural frequencies	3.19	2.99	2.80	5.79	4.16	3.74
Natural frequencies and damping ratios	4.08	3.01	2.79	7.44	4.22	3.74
Natural frequencies, damping ratio and mode shapes	75.7	66.2	52.8	7.71	4.70	4.13

Appendix A.2. Case II

Next, we examine the consequences, if the loading is applied as a moment instead. Here, the moment is applied in DOF 4 i.e. at the same node as the base case shown in Figure 1. Again we jump to the stage where all modal parameters are treated as stochastic parameters. The results are shown in Figure A.13 and the error standard deviation for point a, b, and c is given in Table A.3. For Method 2, again we assume that the distribution is correctly foreseen i.e., $\underline{f_0} = [0\ 0\ 0\ 1\ 0\ 0]^T$.

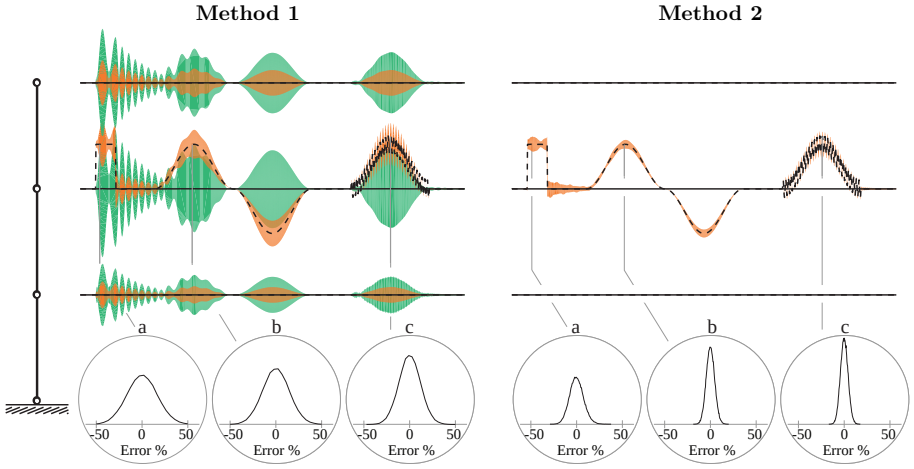

Figure A.13: The loading is applied at DOF 4. Natural frequencies, damping ratios and mode shapes are introduced as stochastic variables. The figure consequently shows the time history of the identified load using Method 1 and Method 2. Each time series shown has a 10 sec. duration. The solid lines are the mean values of the estimated force [N] and the dashed lines are the mean values of the estimated moment [Nm]. The hatched green area indicates uncertainty on the force while the hatched orange area is the uncertainty of the moment. Both are shown using the upper and lower 98% quantiles. Three selected points in time show the error probability density (in percent) for the estimated load in DOF 4. Note that the probability density is scaled differently between Method 1 and Method 2.

Table A.3: Error standard deviation for different levels of uncertainty and for three selected points in time. All based on the estimated moment in DOF 4.

Uncertainties introduced	Method 1			Method 2		
	Error std [%]			Error std [%]		
	a	b	c	a	b	c
Natural frequencies	1.89	2.15	2.17	5.57	4.05	3.76
Natural frequencies and damping ratios	1.90	2.16	2.17	7.37	4.11	3.77
Natural frequencies, damping ratio and mode shapes	16.6	14.7	11.8	7.62	4.57	4.13

Appendix B. Evaluating the number of sensors

The final case is dedicated to the study of how many sensors are required for a successful estimate. It has already been shown that for the truncated modal space, Method 1 does not yield any meaningful result despite having the full-field response measurements. This case study will hence be limited to Method 2 only. Since only a single load source is present, in theory, a single sensor should be sufficient of estimating the load. However, it is needless to say that the number of sensors needed depends on the position of the sensors. If a sensor is positioned at a nodal point for a mode, the corresponding modal load will be poorly estimated.

Reduction in sensor information can be done through the selection matrix $\underline{\underline{S_d}}$ as:

$$\underline{Y_{red}}(\omega) = \underline{\underline{S_d}}\,\underline{Y}(\omega) \tag{B.1}$$

here $\underline{Y_{red}}(\omega)$ will be the reduced measurement signal. The load scaling constant will consequently be

$$\hat{g}(\omega) = \left(\underline{\underline{S_d}}\,\underline{\underline{H}}(\omega)\,\underline{f_0}\right)^{\dagger}\underline{Y_{red}}(\omega) \tag{B.2}$$

For example, if only the response is measured in DOF 1 and 5, the selection matrix becomes

$$\underline{\underline{S_d}} = \begin{bmatrix} 1 & 0 & 0 & 0 & 0 & 0 \\ 0 & 0 & 0 & 0 & 1 & 0 \end{bmatrix} \tag{B.3}$$

This rewriting means that we can still identify loads in any of the six DOFs, although we only measure the response in a few selected DOFs. Figure B.14 shows the estimated loads using only two sensors located in DOF 1 and DOF 5.

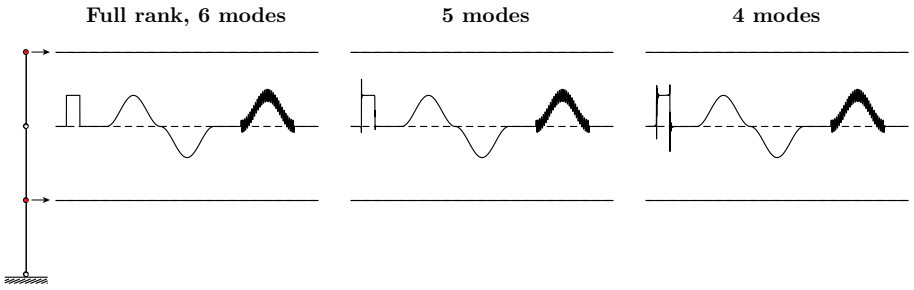

Figure B.14: Load estimate using Method 2 with displacement sensors at DOF 1 and DOF 5 as indicated by the arrows. The figure shows the time domain load estimate based on the number of modes included in the FRF matrix. Each time series shown has a 10 sec. duration. Solid lines show the force [N] and the dashed lines show the moment [Nm].

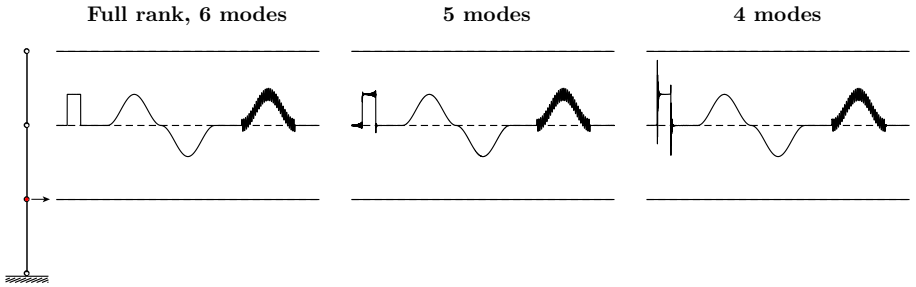

Figure B.15: Load estimate using Method 2 with a displacement sensor only at DOF 1 as indicated by the arrow. The figure shows the time domain load estimate based on the number of modes included in the FRF matrix. Each time series shown has a 10 sec. duration. Solid lines show the force [N] and the dashed lines show the moment [Nm].

Figure B.15 shows similar load estimate, but here, the response is measured at only the bottom node, in DOF 1. We see that even with one sensor, a reasonable estimate is obtained. Only the discontinuity at the impulse is off. Note that neither of the sensors in Figure B.14 and Figure B.15 are located at a mode nodal point.

The precision of the load estimate is evaluated from different numbers of modes in the FRF matrix. The load is consequently estimated at a location where the response is not measured. This corresponds to a flawless modal expansion process [38, 39] or system identification from a set of roving sensors. In general, one may argue that having more modes in the FRF than sensors pose a challenge from a system identification point of view. However, we will not justify this here.

References

[1] R. Brincker, C. Ventura, Introduction to Operational Modal Analysis, John Wiley and Sons, Ltd, Chichester, West Sussex, UK, 2015.

[2] E. Lourens, E. Reynders, G. D. Roeck, G. Degrande, G. Lombaert, An argumented Kalman filter for force identification in structural dynamics, Mechanical Systems and Signal Processing 27 (2012) 446–460.

[3] C. Ma, C. Ho, An inverse method for the estimation of input forces acting on non-linear structural systems, Journal of Sound and Vibration 275 (2004) 953–971.

[4] J. Liu, C. Ma, I. Kung, D. Lin, Input force estimation of a cantilever plate by using a system identification technique, Computer Methods in Applied Mechanics and Engineering 190 (2000) 1309–1322.

[5] F. Naets, J. Cuadrado, W. Desmet, Stable force identification in structural dynamics using Kalman filter and dummy-measurements, Mechanical Systems and Signal Processing 50-51 (2015) 235–248.

[6] K. Maes, K. van Nimmen, E. Lourens, A. Rezayat, P. Guillaume, G. D. Roeck, Verification of joint input-state estimation for force identification by means of in situ measurements on a footbridge, Mechanical Systems and Signal Processing 75 (2016) 245–260.

[7] J. Wambacq, K. Maes, A. Rezayat, P. Guillaume, G. Lombaert, Localization of dynamic forces on structures with an interior point method using group sparsity, Mechanical Systems and Signal Processing 115 (2019) 593–606.

[8] M. Aucejo, O. De Smet, J. Deü, Practical issues on the applicability of Kalman filtering for reconstructing mechanical sources in structural dynamics, Journal of Sound and Vibration 442 (2019) 45–70.

[9] L. Wang, X. Wang, X. Li, Inverse system method for dynamic loads identification via noisy measured dynamic responses, Engineering Computations 32 (2016) 1070–1094.

[10] L. Wang, X. Wang, Dynamic loads identification in presence of unknown but bounded measurement errors, Inverse Problems in Science and Engineering 23 (2015) 1313–1341.

[11] L. Wang, Y. Liu, Y.Liu, Dynamic loads identification in presence of unknown but bounded measurement errors, Advances in Engineering Software 131 (2019) 77–89.
[12] Y. Liu, W. Shepard, Dynamic force identification based on enhanced least squares and total least-squares scheme in the frequency domain, Journal of Sound and Vibration 282 (2005) 37–60.
[13] M. Vigsø, M. Tarpø, J. Hansen, R. Brincker, C. Georgakis, Scenario based approach for load identification, Proceedings of the International Modal Analysis Conference, IMAC (2018) 117–125.
[14] M. Vigsø, J. Kristoffersen, R. Brincker, C. Georgakis, Indirect wave load estimates using operational modal analysis – preliminary findings, Proceedings of the International Ocean and Polar Engineering Conference, ISOPE (2018).
[15] M. Aenlle, R. Brincker, P. Fernández, A. Fernández, Load estimation from modal parameters, Proceedings of the International Operational Modal Analysis Conference, iomac 1 (2007) 39–50.
[16] B. Dobson, E. Rider, A review of the indirect calculation of excitation forces from measured structural data, Proceedings of the Institution of Mechanical Engineers, Part C: Mechanical Engineering Science 204 (1990) 69–75.
[17] K. Stevens, Force identification problems - an overview, Proceedings of the SEM Spring Conference on Experimental Mechanics (1987) 838–844.
[18] R. Cumbo, T. Tamarozzi, K. Janssens, W. Desmet, Kalman-based load identification and full-field estimation analysis on industrial test case, Mechanical Systems and Signal Processing 117 (2019) 771–785.
[19] Z. He, X. Lin, E. Li, A non-contact acoustic pressure-based method for load identification in acoustic-structural interaction system with non-probabilistic uncertainty, Applied Acoustics 148 (2019) 223–237.
[20] Z. He, J. Hu, E. Li, An uncertainty model of acoustic metamaterials with random parameters, Applied Acoustics 62 (2018) 1023–1036.
[21] B. Hillary, Indirect Measurement of Vibration Excitation Forces, PhD Thesis, Imperial College of Science and Technology, London, 1983.
[22] W. Flannelly, F. Bartlett, T. Fonsberg Jr, Laboratory Verification of Force Determination, A Potential Tool for Reliability Testing, Kaman Aerospace Corporation, Old Windsor Road, Bloomfield Conn., 1977.
[23] F. Bartlett, W. Flannelly, Model verification of force determination for measuring vibratory loads, Journal of the American Helicopter Society 24 (2) (1979) 10–18.
[24] J. Fabunmi, Effects of structural modes on vibratory force determination by the pseudoinverse technique, American Institute of Aeronautics and Astronautics Journal 24 (1986) 504–509.
[25] A. Brandt, Noise and Vibration Analysis, John Wiley and Sons, Ltd, West Sussex, UK, 2011.
[26] R. Penrose, A generalized inverse for matrices, Mathematical Proceedings of the Cambridge Philosophical Society 51 (1955) 406–413.
[27] R. Brincker, C. Ventura, P. Andersen, Why output-only modal testing is a desirable tool for a wide range of practical applications, Proceedings of the Internatinoal Modal Analysis Conference IMAC (2003).
[28] M. Aenlle, R. Brincker, A. Canteli, Load estimation from natural input modal analysis, Proceedings of the International Modal Analysis Conference, IMAC (2005).
[29] Z. He, Z. Zhang, E. Li, Multi-source random excitation identification for stochastic structures based on matrix perturbation and modified regularization method, Mechanical Systems and Signal Processing 119 (2019) 266–292.
[30] B. Wang, C. Chiu, Determination of unknown impact force acting on a simply supported beam, Mechanical Systems and Signal Processing 17 (3) (2003) 683–704.
[31] E. Parloo, P. Verboven, P. Guillaume, M. van Overmeire, Force identification by means of in-operation modal models, Journal of Sound and Vibration 262 (2003) 161–173.
[32] J. Zhang, F. Zhang, J. Jiang, Load localization and reconstruction using a variable separation method, Shock and Vibration 2019 (2019) Article ID 4207473.
[33] E. Kreyszig, Advanced Engineering Mathematics, 10th Edition, John Wiley & Sons, Inc, West Sussex, UK, 2011.
[34] J. Schott, Matrix Analysis for Statistics, 3rd Edition, John Wiley & Sons, Inc, West Sussex, UK, 2016.
[35] M. Tarpø, M. Vigsø, R. Brincker, Modal truncation in experimental modal analysis, Proceedings of the International Modal Analysis Conference, IMAC (2018) 143–152.
[36] N. R. Maddox, On the number of modes necessary for accurate response and resulting forces in dynamic analyses, Journal of Applied Mechanics 42 (1975) 516–517.
[37] A. Zygmund, Trigonometrical series, Dover Publications, 1955.
[38] J. O'Callahan, P. Avitabile, R. Riemer, System equivalent reduction expansion process, Proceedings of the International Modal Analysis Conference, IMAC (1989).

[39] R. Brincker, A. Skafte, M. Anelle, A. Sestieri, W. D'Ambrogio, A. Canteli, A local correspondence principle for mode shapes in structural dynamics, Mechanical Systems and Signal Processing Vol: 45 (2014) 91–104.
[40] G. Tondreau, E. Reynders, A. Deraemaeker, Towards a more realistic modelling of the uncertainty on identified mode shapes due to measurement noise, Journal of Physics - Conference series 305 (2011).
[41] E. Reynders, R. Pintelon, G. D. Roeck, Uncertainty bounds on modal parameters obtained from stochastic subspace identification, Mechanical Systems and Signal Processing (2007).
[42] L. Zhang, R. Brincker, P. Andersen, An overview of operational modal analysis: Major development and issues, Proceedings of the International Operational Modal Analysis Conference, iomac (2005) 179–190.
[43] M. Tarpø, T. Friis, P. O. M. Juul, C. Georgakis, R. Brincker, Automated reduction of statistical errors in the estimated correlation function matrix for operational modal analysis, Mechanical Systems and Signal Processing 132 (2019) 790–805.
[44] E. Cheynet, J. Jakobsen, J. Snæbjörnsson, Damping estimation of large wind-sensitive structures, International Conference on Structural Dynamics, EURODYN (2017).
[45] R. Allemang, The modal assurance criterion (MAC): Twenty years of use and abuse, Journal of Sound and Vibration 37 (2003) 14–23.
[46] K. Maes, G. Lombaert, The influence of out-of-band modes in system inversion, Mechanical Systems and Signal Processing 115 (2019) 173–187.

Chapter 9

Modal truncation

Paper III

"Modal truncation in experimental modal analysis"

Marius Tarpø, Michael Vigsø and Rune Brincker

Published in Proceedings of the 36$^{\text{th}}$ International Modal Analysis Conference, IMAC, Orlando, 2018

This chapter presents a study of response truncation by considering out-of-band modes and spatial distribution of the load. The author has contributed to the ideation and the experiment while Marius Tarpø has performed the main part of the analysis and the writing of the paper. The paper has been formatted with minor grammatical adjustments to suit this thesis.

Modal truncation in experimental modal analysis

Marius Tarpø[a,*], Michael Vigsø[a], Rune Brincker[b]

[a] *Aarhus University, Inge Lehmanns Gade 10, 8000 Aarhus, Denmark*
[b] *Technical University of Denmark, Brovej 118, 2800 Kgs. Lyngby, Denmark*

Abstract

Some methods in experimental modal analysis rely on a finite set of modes and they neglect the higher modes. However, this approach causes a truncation of the modal decomposition and the modal truncation introduces errors of unknown magnitude. In this paper the effect of modal truncation is investigated on a test specimen in the laboratory. It is found that the system response is dependent of the frequency and the distribution of the load. Modal truncation can introduce significant errors if the set of mode shapes does not efficiently span the spatial distribution of the load.

Keywords: Operational modal analysis, Experimental modal analysis, Modal truncation, Modal decomposition

1. Introduction

The modal decomposition describes the structural dynamic response where the mode shapes of the system uncouple the dynamic response into the modal coordinates. When we truncate the modal decomposition to only include the first number of modes, we have a smaller set of modal coordinates to describe the system. This simplifies the structural response and it is frequently used to ease the calculation in structural dynamics. In experimental modal analysis, we identify a number of modes and we use them with experimental techniques for different purposes like; full field response estimation, fatigue analysis, load estimation, damage detection etc..

Normally, the truncated set of mode shapes provides good results however it might result in significant errors in certain instances where omitted modes contribute to the response [1–7]. The gross behavior of structures is generally captured by the modes that are located in the frequency range of the load [3, 8]. However, higher modes might influence the localized behavior by their non-trivial contribution. Therefore, a truncation of the modal decomposition can lead to errors of the representation of the response [1, 5, 7, 8]. This is also the case for experimental techniques that uses a truncated set of mode shapes to represent the structural response.

The phenomenon of modal truncation is described in structural computation and finite element modelling. Generally, these fields of research state that we can calculate the response as a combination of the dynamic responses of the lower modes and a correction term, which is based on the quasi-static response of the remaining modes. Two types of corrections are created; static

*Corresponding author
Email addresses: martar@eng.au.dk (Marius Tarpø), mvigso@eng.au.dk (Michael Vigsø), runeb@byg.dtu.dk (Rune Brincker)

Published in the Proceedings of the International Modal Analysis Conference, IMAC
This paper has been formatted to suit this thesis *February 2018*

residual and residual vectors. The static residual uses static correction terms to adjust for the modal truncation. Whereas the other method make use of residual modes, also called "assumed modes" or "pseudo modes", combined with the mode shapes [9].

This paper showcases the potential problem of the modal truncation in an experimental setting. We find that the required number of modes in a modal decomposition depends on the frequency range and the spatial distribution of the loading.

2. Theory

2.1. Truncation of the modal decomposition

The modal decomposition says that any response from a linear system is a linear composition of its mode shapes. This means that the response of a linear structure is located in the subspace of its mode shapes.

$$\underline{y}(t) = \sum_{i=1}^{N} \underline{\phi_i}\, q_i(t) \tag{1}$$

where $\underline{y}(t) \in \mathbb{R}^{N\times 1}$ is system response, $\underline{\phi_i} \in \mathbb{R}^{N\times 1}$ is the mass normalized mode shape, $q_i(t)$ is the modal coordinate for mode i and N is the total number of degrees of freedom in the system.

Let us say that we only use K modes in the modal decomposition then we have a smaller set of modes to describe the system. Hence, we have introduced an error in our representation of the structural response due to the modal truncation. This error is often referred to as the residual effect.

$$\underline{\varepsilon}(t) = \sum_{i=K+1}^{N} \underline{\phi_i}\, q_i(t) \tag{2}$$

As long as this error is insignificant then the truncation of the modal decomposition is acceptable. However, it is hard to estimate the magnitude of this error. We will look at the modal coordinates to get a better understanding of the truncation error. We calculate the modal response in the frequency domain.

$$Q_i(\omega) = H_i(\omega)\ \underline{\phi_i}^T\, \underline{X}(\omega) \tag{3}$$

where $\underline{X}(\omega) \in \mathbb{C}^{N\times 1}$ is the load in the frequency domain, $H_i(\omega)$ is the frequency response function for the i^{th} mode.

$$H_i(\omega) = \frac{1}{m_i\left(-\omega^2 + j\,2\zeta_i\omega_i\omega + \omega_i^2\right)} \tag{4}$$

where m_i is the modal mass, ω_i is natural frequency and ζ_i is the damping ratio for mode i.

In the following, we will look at two types of loading: random or fixed spatial distribution of the load. A load with a fixed spatial distribution can be separated like

$$\underline{X}(\omega) = \underline{F}\, S(\omega) \tag{5}$$

where $\underline{F} \in \mathbb{R}^{N\times 1}$ is the spatial distribution of the load and $S(\omega)$ is the scalar function defining the temporal variation of the load. Therefore, we can rewrite the expression for the modal coordinates in the frequency range, Eq. (3), if the load has a fixed spatial distribution.

$$Q_i(\omega) = H_i(\omega)\, S(\omega)\, \underline{\phi_i}^T\, \underline{F} \tag{6}$$

We see that the contribution of each mode is dependent of the scalar product of frequency response function and the frequency range of the load. However, it is also dependent on the inner vector product between the given mode shape and the spatial distribution of the load. This tells us that a modal coordinate is given both by the frequency range and the spatial distribution of the load. But if the load has a random spatial distribution then the modal response only depends on the frequency range of the load. Therefore, the residual effect depends on frequency range and spatial distribution of the load.

Modal truncation of the quasi-static contribution

Often, the omitted modes are located above the frequency range of the load when we truncate the modal decomposition. When the load frequency is located way before the natural frequencies of the modes then the omitted modes act quasi-static.

We will show this by an example where the frequency range of the load is restricted and we omit all modes outside this range. Here we assume that the first omitted mode n and all higher modes have much higher natural frequencies, ω_n, than the highest load frequency, ω_x. This means; $\omega_x << \omega_n$. So we can rewrite the frequency response function, Eq. (4), for the truncated modes when we roughly approximate that any term in denominator with ω is insignificant compared with the term ω_n^2. Then the modal coordinates for truncated modes are

$$\widetilde{Q}_n(\omega) \approx \begin{cases} \dfrac{1}{m_n \omega_n^2} S(\omega) \, \underline{\phi_n}^T \, \underline{F} & 0 \leq \omega \leq \omega_x \\ 0 & \omega > \omega_x \end{cases} \tag{7}$$

We see on Eq. (7) that the modal coordinates are no longer a dynamic response but a quasi-static response. Therefore, we approximate the residual effect as

$$\underline{\widetilde{\varepsilon}}(t) \approx s(t) \sum_{n=K+1}^{N} \frac{\underline{\underline{\phi_n}} \, \underline{\phi_n}^T \underline{F}}{m_n \omega_n^2} \tag{8}$$

This is a quasi-static error, which depends on the inner vector product between the mode shape and spatial distribution of the load and the modal mass and frequency. So a truncation of higher modes might give a amplitude error of the system response because we have removed a quasi-static contribution from the residual modes.

2.2. Reduction of subspace

We would like to be able to remove the influence of certain modes from a measured system response in order to access the effect of modal truncation. In order to do this we will use a linear transformation, which we base on the modal decomposition. The estimated modal coordinates for K modes is found when we project the system response onto the subspace of the mode shapes.

$$\underline{\hat{q}}(t) \quad = \quad \underline{\underline{\Phi_K}}^{\dagger} \, \underline{y}(t) \tag{9}$$

where $\underline{\hat{q}}(t) \in \mathbb{R}^{K \times 1}$ is the estimated modal coordinates and $\underline{\underline{\Phi_K}} \in \mathbb{R}^{N \times K}$ is the truncated mode shape matrix, which contains the applied mode shape as columns. Then we can find the truncated system response.

$$\underline{\hat{y}}(t) = \underline{\underline{\Phi_K}} \, \underline{\hat{q}}(t) \tag{10}$$

where $\underline{\hat{y}}(t) \in \mathbb{R}^{N \times 1}$ is the truncated system response with a reduced subspace. This transformation projects the response onto the column space of the mode shape matrix and thereby it reduces the subspace of the response to only include the given modes.

2.3. Quality measurements

It is useful to access the difference between a measured and the equivalent truncated response so we know the errors of a modal truncation. To assess the difference, we utilize the coefficient of determination, $R^2_{t,i}$, from model validation in both time and frequency domain [10].

$$R^2_{t,i} = 1 - \frac{\sum_{k=1}^{M} \left(y_i(t_k) - \hat{y}_i(t_k)\right)^2}{\sum_{k=1}^{M} \left(y_i(t_k) - \mathrm{E}\left[y_i(t)\right]\right)^2} \tag{11}$$

$$R^2_{f,i} = 1 - \frac{\sum_{k=1}^{M} \left(|Y_i(f_k)| - |\hat{Y}_i(f_k)|\right)^2}{\sum_{k=1}^{M} \left(|Y_i(f_k)| - \mathrm{E}\left[|Y_i(f)|\right]\right)^2} \tag{12}$$

where $\mathrm{E}[X]$ is the expected value of X, $y_i(t)$ and $\hat{y}_i(t)$ are the measured and truncated response for sensor i and $Y_i(f)$ and $\hat{Y}_i(f)$ are the Fourier transformed measured and truncated response for sensor i. Finally, M represents the number of samples for each sensor.

3. Case study

We will show the effect of modal truncation on a small structure in the laboratory. The test specimen is a T-shaped steel structure, which is fixed with claps, see Figure 1. In this case study, we will assume that we are only interested in the first 100 Hz of the system. We will identify the modes located inside this frequency region and we will project the response onto the column space of the mode shapes using equation (10). By projecting the response onto the subspace of the used mode shapes, we remove the contribution of the higher modes and all noise that are perpendicular to this subspace. This is to illustrate the effect of neglecting the contribution of the others modes in an experimental setting.

Figure 1: Photo of the test specimen in the lab.

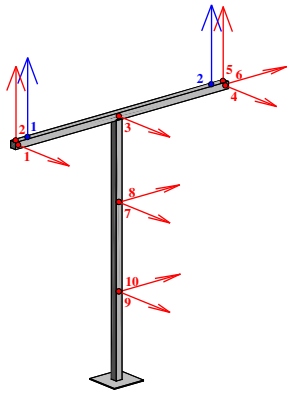

Figure 2: Position of sensors, red arrows are for uniaxial accelerometers and blue arrows are the geophones.

In this paper, we will call the modes located in given frequency range for the "*dynamic modes*" and we will define the modes located outside this range as "*residual modes*". So we will look at the truncation error by using the dynamic modes that are located in the given frequency range. Then we will add one and then two residual modes to the modal decomposition from outside this frequency range and calculate the truncation error. This is in order to see if modes outside the frequency range will have a contribution to the system response.

3.1. Experimental setup

Ten uniaxial accelerometers with a sensitivity of 100 mV/g and two geophones are attached to the structure as seen on Figure 2. The geophones work as shakers when we apply a current to them. Compressed air excites the structure from three directions and this loading creates turbulence around the structure and the excitation resembles white Gaussian noise. One set of data is acquired where the geophones are idle and this data set is used to identify the modal parameters using operational modal analysis [11].

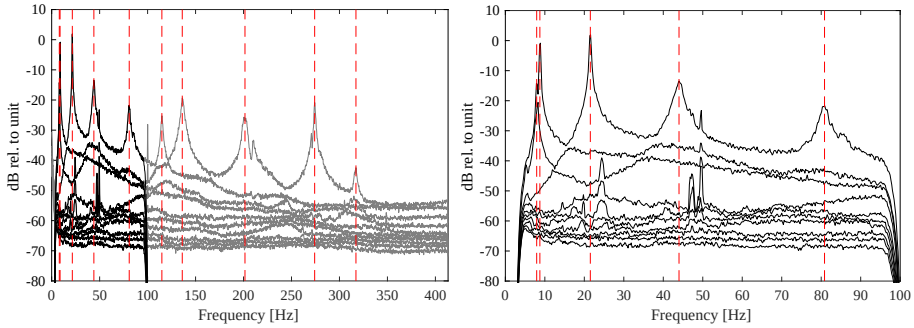

Figure 3: Case 1, singular value decomposition of the spectral density matrix.

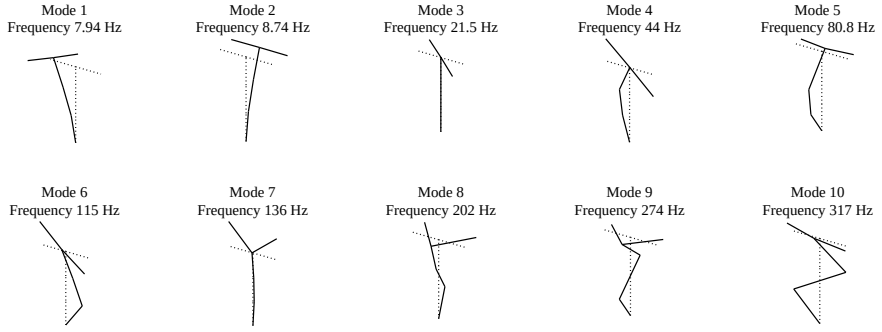

Figure 4: Identified experimental mode shapes.

A time length of 300 seconds is used with a sampling frequency of 1651 Hz for each data set. The data is decimated to a new frequency of 825.5 Hz [11]. We bandpass filter the data sets from 5 to 100 Hz, see Figure 3. The low frequency cut-off is applied to remove noise from DC.

An Operational Modal Analysis is preformed where the *Frequency Domain Decomposition* is used to identify the modes [12]. Five dynamic modes are identified in the frequency region up to 100 Hz and five residual modes outside this range, see Figure 3 and Figure 4.

3.2. Case 1

In this case, the geophones are idle and only compressed air is used as excitation and therefore the load has no defined spatial distribution. The measured response is projected onto the subspace of the five dynamic modes using equation (10). Afterwards, we add one and then two residual modes to the modal decomposition. We calculate the coefficient of determination in time and frequency domain for each version of the modal decomposition, see Table 1.

Generally, we do not achieve a better representation of the response by adding residual modes to the modal decomposition. The two worst truncated responses are sensor 8 and 10 and the recorded acceleration for these two sensors plotted on Figure 5 and Figure 6 for the scenario with dynamic modes only.

Table 1: Quality measurements for Case 1.

		Sensor 1	Sensor 2	Sensor 3	Sensor 4	Sensor 5	Sensor 6	Sensor 7	Sensor 8	Sensor 9	Sensor 10
Dynamic modes	R_t^2	1.0000	0.9916	0.9990	1.0000	0.9919	0.9958	0.9997	0.9969	0.9977	0.9850
	R_f^2	1.0000	0.9955	0.9995	1.0000	0.9975	0.9977	0.9998	0.9979	0.9985	0.9866
Dynamic modes + 1 residual mode	R_t^2	1.0000	0.9924	0.9990	0.9999	0.9917	0.9992	0.9997	0.9986	0.9977	0.9973
	R_f^2	1.0000	0.9960	0.9995	1.0000	0.9974	0.9995	0.9998	0.9991	0.9985	0.9984
Dynamic modes + 2 residual modes	R_t^2	1.0000	1.0000	0.9990	1.0000	1.0000	0.9996	0.9997	0.9986	0.9977	0.9978
	R_f^2	1.0000	1.0000	0.9995	1.0000	1.0000	0.9997	0.9998	0.9991	0.9985	0.9986

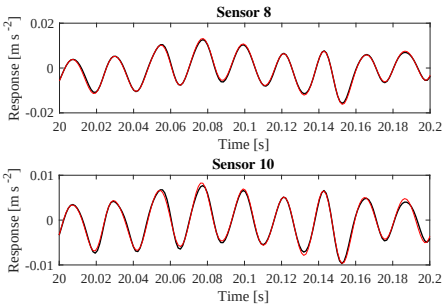

Figure 5: Case 1, only dynamic modes: Response of truncated response, black is the measured and red is the truncated response.

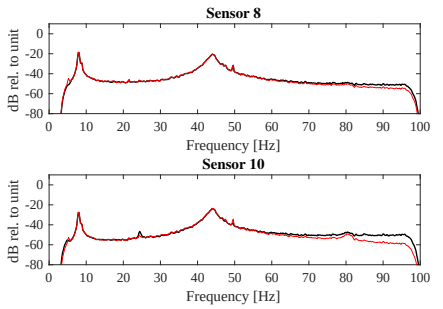

Figure 6: Case 1, only dynamic modes: Spectrum of truncated response, black is the measured and red is the truncated response.

3.3. Case 2

In the next case, we excite the structure with compressed air. Additionally, we apply a current to the second geophone so it excites the structure at a frequency of 64 Hz, see Figure 7 for spectral density plot. This means that a significant part of the load has a fixed spatial distribution in this case.

Like in Case 1, the five dynamic mode shapes are used for the projection of the subspace using Eq. (10). Next, we add one and two residual modes from outside the frequency region. Then the coefficients of determination are calculated for the time and frequency domain, see Table 2.

Table 2: Quality measurements for Case 2.

		Sensor 1	Sensor 2	Sensor 3	Sensor 4	Sensor 5	Sensor 6	Sensor 7	Sensor 8	Sensor 9	Sensor 10
Dynamic modes	R_t^2	0.9999	0.9759	0.9991	0.9999	0.9236	0.8625	0.9991	0.9947	0.9976	0.9745
	R_f^2	0.9999	0.9759	0.9996	0.9999	0.9227	0.8565	0.9991	0.9947	0.9984	0.9745
Dynamic modes + 1 residual mode	R_t^2	0.9999	0.9709	0.9991	0.9999	0.9300	0.9718	0.9994	0.9990	0.9977	0.9993
	R_f^2	0.9999	0.9708	0.9995	1.0000	0.9293	0.9706	0.9995	0.9991	0.9985	0.9994
Dynamic modes + 2 residual modes	R_t^2	1.0000	1.0000	0.9990	0.9999	1.0000	0.9977	0.9997	0.9989	0.9978	0.9989
	R_f^2	1.0000	1.0000	0.9995	1.0000	1.0000	0.9977	0.9998	0.9990	0.9985	0.9990

Generally, the truncated response using only the dynamic mode has a high correlation with the measured response but a few sensors deviate. The two worst channels are for sensor 5 and 6 and the responses for the sensors have wrong amplitudes, see Figure 8 and Figure 9. By adding residual modes, we see an increase in the quality measurements, which is especially evident for sensor 5 and 6. The quality fit for sensor 6 increases with more than 0.1 by adding one residual mode. Whereas, sensor 5 needs two residual modes to have a quality fit above 0.93. The response for sensor 5 and 6 using two residual modes are plotted in Figure 10 and Figure 11.

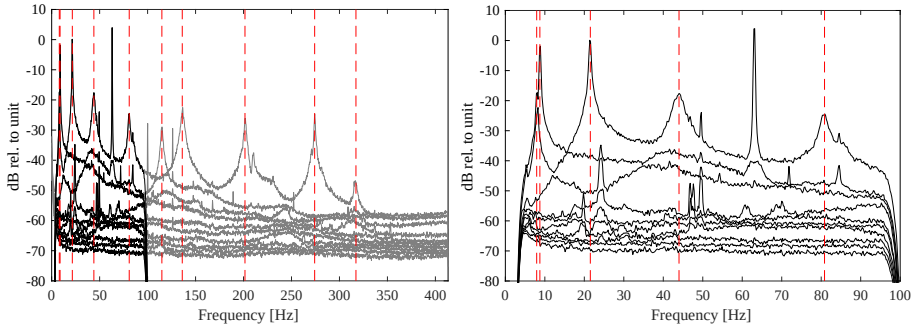

Figure 7: Case 2, singular value decomposition of the spectral density matrix.

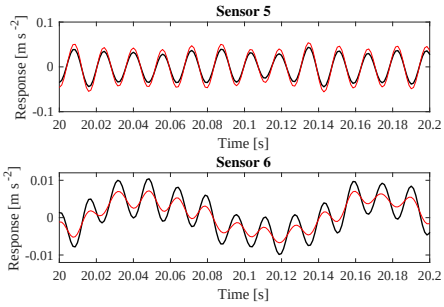

Figure 8: Case 2, only dynamic modes: Response of truncated response, black is the measured and red is the truncated response.

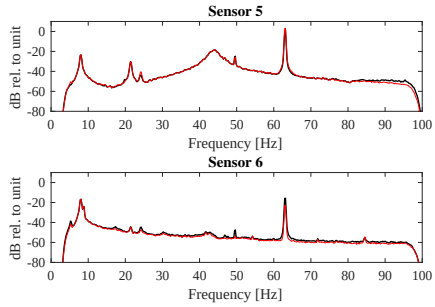

Figure 9: Case 2, only dynamic modes: Spectrum of truncated response, black is the measured and red is the truncated response.

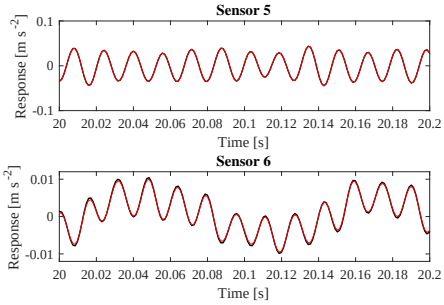

Figure 10: Case 2, dynamic modes + 2 residual modes: Response of truncated response, black is the measured and red is the truncated response.

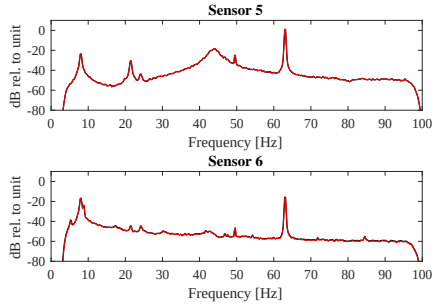

Figure 11: Case 2, dynamic modes + 2 residual modes: Spectrum of truncated response, black is the measured and red is the truncated response.

4. Discussion

First, we should note that the projection onto a fixed number of mode shapes removes noise and modal response alike if their subspaces are orthogonal to the new subspace of the projection. Therefore, we will remove noise and this reduction of noise will affect the quality measurements since we are using a signal with noise as reference. The resolution of the experimental mode shapes also has an influence on the assumption that we can reduce the subspace. However, we will assume that these errors are insignificant.

Overall the modal truncation has a low error and most sensors maintain the same response as measured when we use the five dynamic mode shapes. In Case 1, the first five dynamic mode shapes were sufficient to span the measured response but in Case 2 we needed additional mode shapes to accurate span the measured response for a few of the sensors. Here sensor 5 and 6 are less precise in Case 2 where a part of the load had a defined load pattern. By observing Figure 2, we can see that the excitation by the second geophone primarily results in responses for sensor 2, 5 and 6. Furthermore, we can observe in Figure 4 that the first five mode shapes do not span this

movement. The sixth and seventh mode shapes add more information to better span the response that is caused by the geophone.

In these tests, we see that an excitation with a fixed spatial distribution has a higher residual effect compared with an excitation with a random load pattern. This is in accordance with the theory of the residual effects. The theory suggests that a fixed spatial distribution of the load causes contributions from modes outside the frequency of load. Therefore, a fixed load pattern seems to activate quasi-static response of the higher modes even-though the frequency of the load is located before the natural frequencies of these modes. These modes should be included in the lower frequency region if we want a proper representation of the response for localized behavior.

5. Conclusion

In this paper we have shown the possible errors caused by truncating the modal decomposition in experimental modal analysis. Often this truncation error is insignificant but it is pronounced if a significant part of load has a fixed spatial distribution. The magnitude of the error is hard to estimate but localized structural behavior seem to be highly affected by this residual effect. This means that experimental techniques that use a truncated set of modes to describe the response might introduce errors in localized behavior.

To sum up, we cannot rely purely on the frequency range to choose the number of modes in a experimental modal analysis since the combination of higher modes may contribute to the response. Therefore, modal truncation introduces errors in response representation if the set of mode shapes inefficiently span the spatial distribution of the load.

Acknowledgments

The authors acknowledge the funding received from the Centre for Oil and Gas – DTU/Danish Hydrocarbon Research and Technology Centre (DHRTC).

A special thanks to Jannick Balleby Hansen for helping with the experimental tests.

References

[1] D. Lui, H. Chung, W. Chang, The errors caused by modal truncation in structure dynamic analysis, Proceedings of the 18th International Modal Analysis Conference, IMAC (2000) 1455–1460.

[2] N. R. Maddox, On the number of modes necessary for accurate response and resulting forces in dynamic analyses, Journal of Applied Mechanics 42 (1975) 516–517.

[3] J. H. Vugts, I. M. Hines, R. Nataraja, W. Schumm, Modal superposition v direct solution techniques in the dynamic analysis of offshore structures, Behaviour of off-shore structures (1979) 23–29.

[4] P. Léger, J. M. Ricles, L. J. Robayo, Reducing modal truncation error in wave response analysis of offshore structures, Communications in applied numerical methods 6 (1) (1990) 7–16.

[5] P. Léger, E. L. Wilson, Generation of load dependent ritz transformation vectors in structural dynamics, Engineering Computations 4 (4) (1987) 309–318.

[6] J. M. Dickens, J. M. Nakagawa, M. J. Wittbrodt, A critique of mode acceleration and modal truncation augmentation methods for modal response analysis, Computers and Structures 62 (6) (1997) 985–998.

[7] O. E. Hansteen, K. Bell, On the accuracy of mode superposition analysis in structural dynamics, Earthquake Engineering and Structural Dynamics 7 (1979) 405–411.

[8] P. Avitabile, P. Pingle, Prediction of full field dynamic strain from limited sets of measured data, Shock and Vibration 19 (5) (2012) 765–785.

[9] N. Roy, A. Girard, Impact of residual modes in structural dynamics, Proceedings of the European Conference on Spacecraft Structure, Materials and Testing (2005).

[10] P. C. Hansen, V. Pereyra, G. Scherer, Least squares data fitting with applications, Johns Hopkins University Press, Baltimore, MD, 2013.
[11] R. Brincker, C. Ventura, Introduction to Operational Modal Analysis, John Wiley and Sons, Ltd, Chichester, West Sussex, UK, 2015.
[12] R. Brincker, L. M. Zhang, P. Andersen, Modal identification of output-only systems using frequency domain decomposition, Smart Materials and Structures 10 (3) (2001) 441–445.

Chapter 10

Fluid-structure interaction

Paper IV

"Operational modal analysis and fluid-structure interaction"

Michael Vigsø, Thomas Kabel, Marius Tarpø, Rune Brincker and Christos Georgakis

Published in Proceedings of the 28th International Conference on Noise and Vibration Engineering, ISMA, Leuven, 2018

This chapter presents a study of the influence of water surrounding a structure. Changes in modal parameters are observed as the water level rises. The author has performed the main part of the ideation, experiments, analysis and the writing of the paper. Thomas Kabel contributed to the success of the experiments while Marius Tarpø aided the ideation and analysis. The paper has been formatted with minor grammatical adjustments to suit this thesis.

Operational modal analysis and fluid-structure interaction

Michael Vigsø[a,*], Thomas Kabel[a], Marius Tarpø[a], Rune Brincker[b], Christos Georgakis[a]

[a] *Aarhus University, Inge Lehmanns Gade 10, 8000 Aarhus, Denmark*
[b] *Technical University of Denmark, Brovej 118, 2800 Kgs. Lyngby, Denmark*

Abstract

Operational modal analysis (OMA) has in the last decade shown its potential in the field of offshore structures such as oilrigs and wind turbines etc. Typically, the estimated modal parameters will be used in conjunction with a finite element (FE) model. However since bottom-fixed offshore structures typically will be semi-submerged this affects the modal parameters by fluid-structure interaction. Fluid surrounding a structure is known to retard the response and locally introduce an increase in mass and damping. These local changes yield a complex alteration of the modal parameters and this paper highlights these effects by a wave flume experiment conducted on a cantilever structure. The structure is a scaled offshore structure and its modal parameters are examined at different water levels ranging from dry state to 60 % submerged.

Keywords: Modal analysis, Added mass, Fluid-structure interaction

1. Introduction

Modal analysis is an effective tool in describing the dynamic behavior of a structure. When dealing with civil engineering structures, traditional experimental modal analysis (EMA) has some shortcomings and hence opens the playground for its cousin named operational modal analysis (OMA). OMA utilizes the operational conditions in providing the excitation of the structure and if the loading is approximating white noise, the modal parameters can elegantly be extracted from the structural response. The application of OMA is gaining ground and is becoming the preferred approach when evaluating modal properties of offshore structures. [1] The motivation for making modal analysis may be multiple; for instance in the field of structural health monitoring (SHM), model updating, fatigue estimation or indirect load estimation. Most of these disciplines use an FE model (updated to insitu conditions) as a basis.

There will always be some natural variations in the estimated modal parameters; besides estimation- or statistical error also environmental changes such as wind speed, scour or other seabed changes, structural degradation, mass loading, temperature or even tidal variations can cause the modal parameters to fluctuate. This paper will focus on how variations in the surrounding water may alter the dynamics of the structure.

The fluid-structure interaction is a complex topic and existing research in this area is plentiful. Both analytical, experimental and numerical work has been done in the past, e.g. [2–5]. The

*Corresponding author
Email addresses: mvigso@eng.au.dk (Michael Vigsø), tk@eng.au.dk (Thomas Kabel), martar@eng.au.dk (Marius Tarpø), runeb@byg.dtu.dk (Rune Brincker), cg@eng.au.dk (Christos Georgakis)

Published in the Proceedings of the International Conference on Noise and Vibration Engineering, ISMA
This paper has been formatted to suit this thesis *September 2018*

content of this paper does not intend to challenge these works, instead it will demonstrate an application in the field of operational modal analysis conducted on a miniature offshore model. The results shown in this paper are preliminary findings which will be the basis for a later study, where an accurate model update is required. The model design does not descend from any actual physical structure, but is constructed as a simple cantilever with a topside in order to better monitor the torsional modes.

2. Experiment setup

The experimental campaign is conducted at Luminy University at Marseille, France in 2018. A cantilever structure made from plexiglass will be the scope for this study. The structure is a cylindrical mono tower with a truss box topside. The columnar part of the model is constructed by segments bolted together through an internal flange. Each segment is 200 mm in length and has an outer diameter of 150 mm. The structure is dry on the inside at all times during the tests. The topside has an outer geometry of $l \times b \times h$ of $400 \times 200 \times 200$ mm. The entire model is situated on a load cell connected to an aluminium base plate, which yields a total height of the model to be 1485 mm. The maximum water level, which can be applied in the flume, is 900 mm as indicated by Figure 1 a) and b). The sizing of the segments is primarily based on accessibility concerns regarding sensor installation. The joints between the circular sections are waterproofed through a gasket which may be seen in Figure 1 c).

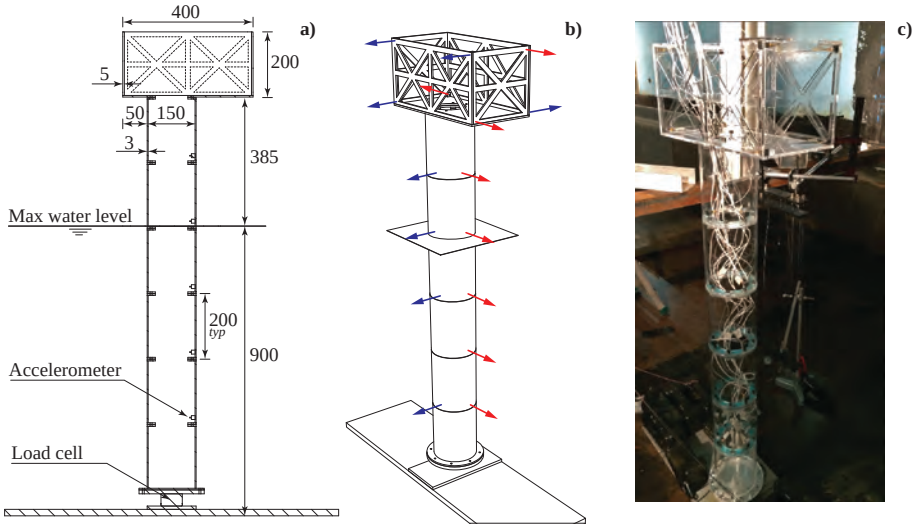

Figure 1: Experimental setup. a) shows the sideview cross section including the overall dimensions of the model, b) indicates the sensor position and direction, c) shows a picture from the test. Dimensions in mm.

The model is equipped with 16 uni-axial accelerometers; nine of which are positioned inside the pile and the remaining seven are distributed to the corners of the topside. The position and measuring direction are indicated in Figure 1 b). The accelerometers used are Brüel & Kjær type 4508-002 1000 mV/g and the sampling rate is 2 kHz.

The scope of the test is to monitor the structure during water filling of the flume and track the changes in modal parameters due to the influence of water. The test will begin at zero water level (referred to as dry state) and the water level will be increased to a maximum of 900 mm. Intermediate tests are conducted at 150 mm, 400 mm, 670 mm, 800 mm and 850 mm respectively. For each of these water levels, 3-4 individual tests are performed. The tests are conducted by introducing some random loading to the structure and record the response for approximately 300 seconds. The concepts of operational modal analysis are then applied on the response data from the accelerometers and modal parameters (natural frequencies, damping ratios and mode shapes) are extracted [6].

In order for OMA to be successfully applied, the loading of the structure should be approximately white noise i.e. random in time and space [6]. The excitation medium utilized in this case is a soft brush swept over the structure along with disturbance to the surrounding water. Additional instrumentation not relevant for the topic of this paper includes: ATI 6 DOF load cell, Wave gauges, 8 pcs kulite pressure transducers. These are installed for a later purpose in the test campaign.

3. ID algorithm

A total of 22 tests are conducted and though of different quality, each of these will yield an estimate on a number of modes. The frequency band of interest is 0 - 160 Hz as anything above this is too inflicted by noise and the sensor resolution not capable of spanning the modes shapes. Nine modes are identified in this frequency band and these nine modes will be examined in greater detail.

Now, several different identification methods are available both in the time domain and in the frequency domain. The identification algorithm selected is the Time Domain Poly Reference (TDPR) [7]. Although it was developed for impulse response functions, it can easily be adopted in OMA by using the correlation functions instead [8, 9]. Note that this section is not intended to go into details on the algorithm, however a brief overview of the method is outlined. For further details, the reader may find use of literature such as [6, 10].

Basically, the response data of the structure are used to calculate the correlation functions. The transposed correlation function matrix is then considered as free decays of the system and the concepts of the TDPR can be applied; A Hankel matrix is constructed and the polynomial coefficients are solved by a least square approach. Then, the coefficients are stored in a companion matrix and by making an eigenvalue decomposition, the modal parameters can be found.

Now, in order to get the best conditions for the modal identification, filtering and DOF condensation are applied as a pre-step to the TDPR. This is exercised in the frequency domain by reducing the number of DOFs and amplifying the remaining principal components. The details on condensation can be found in [11].

The data is examined by looking at one frequency band at a time. While moving the frequency band and shifting the model order in the TDPR, stable poles are extracted from the signal. Typically these are represented by stabilization diagrams, but in order to limit the data flow in the figures of this paper, only the single picked modes are shown.

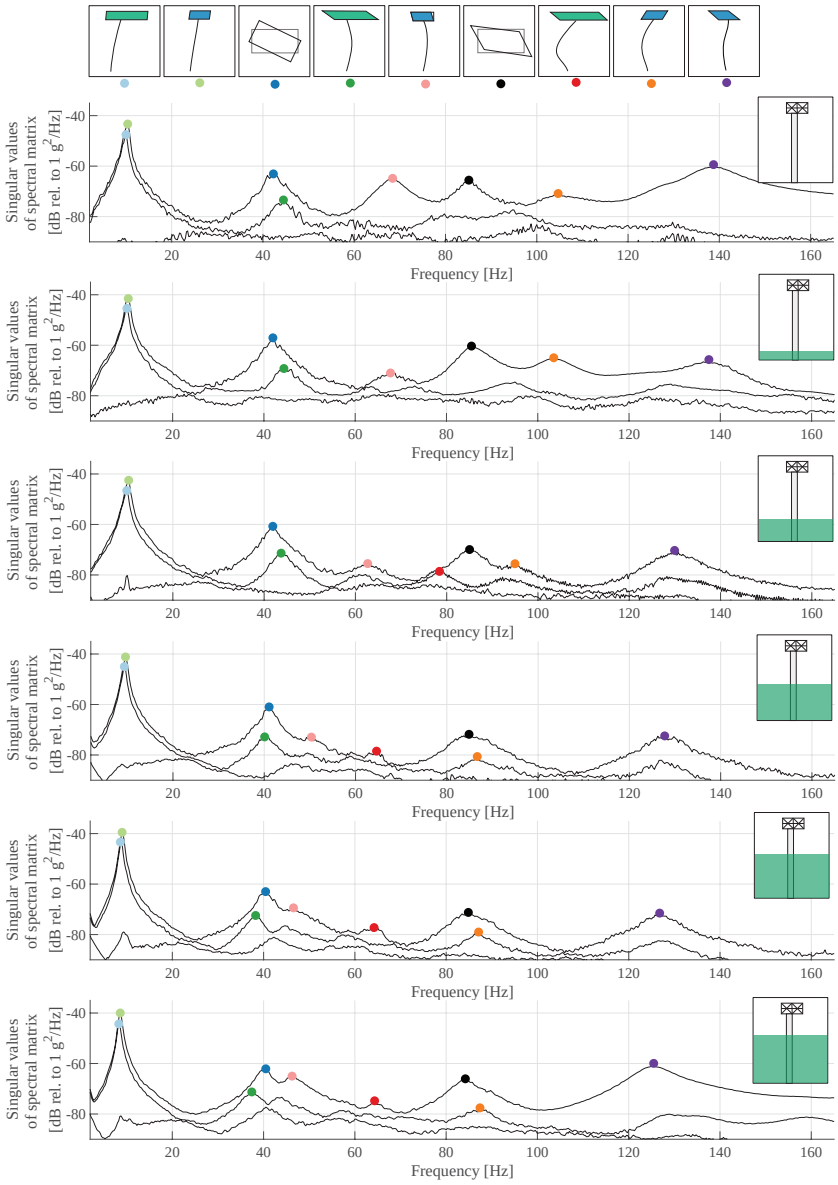

Figure 2: Singular values of the spectral density. The three first singular values are shown for different water levels. The water levels shown are 0, 150, 400, 670, 800 and 900 mm respectively. The different mode shapes identified are sketched in the top of the figure in ascending order and indicated by a coloured dot.

4. Modal parameter tracking

To give an indication of the quality of the data, a compilation of spectres are shown in Figure 2. The data series for each water level are merged into a single file and the spectra are averaged using the Welsh technique with a block size of 2^{13} samples corresponding to four seconds. A singular value decomposition of the spectral density is made and the figure shows the first three singular lines. The modes in Figure 2 are identified by peak picking and tracked by colour coding.

5. Results

For the seven different water levels ranging from 0 to 900 mm, modal identification is conducted using the TDPR technique outlined in Section 3. For each water level, 3-4 separate tests are made and the modal parameters are shown along with the average of the estimates. Figure 3 and Figure 4 show the identified modes in the frequency band of 0-160 Hz. The natural frequency, damping ratio and mode shape complexity are all given as a function of the water level. The individual mode shapes (1-9) are sketched in Figure 2 for reference.

The data in Figure 4 are merely the same as given in Figure 3, but normalized with respect to the average dry conditions to show the relative development in modal parameters. As seen in Figure 3 and 4, the scatter in the estimates are significantly higher on the damping ratios and complexity indicators than for the frequencies. This is not uncommon when engaging in modal analysis on experimental data (especially when dealing with closely spaced modes), yet it masks the conclusion on the fluid influence on these parameters - more about this in the following.

First, looking at the frequencies; it is seen that in general the natural frequencies drop with the increase in water level due to the hydrodynamic added mass. Yet, mode 3 and mode 6 are nearly

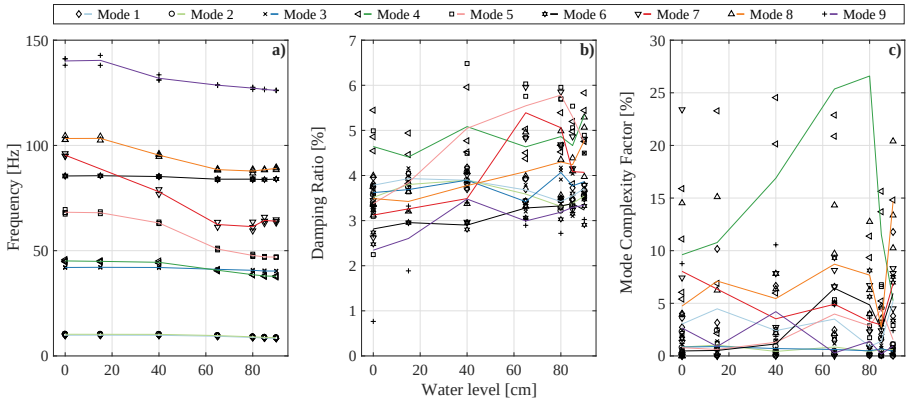

Figure 3: Estimated modal parameters at different water levels. Each mark represents an estimate from a data series and the solid lines are the water level averages. a) shows the development in natural frequency for each mode. b) shows the development in damping ratio for each mode. c) shows the development in mode shape complexity of each mode.

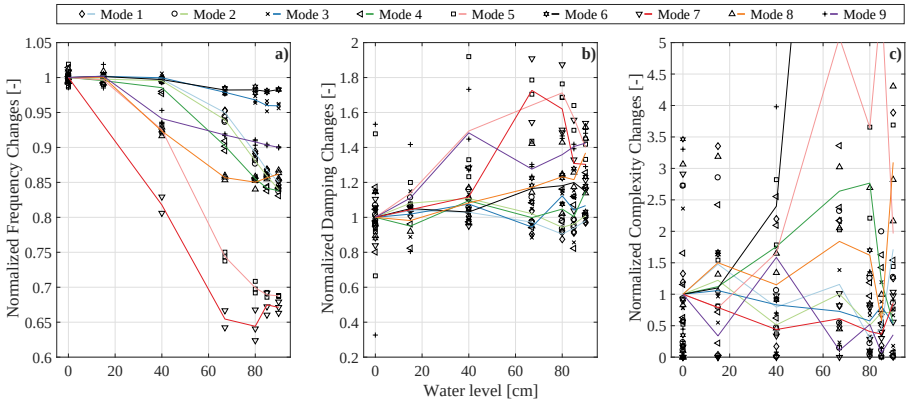

Figure 4: Relative changes in modal parameters due to shift in water level. Each mark represents an estimate from a data series and the solid lines are the water level averages and normalized with respect to the dry state. a) shows the relative development in natural frequency for each mode. b) shows the relative development in damping ratio for each mode. c) shows the relative development in mode shape complexity of each mode.

unaffected by the water. The mode shapes for these are characterized by predominant deformation to the topside and nearly no subsea deformation, see Figure 2. Literature such as [12, 13] states that one may encounter these effects when fluid-structure interaction is present. Since all modes, but the ones concerning only the topside, have a decrease in frequency, this yield an interesting phenomena as the modes start to cross each other by frequency. This is seen in Figure 3 a) at a water level of 670 mm for mode 3 and at a water level of 250 mm for mode 6.

Next looking at the damping estimates; the scatter from test to test is high compared to the average changes due to the influence of water. However, there is a tendency of an increase in damping for all modes. The higher modes (with exemption to mode 6) seems to be affected the most with respect to the damping with relative changes $> 30\,\%$ whereas the the changes on the first two bending modes and the two topside modes are less significant, see Figure 4 b).

Finally, the complexity of the mode shapes are shown in Figure 3 c) and Figure 4 c). The details on how the mode complexity factor is calculated is described in Section 6.1. In general there is a considerable level of complexity in the mode shapes ranging between 1 and up to 30 %. However, given the level of scatter in the estimates it is inconcludable whether the complexity originates from the influence of water or rather non-linearities in the model. The latter is anticipated to be the main reason for the complexity considering the number of structural joints, material selection etc.

6. Mode shape alteration

6.1. Complex mode shapes

When identifying mode shapes from experimental data, often the identified mode shapes tend to have a imaginary part. This may be due to ID algorithm, non-linearities or cases of non

proportional damping. The complex part is often considered as noise and disregarded, but it may indicate some physical properties of the system [14]. If the purpose of the modal analysis is to link the experimental mode shapes to ones obtained from an FE model, the most natural choice would be to disregard the imaginary part or use the absolute value.

Several different indicators can be used to quantify the complexity in a mode shape. For this case the mode complexity factor (MCF) will be utilized. The MCF is calculated for mode r as

$$\mathrm{MCF}_r = 1 - \frac{(S_{xx} - S_{yy})^2 + 4S_{xy}^2}{(S_{xx} + S_{yy}^2)} \tag{1}$$

where

$$S_{xx} = \Re\left(\underline{\phi_r}^T\right)\Re\left(\underline{\phi_r}\right) \qquad S_{yy} = \Im\left(\underline{\phi_r}^T\right)\Im\left(\underline{\phi_r}\right) \qquad S_{xy} = \Re\left(\underline{\psi_r}^T\right)\Im\left(\underline{\psi_r}\right) \tag{2}$$

Here, $\underline{\phi_r}$ is the mode shape vector for mode r while $\Re(\cdot)$ and $\Im(\cdot)$ extract the real and imaginary part reepectively. The MCF value is real and ranging between 0 and 1.

6.2. Mode shape

For complex modes, the MAC value between two mode shape vectors $\underline{\phi_a}$ and $\underline{\phi_b}$ can be calculated from [15, 16] as

$$\mathrm{MAC}(\underline{\phi_a},\ \underline{\phi_b}) = \frac{|\underline{\phi_a}^T\ \underline{\phi_b}^*|^2}{\left(\underline{\phi_a}^T\ \underline{\phi_a}^*\right)\left(\underline{\phi_b}^T\ \underline{\phi_b}^*\right)} \tag{3}$$

In order to quantify the changes in mode shapes the MAC value is calculated for every mode compared to a reference mode shape. The reference mode shape is the mode shape at dry state identified by the first test series - i.e. the first column in Figure 5. The MAC values depicted are hence the same mode for all successive tests compared to the reference test.

When modes are closely spaced in frequencies, their associated modes shapes may be rotated within the subspace spanned by the modes engaged [17]. For instance, this can be observed in the case of mode 3, 4 and 5 whose mode shapes start to mix at a water level of 670 mm, see Figure 3 a) or Figure 2. How much the mode shapes will blend among the conjointly modes depends on ID algorithm used and its fitting parameters. Surely it is more convenient if this rotation does not occur, but it does not pose a problem as they can be reorientated to fit the reference modes better. This is done by assuming a linear combination of the mode engaged and making a least square fit to the reference modes.

Test series 2, 6 and 17 showed poor results due to improper excitation. As a result of this, only the first 4 modes were extractable from the data, hence the missing bars in Figure 5. Although a true random excitation was attempted also mode 7 was not greatly engaged in several tests as seen from the spectra in Figure 2, this may be the reason for increased fluctuations in the estimates.

6.3. Mode shapes in details

In this section, a close-up on two selected mode shapes is presented. The mode shapes displayed are mode 7 and mode 9 which are highlighted by an asterisk (*) in Figure 5. The mode shapes have been normalized to a maximum deflection of 0.15 m i.e. 10 % of the total height of the model.

Note that the mode shapes presented by Figure 6 and 7 are shown by utilizing some assumptions on the behavior of the structure. By looking at Figure 7 a), it is clear that the nodal value for the 4th node from bottom is incorrect. Since no sensor is positioned at this node in this direction

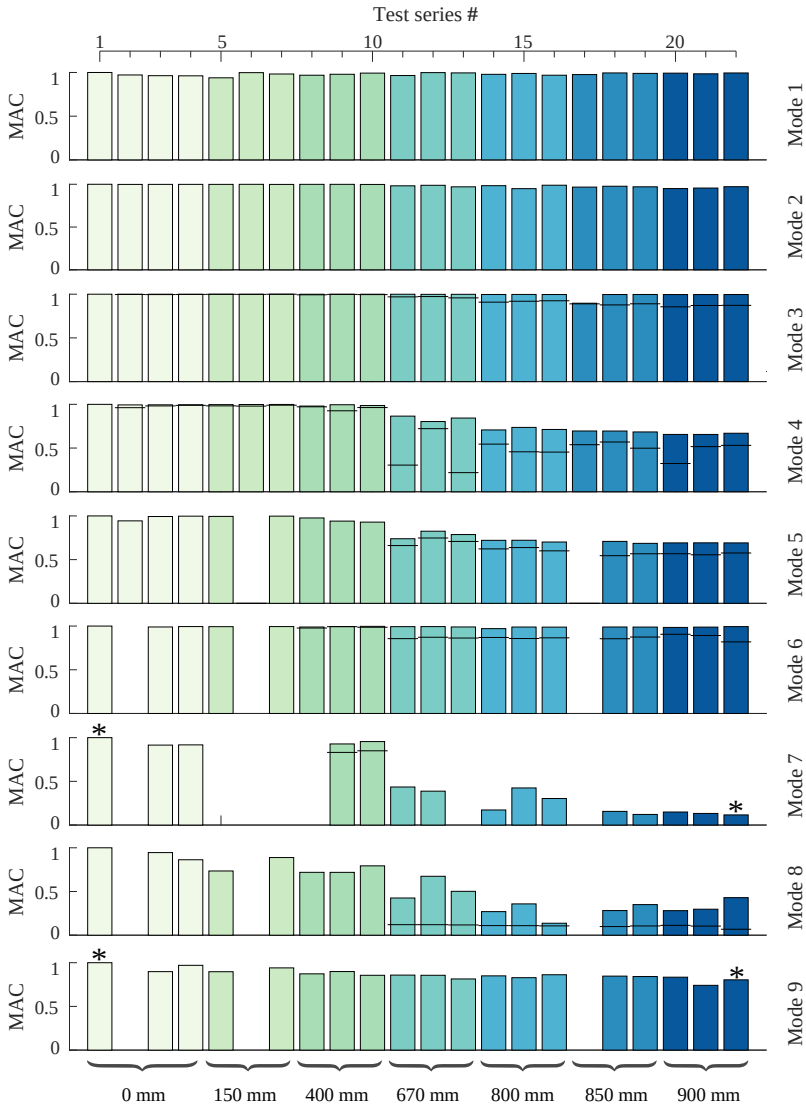

Figure 5: Modal assurance criterion (MAC). Every column corresponds to a test series while every row corresponds to a mode. The columns are grouped according to water level during the test. The black line splitting a single bar indicates the MAC value prior to rotating the mode shapes within their subspace. The four estimates marked by an asterisk (*) are shown in Figure 6 and Figure 7.

the nodal value depicted is simply an interpolation value between the adjacent nodes. These assumptions are just for visualization purposes and do not influence the MAC values presented earlier. Same applies to the topside.

Looking at these two modes shown by Figure 6 and Figure 7, the changes in mode shape are predominant subsea where the bending amplitude of the pile is reduced. The nodal point (zero vibration amplitude) for the pile is moved down for both cases.

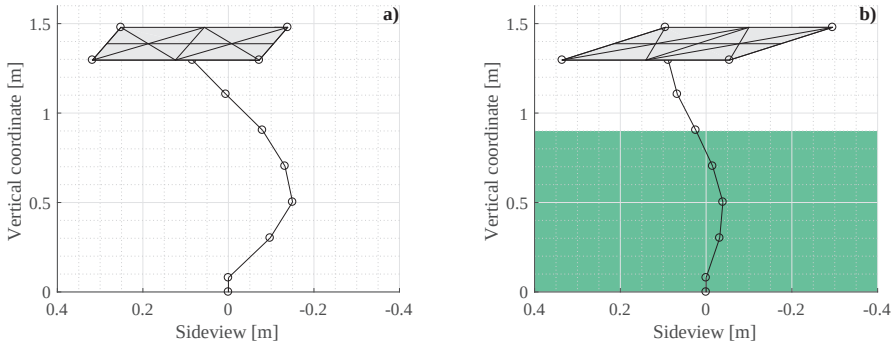

Figure 6: Mode shape 7 before and after water filling. MAC value between the two modes is 0.12.

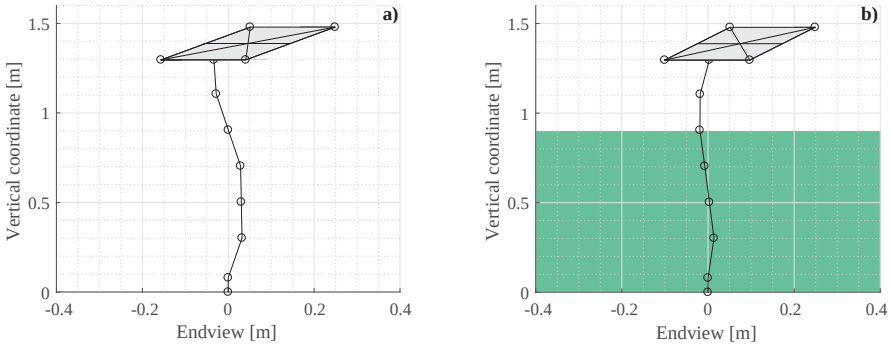

Figure 7: Mode shape 9 before and after water filling. MAC value between the two modes is 0.80.

7. Full scale perspective

The model considered in this paper is constituted as a hollow plexiglass model with a fairly large diameter to water depth ratio. This yields a large volume of water to be displaced by the structure and hence a large amount of added mass. Since the model itself is made from light weight material and air filled, the ratio of added mass versus the mass of the structure is also large. In the full scale perspective, the mass of the displaced water compared to the structural mass is likely to be a different ratio.

Now, if the structure is considered as an idealized SDOF system, the natural angular frequency is found as

$$\omega_{dry} = \sqrt{\frac{K_{dry}}{M_{dry}}} \tag{4}$$

where the K_{dry} is the generalized stiffness of the structure and M_{dry} is the generalized mass both at a dry state for a mode of vibration. If it is assumed that the stiffness of the structure is unchanged by the presence of water, the equation for the wet conditions becomes:

$$\omega_{wet} = \sqrt{\frac{K_{wet}}{M_{wet}}} = \sqrt{\frac{K_{dry}}{M_{dry} + M_{added}}} \tag{5}$$

Here, M_{added} symbolizes the added mass from the fluid-structure interaction [2, 4, 13]. Now, this is strictly only valid if the mode shape of interest is unchanged by the influence of water. This is a fair assumption for the first few modes in this case, see Figure 5. The change in frequency from the influence of water is hence seen as

$$\frac{\omega_{wet}}{\omega_{dry}} = \frac{1}{\sqrt{\left(1 + \frac{M_{added}}{M_{dry}}\right)}} \tag{6}$$

From equation (6) it is evident that the change in frequency depends on the ratio between the mass of the structure and the added mass from the fluid. Since the cross section of the model in this case is circular, there is no cross coupling and the added mass is somewhat proportional to the mass of the fluid displaced by the structure: $M_{added} \propto V, \rho_w$, where V is the displaced volume and ρ_w is the fluid density. However other aspects such as boundary conditions for the fluid, viscosity, vibration amplitude and frequency can also influence the effect of added mass [13, 18]. Since the fluid density in this scaled experiment is larger than in full scale the effect from the fluid- structure interaction is amplified. This means that the relative changes in modal parameters shown by Figure 3 and Figure 4 may be less for the full scale scenario.

The model considered in this paper is dry on the inside (concerning the sensors). Offshore mono tower structures may be constructed as dry or wet on the inside where the latter is the most common. Water inside the structure will yield a different alteration of the structure as the internal water will further increase the added mass. This effect is not studied additionally but is worth mentioning.

8. Conclusion

This paper has outlined the changes in modal parameters from the influence of surrounding water on a small scale model. The model is a bottom fixed, surface piercing mono tower made from

plexiglass. It was through operational modal analysis demonstrated how the modal parameters changes by the presence of water. Most significant finding was that the order of the modes were changing as the flume was filled with water. This was due to the nature of the individual mode shapes; mode shapes, where deflection is predominant ascribed to rotation and not bending of the tower will yield little or no changes from the water whereas especially higher order bending of the tower will experience great influence from the added mass. If modes are closely spaced this may cause them to change order.

Damping estimates were examined and found to increase with water level as expected. For semi-submerged structures, where fluid-structure interaction is present, it might be expected that non-proportional damping could cause the mode shapes to become complex. However it was not possible to show a decisive relation for this due to the scatter in the estimates. The mode shapes, however, were examined in details and it was seen that especially for higher modes; the deflection subsea were reduced.

The development in modal parameters are based on averages from different tests, where it was assumed that the water yields a constant alteration of the modal parameters. The conclusions from this study are hence based on small vibration amplitudes as different levels of excitation force is not examined.

8.1. Further work

As mentioned by the introduction, the work shown in this paper will be the basis for a successive study in indirect load estimation. The knowledge gained will feed the updating process of a finite element model needed for the dynamic analysis of wave action.

Acknowledgements

The authors acknowledge the funding received from the Centre for Oil and Gas – DTU/Danish Hydrocarbon Research and Technology Centre (DHRTC). Also assistance from the staff at Luminy University, Marseille, during the experimental campaign needs to be acknowledged.

References

[1] U. Tygesen, K. Worden, T. Rogers, G. Manson, E. J. Cross, State-of-the-art and future directions for predictive modelling of offshore structure dynamics using machine learning, Proceedings of the International Modal Analysis Conference, IMAC (2018b).

[2] M. Maheri, R. Severn, Experimental added-mass in modal vibration of cylindrical structures, Engineering Structures 14 (3) (1992) 163 – 175.

[3] M. Rahman, D. Bhatta, Evaluation of added mass and damping coefficient of an oscillating circular cylinder, Applied Mathematical Modelling 17 (1993) 70–79.

[4] V. Vu, M. Thomas, A. Lakis, L. Marcouiller, Effect of added mass on submerged vibrated plates, 25th Seminar on machinery vibration, Canadian Machinery Vibration Association (2007).

[5] R. Han, H. Xu, A simpled and accurate added mass model for hydrodynamic fluid-structure interaction analysis, Journal of the Franklin Institute, Volume 333, Issue 6 (1996).

[6] R. Brincker, C. Ventura, Introduction to Operational Modal Analysis, John Wiley and Sons, Ltd, Chichester, West Sussex, UK, 2015.

[7] H. Vold, J. Knudrat, G. Rocklin, R. Russell, A multi-input modal estimation algorithm for mini-computers, SAE International Congress and Exposition Technical Paper 820194 (1982).

[8] G. C. James, T. G. Carne, J. P. Lauffer, The natural excitation technique (NExT) for modal parameter extraction, The International Journal of Analytical and Experimental Modal Analysis 10 (4) (1995) 260–277.

[9] R. Brincker, On the application of correlation function matrices in OMA, Mechanical Systems and Signal Processing 87 (2017) 17–22.
[10] A. Harvey, Time series models, Phillip Allan Publisher Ltd, 1981.
[11] P. Olsen, M. Juul, R. Brincker, Condensation of the correlation functions in modal testing, Submitted to Mechanical Systems and Signal Processing (2017).
[12] N. Barltrop, A. Adams, Dynamics of fixed marine structures, 3rd Edition, Butterworth-Heinemann, UK, 1991.
[13] B. Blevins, Formulas for natural frequency and mode shape, Krieger Publishing Company, Malabar, Florida, USA, 1984.
[14] M. Imregun, D. Ewins, Complex modes - origins and limits, Proceedings of the International Modal Analysis Conference, IMAC 1 (1995) 496 – 506.
[15] R. Allemang, The modal assurance criterion (MAC): Twenty years of use and abuse, Journal of Sound and Vibration 37 (2003) 14–23.
[16] M. Pastor, M. Binda, T. Harcarik, Modal assurance criterion, Procedia Engineering 48 (2012).
[17] P. Avitabile, Modal space - back to basics, Society of experimental mechanics Journal compilation December (2007) 1–2.
[18] S. Chakrabarti, Offshore structure modeling, Advanced series on ocean engineering, Vol. 9, World Scientific Publishing Co. Pte. Ltd., 1994.

Chapter 11

Wave loading using frequency domain identification

Paper V

"Indirect wave load estimates using operational modal analysis"

Michael Vigsø, Julie Kristoffersen, Rune Brincker and Christos Georgakis

Published in Proceedings of the 28th International Ocean and Polar Engineering Conference, ISOPE, Sapporo, 2018 (Peer reviewed)

This chapter presents a study of regular wave loading on a highly flexible cantilever structure. The load identification is performed in the frequency domain. The author has performed the main part of the ideation, experiments, analysis and the writing of the paper. Julie Kristoffersen took part in planning and conducting the experiments. The paper has been formatted with minor grammatical adjustments to suit this thesis.

Indirect wave load estimates using operational modal analysis – Preliminary findings

Michael Vigsø[a,*], Julie Kristoffersen[a], Rune Brincker[b], Christos Georgakis[a]

[a] *Aarhus University, Inge Lehmanns Gade 10, 8000 Aarhus, Denmark*
[b] *Technical University of Denmark, Brovej 118, 2800 Kgs. Lyngby, Denmark*

Abstract

Wave loading on offshore structures has proven difficult to quantify through direct full-scale measurements. Therefore, engineers rely on codes and guidelines, numerical simulations, and scaled experiments in the design and as-built evaluation process. In this paper, it is shown that by monitoring the response of the structure and utilizing Operational Modal Analysis (OMA) it is possible to indirectly identify loads, occurring in actual conditions. A method employing modal parameters to establish a response function, which is used to back-calculate the hydrodynamic wave loading of a structure is presented. The process of inverting the system matrices is stabilized by merging the model with linear wave theory and hence constraining the solution to a scaling function of a predefined load distribution. The method is validated through a numerical case study and by wave flume experiments. Both cases are constituted as two-dimensional loading on a semi submerged cantilever cylinder.

Keywords: Wave loading, Indirect measurements, Operational modal analysis, Offshore structures

1. Introduction

In recent years concerning footage from the North Sea have been fuelling an intensive investigation lead by Mærsk. The recordings show plunging breaking waves at the Tyra field in close proximity to the offshore structures [1]. It was estimated that the wave heights were exceeding the 10 000 year return period for abnormal wave design. Questions have been raised whether the load effect of these extreme waves will compromise the reliability of the structures at sea.

Although much research has been done in the field of abnormal and breaking waves, it is evident that more research is needed in the field of extreme wave loading to offshore structures. Some issues remain elusive as most methods are based on scaled laboratory experiments. When conducting wave lab experiments, scaling effects will inevitable be present and especially in the case of breaking waves [2].

A new approach - not subjected to scaling limitations for wave load quantification - is presented in this study. By monitoring the response of an offshore structure, the structure itself can be used as

*Corresponding author
Email addresses: mvigso@eng.au.dk (Michael Vigsø), jck@eng.au.dk (Julie Kristoffersen), runeb@byg.dtu.dk (Rune Brincker), cg@eng.au.dk (Christos Georgakis)

Published in the Proceedings of the International Ocean and Polar Engineering Conference, ISOPE
This paper has been formatted to suit this thesis *June 2018*

a live full scale load cell. This is done by inverse computations from the response of the structure. Limited research has been done specific to this application [3, 4], whereas more focus has been given to indirect methods of e.g. fatigue assessment of offshore structures [5, 6]. The indirect load identification of the wave action is a challenging discipline to verify, which may be the reason why little work has been done on this in the past. Input estimation in general is not a new topic as people have worked with this for many years.

In the late 80's Karl Stevens wrote an excellent overview on the topic of indirect load identification [7]. The paper outlines the challenges associated with this field of research, but also its potential. Many different approaches have since been tried out within the field of input identification. Most of the work done in this context are based on cases where the input is well defined and hence capable of verifying the results - either by using impact hammers or by simulation e.g. [8–10]. In resent years input identification using Kalman filters has proven successful [11–15].

In this paper, Operational Modal Analysis (OMA) will be used as a tool for modal identification of the structures in as-build conditions. The result from the OMA is used to make a model representation and this will be the key in deciphering the vibrations of the structure and hence estimate the wave loading.

The mathematical notation used is denoting matrices by a double underline and vectors by a single underline. Superscript* is a complex conjugate and superscript^T is a transposing operation.

2. Theory

The response of a linear dynamic system, $\underline{y}(t)$, is defined as the convolution integral between the impulse response function, $\underline{\underline{h}}(t)$ and the a time varying load. [16]. The principle of load identification is to measure the response and then de-convolute this expression.

$$\underline{y}(t) = \underline{\underline{h}}(t) \circledast \underline{f}(t) \triangleq \int_{-\infty}^{\infty} \underline{\underline{h}}(\tau)\, \underline{f}(t-\tau)\, \mathrm{d}\tau \tag{1}$$

This integral is more conveniently evaluated in the frequency domain, so by means of the Fourier transformation Eq. (1) becomes:

$$\underline{Y}(\omega) = \underline{\underline{H}}(\omega)\, \underline{F}(\omega) \tag{2}$$

here, $\underline{Y}(\omega)$ and $\underline{F}(\omega)$ contain the Fourier coefficients of the response- and load vectors respectively. $\underline{\underline{H}}(\omega)$ is referred to as the Frequency Response Function (FRF). The FRF matrix can be constructed from either mass-, damping- and stiffness matrices or from modal parameters, which will be the case for this paper.

$$\underline{\underline{H}}(\omega) = \sum_{r=1}^{N} \left(\frac{Q_r\, \underline{\psi_r}\, \underline{\psi_r}^T}{i\omega - \lambda_r} + \frac{Q_r^*\, \underline{\psi_r^*}\, \underline{\psi_r^*}^T}{i\omega - \lambda_r^*} \right) \tag{3}$$

where, $\underline{\psi_r}$ is the mode shape vector for mode r. Q_r is a mode shape scaling constant and λ_r is the complex pole. The parameters needed for the FRF matrix - mode shapes and poles - can be experimentally determined by utilizing the concepts of operational modal analysis. [17]. This is done by monitoring the response caused from what may be assumed as random excitation. For instance, in the context of offshore structures: small crested random waves and a light breeze

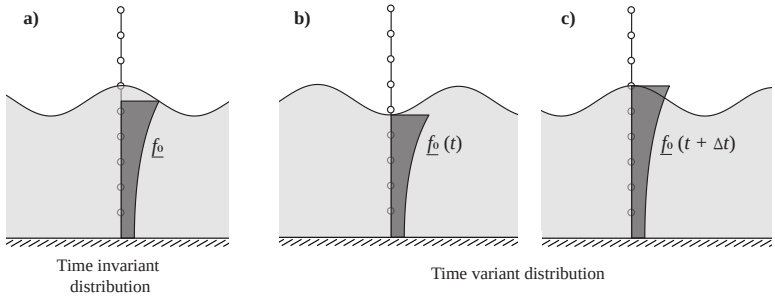

Figure 1: Principle of spatial distributions, $\underline{f}_0$.

touching the topside. The ID algorithm of choice can be applied and the modal parameters can be extracted from the signal. Both time- and frequency domain techniques exists for this.

Once the FRF matrix is estimated and the response of the structure, $\underline{Y}(\omega)$, is measured, the load can be calculated. This yields a type of inverse computation, where the load indirectly can be determined from measuring the response. Although it seems simple, problems persist as Eq. (2) is sensitive to truncation errors so when inverting the FRF matrix, the load estimate quickly becomes erroneous and may appear as non-physical.

As it was demonstrated by Vigsø et al. [18] - if the load distribution is known this can be utilized to constrain the solution and hence improve the load estimate. This is implemented by separating the load variable from Eq. (1), into a spatial distribution, $\underline{f}_0$, and scaling function, $g(t)$:

$$\underline{f}(t) = \underline{f}_0\, g(t) \tag{4}$$

when inserting this definition into Eq. (2) we have

$$\begin{aligned} \underline{Y}(\omega) &= \underline{\underline{H}}(\omega)\, \underline{F}(\omega) \\ &= \underline{\underline{H}}(\omega)\, \underline{f}_0\, G(\omega) \\ &= \underline{C}(\omega)\, G(\omega) \end{aligned} \tag{5}$$

here, $\underline{C}(\omega)$ is the matrix product of the FRF matrix and the spatial distribution. The scaling function can now be estimated by a pseudo inverse operation.

$$\hat{G}(\omega) = \underline{C}^{\dagger}(\omega)\, \underline{Y}(\omega) \tag{6}$$

The final load estimate is then found by an inverse Fourier transformation and back substitution into Eq. (4). In order to do this, the spatial distribution, $\underline{f}_0$, must be known.

In order to apply this in the context of wave loading of an offshore structure it may be assumed that the structural loading is solely caused by water waves. Figure 1 shows the principle of how the spatial distribution can be defined.

If the wave height is not recorded, the spatial distribution may be assumed as time invariant - for instance varying between the seabed and the mean water level as indicated by Figure 1 **a)**.

On the other hand - if the surface elevation is recorded simultaneously as the response of the structure, this additional information can be incorporated in the calculations, Figure 1 **b)** and **c)**. For instance, taking the same distribution as in **a)** and stretching it to follow the surface elevation near the structure and hence assuming that the loading will occur at the entire wetted area.

When the spatial distribution of the load is changing in time (case **b)** and **c)**), the procedure for solving the scaling function changes. That is due to the convolution theorem which states that a product in the time domain is a convolution in the frequency domain and vice versa. If we apply the time variant definition of the spatial distribution, Eq. (2) becomes

$$\begin{aligned} \underline{Y}(\omega) &= \underline{\underline{H}}(\omega)\, \underline{F}(\omega) \\ &= \underline{\underline{H}}(\omega)\, \big(\underline{f_0}(\omega) \circledast G(\omega)\big) \qquad (7) \\ &= \underline{\underline{H}}(\omega) \int_{-\infty}^{\infty} \underline{f_0}(\xi)\, G(\omega - \xi)\, \mathrm{d}\xi \qquad (8) \end{aligned}$$

here, ξ is the frequency lag. As seen in the equation; when $\underline{f_0}(t)$ is a time variant function this yields a more complex problem to be solved. If the frequency content of the load is known this can be included else wise the equation can be solved through iteration.

3. Simulation

This simulation case study will demonstrate, that by monitoring the response of an offshore structure and applying the procedure described above, it is possible to indirectly estimate the wave load. A plane semi-submerged cantilever structure exposed to non-breaking waves will be the scope of this demonstration. The benefits of a simulation is that the method can be evaluated with as much noise as desired and the result can be compared to the precise input and hence indicate how sensitive the solution is to different assumptions and sources of error.

The simulation is conducted as a plane scenario using an finite element (FE) cantilever beam model. The wave loading is evaluated using linear theory and Wheeler stretching to account for fluid motion above mean water level [19]. Although fluid surrounding a structure is known to retard

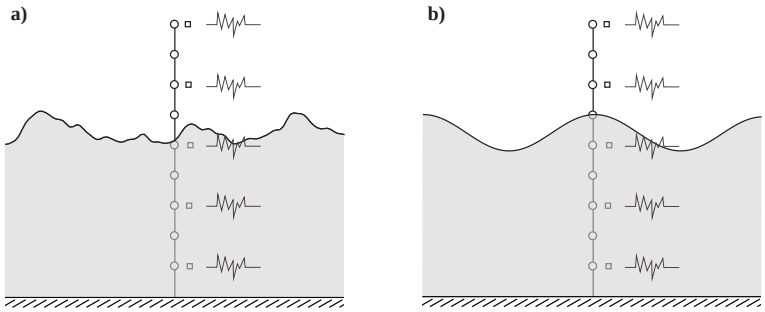

Figure 2: Simulation sea states.

the response by added mass and damping, for this simulation, it is assumed that no interaction between the fluid and structure is present. The drag- and added mass coefficients are set to 1.3 and 1.9 respectively and the loads are evaluated using the Morison equation [20]. (The coefficients are assumed to be unknown in the successive load identification). The geometrical quantities and hydrodynamic properties are selected to resemble the physical experiment covered by this paper (water depth 0.9 m, structure diameter 50 mm).

The simulation will be divided into two parts: 1): A simulation of the system response caused by a series of random waves. This shall be the basis for the OMA analysis and hence provide estimated modal parameters needed for the successive analysis of the wave loads. The random waves are synthesized from a Pierson–Moskowitz spectra with a peak frequency of 0.5 Hz and a significant wave height of 0.2 m.

2): Next a series with regular waves is simulated and shall be the basis for the indirect load identification calculations. A wave height of 0.2 m and period of 2 s is chosen as the sea state for the simulation. This gives a relative wave height of $H/h = 0.22$ and a wave steepness of $H/L = 0.04$. The two different simulation cases are shown by Figure 2, where a set of five FE-DOFs are chosen as sensor information and only the response from these are kept for the analysis. The sensors in Figure 2 are indicated by squares (□). For both of the simulation cases, a noise level of 150 dBW is added to the recorded signal.

Modal identification from random waves

The frequency domain response from 180 seconds of random wave simulation can be seen in Figure 3 in terms of singular values [17]. Despite the loading not being perfect white noise, four modes are revealed in the signal within the frequency band of 0-300 Hz. The modes are peak picked and analysed using the Frequency Domain Decomposition method [21]. The damping estimates are found by applying the Eigensystem Realization Algorithm [22] at a band passed signal near the resonance frequencies. The modal parameters are listed in Table 1. Since no fluid/structure interaction is considered, the estimated modal parameters shall resemble the FE model with deviation only caused by noise and statistical error. The 4th mode shape from the FE model is an axial deformation mode and since only horizontal sensor information is available for the OMA, this mode cannot be estimated from the signal.

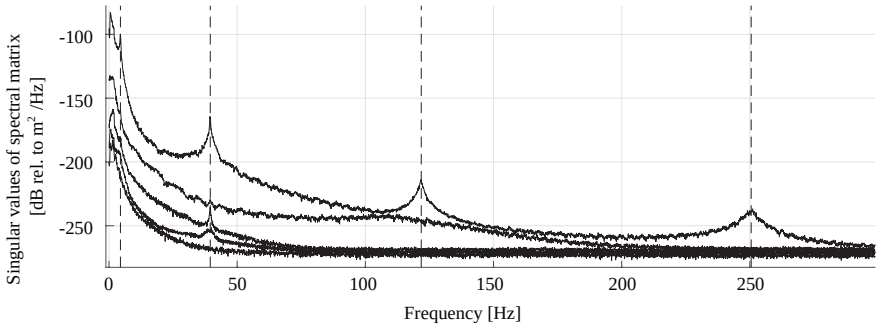

Figure 3: Singular value decomposition of the response spectral density. Data composed using Welch averaging.

Table 1: Modal parameters from simulation case study.

FE model					
Mode	1	2	3	4	5
Natural Frequency, ω [Hz]	4.47	39.5	121	180	250
Damping Ratio, ζ [%]	1.80	0.33	0.45	0.61	0.82
OMA estimates					
Mode	1	2	3	4	5
Natural Frequency, ω [Hz]	4.46	39.5	122		251
Damping Ratio, ζ [%]	2.07	0.31	0.44		0.82

Assuming that the structural properties, geometry and material, are known quantities for the offshore structure. These can be used to make a new FE model to aid in the mass normalization of the OMA mode shapes. This FE model can also be used for mode shape expansion [23] in order to obtain a higher resolution near the splash zone as desired. Now, the obtained modal parameters can be used to establish the frequency response function for the structure at actual in-place conditions, Eq. (3).

Load identification

The response due to regular wave loading is seen in Figure 4. The response of the structure will be truncated in terms of the sensor position and noise level though still be of value for the load identification.

Before making the final load identification calculation, the spatial distribution must be revisited. As the assumed load distribution is of great importance for the quality of the load estimate this must be selected with care. In principle any reasonable distribution can be used and for this study, two different distributions will be tried out. They are shown by Figure 5. Distribution **a)** is generated from linear wave theory by assuming velocity squared proportionality at $\mathrm{d}u(z,t)/\mathrm{d}t = 0$. Distribution **b)** is likewise generated from linear wave theory but from an acceleration proportional

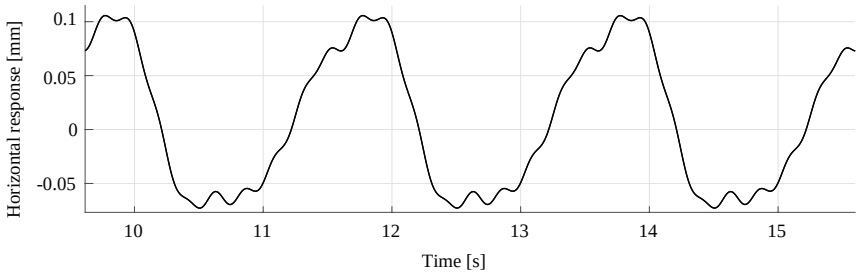

Figure 4: Steady state response from top sensor when subjected to regular wave loading.

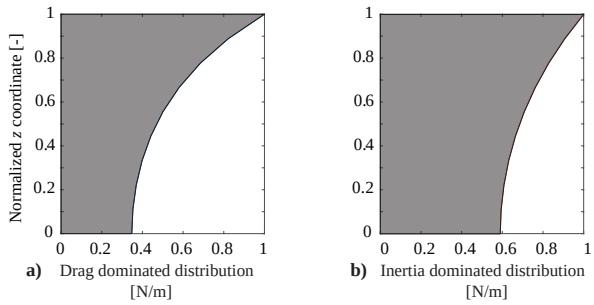

Figure 5: Load distributions. **a)** Drag dominated is proportional to velocity squared. **b)** Inertia dominated is proportional to acceleration.

assumption at $u(z,t) = 0$. Information regarding water depth, wave height and period are of course needed to derive these. The normalized z coordinate is 0 at the seabed and 1 at the water surface. Both the distributions are normalized with a maximum value of 1 N/m. Neither of these will perfectly describe the actual loading used in the simulation, however it is demonstrated that they yield a reasonable approximation.

Figure 6 shows the final load estimate for both the time variant and time invariant approach - recall their definitions from Figure 1. The figure shows the total load applied to the structure from the wave action. As a general observation, for this type of cantilever structure, the assumed point of attack for the load distribution is governing for the load estimate. When the point of attack is assumed to be lower than the real, this will result in a over estimated load and vice versa. Hence the two time variant distributions (drag- or inertia dominated) will yield an absolute lower and upper bound for the estimate respectively and the span between should be considered as the

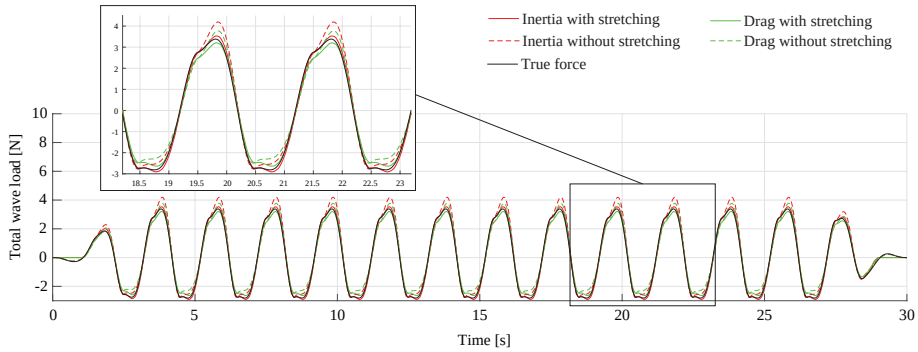

Figure 6: Wave load estimate from the simulation case study. Both the time variant (with stretching) and time invariant (without stretching) solution are shown and compared to the actual input force in the simulation. The windowing is added during post processing.

uncertainty of the estimate.

If the surface elevation is not recorded - hence the distribution is described as time invariant - this yields an offset in the load estimate as the point of attack at some instances of time will be too low and at some instances too high. As seen from the estimates, the two solutions using stretching of the load distribution, yield a better estimate, than the time invariant distribution. It is expected that the deviation between the two methods will increase with the wave height.

Experiment

An experimental campaign has been conducted in a wave flume at Newcastle University, UK 2016 [24]. A cantilever beam made from plexiglass is used for the experiment. The model is equipped with 7 uni-axial accelerometers; 6 positioned in the the wave direction and one in the transverse direction. Accelerometers used are Brüel & Kjær type 4508-B 100 mV/g. Three wave gauges are positioned in line with the model and an average of these are used as a basis for the surface elevation, $\eta(t)$. The model and the sensor layout is sketched in Figure 7.

The model is resting on a 6 DOF ATI load cell which is used to record the all the mudline forces. The mean water level of the flume is 0.9 m and the plexiglass model has a diameter of Ø50 mm. The total height of the model is 1.35 m.

Modal identification

As for the simulation case study; the model is observed at two stages, 1): Recording the response due to random excitation - the excitation is caused by making some random disturbance to the water surface surrounding the model. Again the concepts of OMA are deployed and mode shapes and damping estimates of the structure are obtained. For the frequency band of 0-100 Hz four in-plane bending modes were identified. Their frequency and damping ratio are listed in Table 2. The ID algorithm used is the same as for the simulation case study.

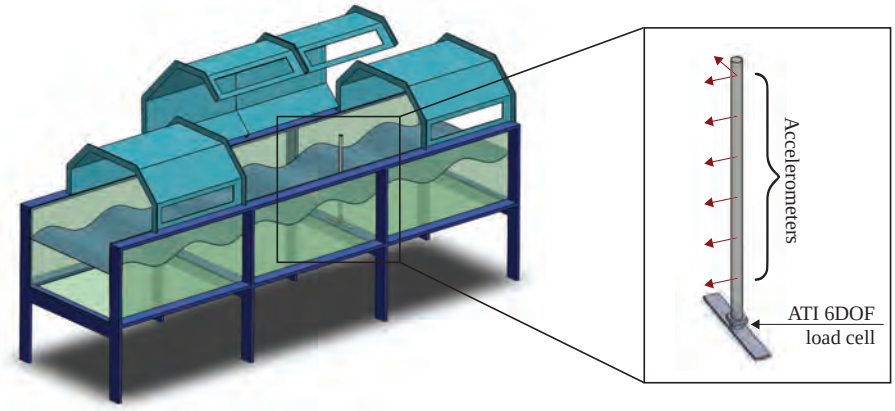

Figure 7: Experimental setup.

Disregarding the complex part of the mode shapes, an FE model is made and updated with focus on mode shape correlation and frequency match. The model is made using beam elements with 6 degrees of freedom (DOF) at each node. The influence of water is included as added mass below the mean water level. As a simplification; proportional damping is assumed and coefficients adjusted for a best fit. The FE model is used for mode shape expansion and mass normalization of the experimentally obtained mode shapes from the OMA analysis.

A frequency response function (FRF) of the system can yet again be formulated using Eq. (3). Obviously when using expanded mode shapes to construct the FRF matrix, the matrix will suffer from rank deficiency as no new modes are added. However, when the estimate is afterwards constrained by the assumed load distribution and solved by the pseudo inverse operation, this stabilizes the result.

Table 2: Modal parameters from experimental case study. (In-plane modes only).

OMA estimates				
Mode	1	2	3	4
Natural Frequency, ω [Hz]	2.12	13.4	44.5	97.7
Damping Ratio, ζ [%]	2.0	4.2	3.6	2.1

Load identification

2): Next step is to generate a wave configuration which can be used for the load computations. For this, a series of regular waves is chosen and the structural response is recorded. The waves are synthesized as linear waves with a period of 1.43 s and a wave height of 114 mm. These yield a relative wave height of $H/h = 0.127$ and a wave steepness of $H/L = 0.038$. The recording is initiated once the wave maker has reached a steady state output. As for the simulation case study; a set of two spatial distributions is used for the estimates. The distributions are generated in the same manner by assuming acceleration- or velocity proportionality and using linear wave theory. Only the solution using the time variant approach will be shown, i.e. utilizing the readings from

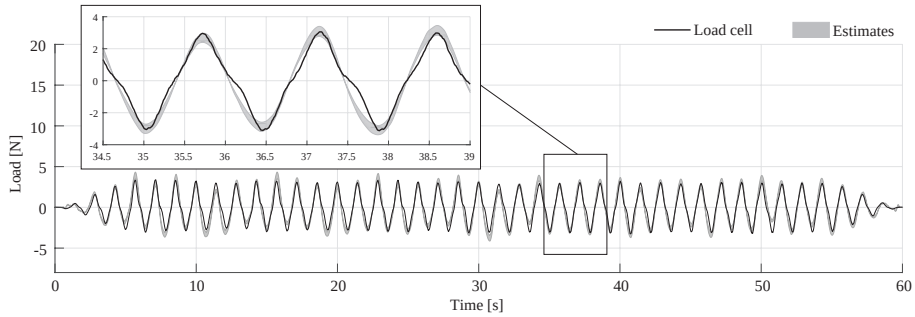

Figure 8: Estimated total wave load from physical experiment. The shear force measured by the load cell is shown for reference. The windowing is added during post processing.

the wave gauges and hence stretching the assumed load distribution to always cover the wet surface of the pile.

The solution on the load estimate can be seen in Figure 8. The estimate is shown as an interval between the drag dominated and the inertia dominated distribution. From the same reasoning as mentioned earlier: the absolute lower bound is the drag dominated result and the absolute upper bound is the inertia result. In principle, now the wave load has been indirectly determined from the response. However, since the structure at hand has some dynamic properties, which yields a dynamic amplification to the wave loading, it is not possible to directly measure the wave load at the load cell and hence verify the estimates. The estimated load from Figure 8 must then be transformed to reaction forces in order for a direct comparison to be made. Although accumulated uncertainty is present, this can be done by solving the unconstrained system of motion in Eq. (9), where the three response vectors are synthesized using the estimated load from Figure 8 along with the mass, damping and stiffness matrices from the updated FE model.

$$\underline{\underline{M}}\,\underline{\ddot{y}}(t) + \underline{\underline{C}}\,\underline{\dot{y}}(t) + \underline{\underline{K}}\,\underline{y}(t) = \underline{f}(t) \tag{9}$$

here, $\underline{y}(t)$ is the nodal displacement, $\underline{\dot{y}}(t)$ is the nodal velocity and $\underline{\ddot{y}}(t)$ is the nodal acceleration. The results of the estimated mudline forces (including dynamic amplification) are shown in Figure 9 and Figure 10 along with the readings from the load cell. The measurements from the load cell are affiliated by a severe degree of noise from 50 Hz. Thus the measured values shown by Figures 8 to 10 have been low-pass filtered at 40 Hz.

In terms of peak values for each passing wave, the estimated value of the force and moment is fairly good. Especially for the drag dominated end of the range. When it comes to variations between the peaks, the FE model is not capable in predicting the load variation and the estimate deviates more. This is naturally enough as the peak values of the load are the most governing for the response and as the response is the basis for the load estimate; the estimated load should have a best fit towards the peak values. The maximum and minimum forces and moments for each passing wave are plotted in Figure 11. Figure 11 **a)** shows the maximum negative forces i.e. caused during wave trough and Figure 11 **b)** shows the maximum positive forces i.e. caused during wave crest. The mean value and standard deviations are given by Table 3.

From Figure 11, linear wave theory adjusted by stretching of the profile seems to yield a too low point of attack - especially for the positive forces as indicated by Figure 11 **b)**. As a result of that, the mean value of the estimated bending moments is in good agreement with the measurements, whereas the force is overestimated. The increase in standard deviation in the estimated values are suspected to originate from integration error and noise in the response measurements.

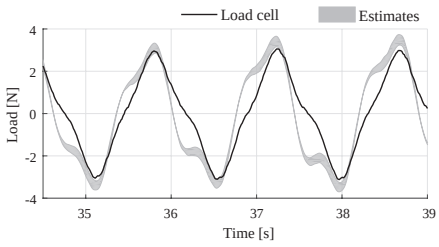

Figure 9: Estimated dynamic reaction forces, shear.

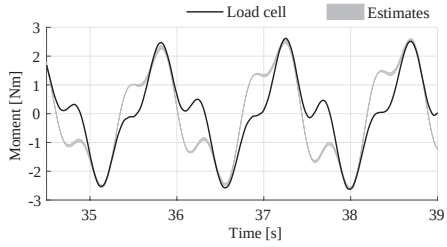

Figure 10: Estimated dynamic reaction forces, moment.

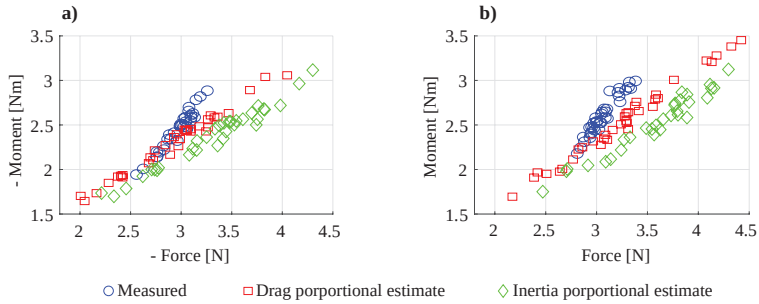

Figure 11: Maximum mudline forces for each passing wave. Average relative wave height $H/h = 0.127$ and average wave steepness $H/L = 0.038$.

Table 3: Mean and standard deviation of the maximum loads, i.e. from Figure 11 **a)** and **b)**.

	Moment [Nm]		Force [N]		Moment [Nm]		Force [N]	
	μ	σ	μ	σ	μ	σ	μ	σ
Measured	-2.44	0.22	-2.98	0.16	2.60	0.22	3.07	0.15
Drag proportional estimate	-2.31	0.53	-2.94	0.49	2.54	0.44	3.26	0.55
Inertia proportional estimate	-2.39	0.36	-3.36	0.56	2.65	0.45	3.76	0.62
	Loads during wave trough				Loads during wave crest			

4. Conclusion

It has been demonstrated that operational modal analysis can be used for indirect load quantification for offshore structures. For the analyses presented, it has been assumed that the only loading to the structure is originated from wave action. If several other contributions are present this complicates the procedure. The paper also demonstrates that by merging different sensor information (accelerations and wave gauges/LIDAR) this can be incorporated in the load estimate. The method is not subjected to scaling issues and can be applied on a full scale if the response of the structure is successfully recorded and a well updated FE model is available.

Although the structures considered by this paper are based on a simple static systems, nothing dictates that the method cannot be applied on more complex systems as long as there are sufficient sensors to describe the additional mode shapes.

5. Future work

Although the results presented by this paper are promising, they are based on a single structural system and one directional regular waves only. More research is needed in order to verify this method in cases where multi directional- irregular and even breaking waves are present.

Acknowledgements

The authors acknowledge the funding received from the Centre for Oil and Gas – DTU/Danish Hydrocarbon Research and Technology Centre (DHRTC). Also the assistance provided by Bruna Silva Nabuco (Technical University of Denmark), during the experimental campaign in Newcastle needs to be acknowledged.

References

[1] J. Tychsen, M. Dixen, Wave kinematics and hydrodynamic loads on intermediate water depth structures inferred from systematic model testing and field observations – tyra field extreme wave study 2013-15, Offshore Structural Reliability Conference, OSRC (2016).
[2] S. Hughes, Physical Models and Laboratory Techniques in Coastal Engineering, World Scientific Publishing Co Pte Ltd, 2015.
[3] J. Jensen, P. H. Kirkegaard, R. Brincker, Modal and wave load identification by ARMA calibration, Journal of Engineering Mechanics (1992).
[4] N. Perisic, P. H. Kirkegaard, U. Tygesen, Load identification of offshore platform for fatigue life estimation, Structural Health Monitoring 5 (2014) 99–109.
[5] N. Noppe, A. Iliopoulos, W. Weijtjens, C. Devriendt, Full load estimation of and offshore wind turbine based on SCADA and accelerometer data, Journal of Physics Conference Series 753 (2016).
[6] K. Maes, A. Iliopoulos, W. Weijtjens, C. Devriendt, G. Lombaert, Dynamic strain estimation for fatigue assessment of and offshore monopile wind turbine using filtering and modal expansion algorithms, Mechanical Systems and Signal Processing 76-77 (2016) 592–611.
[7] K. Stevens, Force identification problems - an overview, Proceedings of the SEM Spring Conference on Experimental Mechanics (1987) 838–844.
[8] C. Fritzen, M. Klinkov, Load identification for structural health prognosis, North Atlantic Treaty Organization, NATO - Science and Technology Organization (2014).
[9] M. Aenlle, R. Brincker, P. Fernández, A. Fernández, Load estimation from modal parameters, Proceedings of the International Operational Modal Analysis Conference, iomac 1 (2007) 39–50.
[10] B. Wang, C. Chiu, Determination of unknown impact force acting on a simply supported beam, Mechanical Systems and Signal Processing 17 (3) (2003) 683–704.
[11] E. Lourens, E. Reynders, G. D. Roeck, G. Degrande, G. Lombaert, An argumented Kalman filter for force identification in structural dynamics, Mechanical Systems and Signal Processing 27 (2012) 446–460.
[12] J. Hwang, A. Kareem, W. Kim, Estimation of modal loads using structural response, Journal of Sound and Vibration 326 (2009) 522–539.
[13] F. Naets, J. Cuadrado, W. Desmet, Stable force identification in structural dynamics using Kalman filter and dummy-measurements, Mechanical Systems and Signal Processing 50-51 (2015) 235–248.
[14] J. Liu, C. Ma, I. Kung, D. Lin, Input force estimation of a cantilever plate by using a system identification technique, Computer Methods in Applied Mechanics and Engineering 190 (2000) 1309–1322.
[15] K. Maes, K. Nimmen, S. Gillijns, G. Lombaert, Validation of time-delayed recursive force identification in structural dynamics, International Conference on Structural Dynamics, EURODYN (2017).
[16] A. Brandt, Noise and Vibration Analysis, John Wiley and Sons, Ltd, West Sussex, UK, 2011.
[17] R. Brincker, C. Ventura, Introduction to Operational Modal Analysis, John Wiley and Sons, Ltd, Chichester, West Sussex, UK, 2015.
[18] M. Vigsø, M. Tarpø, J. Hansen, R. Brincker, C. Georgakis, Scenario based approach for load identification, Proceedings of the International Modal Analysis Conference, IMAC (2018) 117–125.
[19] J. Wheeler, Method for calculating forces produced by irregular waves., Offshore Technology Conference 1 (1969) 83 – 94.
[20] J. Morison, M. O'Brien, J. Johnson, S. Schaaf, The force exerted by surface waves on piles, Petroleum Transactions, American Institute of Mining Engineers (1950) 149–154.
[21] R. Brincker, L. Zhang, P. Andersen, Modal identification from ambient responses using frequency domain decomposition, Proceedings of the International Modal Analysis Conference, IMAC (2000) 625–630.
[22] J. Juang, R. Pappa, An eigesystem realization algorithm for modal parameter identification and model reduction, Journal of Guidance, Control, and Dynamics 8 (1985) pp 620–627.

[23] J. O'Callahan, P. Avitabile, R. Riemer, System equivalent reduction expansion process, Proceedings of the International Modal Analysis Conference, IMAC (1989).
[24] J. Kristoffersen, C. Georgakis, H. Bredmose, L. Tao, Preliminary experimental study on the influence of the local wind field on forces from breaking waves on a circular cylinder, Proceedings of the 37th International Conference on Ocean, Offshore and Arctic Engineering, ASME (2018).

Chapter 12

Wave loading using time domain identification

Paper VI

"Identifying wave loads during random seas using structural response"

Michael Vigsø, Rune Brincker and Christos Georgakis

Published in Proceedings of the 29th International Ocean and Polar Engineering Conference, ISOPE, Hawaii, 2019 (Peer reviewed)

This chapter presents a study of random wave loading on a cantilever structure. The load identification is performed real-time using state-space models and Kalman filters. The author has performed the ideation, experiments, analysis and the writing of the paper. The paper has been formatted with minor grammatical adjustments to suit this thesis.

Identifying wave loads during random seas using structural response

Michael Vigsø[a,*], Rune Brincker[b], Christos Georgakis[a]

[a] *Aarhus University, Inge Lehmanns Gade 10, 8000 Aarhus, Denmark*
[b] *Technical University of Denmark, Brovej 118, 2800 Kgs. Lyngby, Denmark*

Abstract

Structural monitoring is increasingly becoming everyday business in the offshore industry. The monitoring may target the strain estimation or focus on tracking the changes in the dynamic properties of the structure in order to predict damages at remote / or possibly subsea locations. This paper will show that by monitoring the structural response, it is also possible to indirectly estimate the wave loading acting on the system. This information can be used to increase confidence in the load probability models for the structural design or aid the health monitoring procedure. During ambient vibration, the principles of operational modal analysis (OMA) are applied to harvest the dynamic properties of the structure. Successively, a dynamic model is formulated and used to calculate the loading from a random sea state using the response of the structure. A laboratory experiment is conducted in a wave flume at LASIF, Marseille, France, where a scaled offshore model is equipped with accelerometers to monitor the structural response during a random sea. The study shows that it is possible to use the structure as a dynamic load cell and monitor the loads occurring in actual conditions. Both the short time variations and the load spectra can be computed successfully using the structural response.

Keywords: Wave loading, Indirect measurements, Operational modal analysis, Offshore structures

1. Introduction

In the field of offshore structures, an increase is seen in the subject of monitoring. Recently, TOTAL announced that as for the redevelopment of the Tyra field, the platform Tyra East will be equipped with no less than 100 000 sensors [1]. Most of these will, of course, target the production processes, but the monitoring scope will also include the structural performance. The aim of structural monitoring may be plentiful, for instance with regards to operational limitations such as heading, static deformation or vibration level. The vibration pattern can be used for health diagnostics, and since offshore structures are prone to fatigue damages, monitoring their well-being is essential for ensuring safety and reliability.

Due to the nature of offshore structures, it is common to monitor the surrounding sea state, but more interesting is the wave loading itself rather than the surface elevation. The wave loading depends on the geometry and surface properties of the structure, but also on its dynamics.

*Corresponding author
Email addresses: mvigso@eng.au.dk (Michael Vigsø), runeb@byg.dtu.dk (Rune Brincker), cg@eng.au.dk (Christos Georgakis)

Published in the Proceedings of the International Ocean and Polar Engineering Conference, ISOPE
This paper has been formatted to suit this thesis *June 2019*

Therefore, it is challenging to obtain the load measurements directly and hence we need to rely on indirect methods. By monitoring the response of a structure, it is, indirectly, possible to identify the loading during operational conditions with the actual boundary conditions.

Indirect (wave) load identification has been used in ship design, but it is becoming more common in the field of fixed offshore structures as well. Within industry practice, wind turbines or oil and gas installations are exploited for this. For example the "digital twin" concept introduced by Ramboll Oil and Gas as part of their monitoring programme [2], [3], [4] and [5]. Within academia, early studies [6] suggest the feasibility of wave load estimates using the structural response on a simulated case study. Later studies [7–11] demonstrate how wave loads can be estimated using existing load identification techniques. The studies include both numerical and experimental work and aim to quantify loads from a variety of wave types, including breaking waves.
In this paper, we will add to the study of indirect methods for wave load identification by monitoring a scaled model in a wave flume. The aim of this study will be to estimate the load variations during random seas.

The mathematical notation used is denoting matrices by a double underline and vectors by a single underline.

2. Theory

For the load identification process, we shall rely on the time domain technique using the modally reduced model. The method is adopted from [12] with reference to [13]. The principle is that a modal analysis is performed and modal parameters are obtained for the structure at in-place conditions. The modal parameters are then fed into a recursive modal description together with response measurements from the structure, and by using the means of a linear Kalman filter, an estimate of the wave loading is obtained in real-time.

The performance of the method is sensitive to assumptions regarding the spatial distribution of the load and hence a wave gauge is used to fix the loading to the wetted area of the structure during the random sea. The algorithm is recapped here in a condensed form suited for the need of this study. We start out by defining the state modal coordinates:

$$\underline{x}(t) = \begin{bmatrix} \underline{\underline{\Phi}} & \underline{\underline{0}} \\ \underline{\underline{0}} & \underline{\underline{\Phi}} \end{bmatrix} \underline{\zeta}(t) \tag{1}$$

Here, $\underline{\zeta}(t)$ is the state vector in modal coordinates while $\underline{x}(t)$ is the state vector in physical coordinates. $\underline{\underline{\Phi}}$ contains the mode shapes, expanded, mass normalized and arranged in columns. We arrange the natural frequencies ω_i and the modal damping ξ_i in diagonal matrices such that:[1]

$$\underline{\underline{\Omega}} = \begin{bmatrix} \omega_1 & 0 & 0 \\ 0 & \ddots & 0 \\ 0 & 0 & \omega_n \end{bmatrix}, \qquad \text{and} \qquad \underline{\underline{\Gamma}} = \begin{bmatrix} 2\xi_1\omega_1 & 0 & 0 \\ 0 & \ddots & 0 \\ 0 & 0 & 2\xi_n\omega_n \end{bmatrix} \tag{2}$$

[1] This formulation is based on proportionally damped systems and thus might be violated by the hydrodynamic contribution.

For the classic continuous state space in modal coordinates we have:

$$\dot{\underline{\zeta}}(t) = \underbrace{\begin{bmatrix} \underline{\underline{0}} & \underline{\underline{I}} \\ -\underline{\underline{\Omega}}^2 & -\underline{\underline{\Gamma}} \end{bmatrix}}_{\underline{\underline{A_c}}} \underline{\zeta}(t) + \underbrace{\begin{bmatrix} \underline{0} \\ \underline{\underline{\Phi}}^T \underline{S_p} \end{bmatrix}}_{\underline{B_c}} p(t) \tag{3}$$

Here, we assume that the hydrodynamic added mass and damping are embedded in the modal parameters and thus do not appear directly in the state equation. Another important aspect of this formulation is the separation of the load into the spatial distribution $\underline{S_p}$ and the scaling $p(t)$. Note that the loading may be composed of multiple sources and thus the spatial distribution will be a matrix with load sources arranged in columns, and the scaling will be a corresponding vector. For this study, however, we assume that only one load source is present, i.e. the load caused by the waves. The subscript c indicates that the state matrices are on continuous form.

Since the spatial distribution is not constant during the wave loading, but instead will relate to the water runup on the pile, we will adjust the spatial distribution accordingly using the wave gauge measurements. The position of the wave gauge may be seen in Figure 2. Consequently, the modal load is adjusted as:

$$\underline{q}(t) = \underline{\underline{\Phi}}^T \underline{S_p}\, p(t) \quad \rightarrow \quad \underline{q}(t) = \underline{\underline{\Phi}}^T \underline{S_p}\,(\eta(t))\; p(t) \tag{4}$$

Here, $\eta(t)$ is the water surface elevation near the structure. The principle is sketched in Figure 1. The distribution of the load is derived as an inertia dominated load from a linear wave, given a peak frequency and significant wave height matching the wave spectrum. The distribution is then (with similarity to Wheeler stretching [14]) stretched such that it follows the surface elevation as shown in Figure 1.

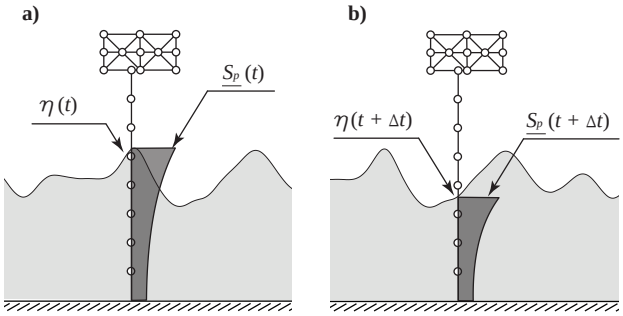

Figure 1: Principle of time varying load distribution. The spatial distribution $\underline{S_p}(t)$ is stretched by the information from the wave gauge $\eta(t)$.

Augmented state

Now, since we wish to obtain an estimate on the input rather than the response, we expand the state vector to include the load (referred to as augmented state vector). That is:

$$\underline{\zeta_a}(t) = \begin{bmatrix} \underline{\zeta}(t) \\ p(t) \end{bmatrix} \tag{5}$$

In Eq. (5), $p(t)$ shall be interpreted as the load scalar function. The subscript a indicates augmented state.

We assume that the augmented state equation in discrete form can be written for time step $k+1$ as:

$$\underline{\zeta_a}(k+1) = \underline{\underline{A_a}}\, \underline{\zeta_a}(k) + \begin{bmatrix} \underline{w}(k) \\ \gamma(k) \end{bmatrix} \tag{6}$$

Here, $\underline{w}(k)$ and $\gamma(k)$ are the noise processes which account for discrepancies in the relation (more about these later). The discrete state transition matrix $\underline{\underline{A_a}}$ is written as:

$$\underline{\underline{A_a}} = \begin{bmatrix} \underline{\underline{A}} & \underline{\underline{B}} \\ \underline{\underline{0}} & \underline{\underline{I}} \end{bmatrix} \tag{7}$$

where

$$\underline{\underline{A}} = e^{\underline{\underline{A_c}}\, dt}, \qquad \text{and} \qquad \underline{\underline{B}} = \left[\underline{\underline{A}} - \underline{\underline{I}}\right] \underline{\underline{A_c}}^{-1} \underline{B_c} \tag{8}$$

Now we have defined the augmented state equation in discrete form and hence we can implement the Kalman filter for a real-time input estimate.

Kalman filter

We assume that the load scalar $p(k)$ remains constant during the time steps and that variations are caused only by a stochastic process also known as a random walk. Hence:

$$p(k+1) = p(k) + \gamma(k) \tag{9}$$

Here, γ is assumed to be Gaussian.

Since the resolution of the mode shapes is greater than the number of sensors, we must define the selection matrix. In general, we wish to link the measurement $\underline{z}(k)$ to the system state $\underline{\zeta}(k)$. Since only accelerations are measured, the state observation equation reduces to (in discrete form):

$$\underline{z}(k) = \left[-\underline{\underline{S_a}}\, \underline{\underline{\Phi}}\, \underline{\underline{\Omega}}^2 \quad -\underline{\underline{S_a}}\, \underline{\underline{\Phi}}\, \underline{\Gamma} \quad \underline{\underline{S_a}}\, \underline{\underline{\Phi}}\, \underline{\underline{\Phi}}^T \underline{S_p}(\eta(k))\right] \underline{\zeta_a}(k) + \underline{v}(k) \tag{10}$$

The selection matrix $\underline{\underline{S_a}}$ is a matrix that picks the degrees of freedom (DOFs) which coincide with the sensors. For example, sensor 1 coincides with DOF 8 and sensor 2 with DOF 7. This yields:

$$\underline{\underline{S_a}} = \begin{bmatrix} 0 & 0 & 0 & 0 & 0 & 0 & 0 & 1 & \dots \\ 0 & 0 & 0 & 0 & 0 & 0 & 1 & 0 & \dots \\ \vdots & & & & & & & & \ddots \end{bmatrix}_{n_{sensors} \times n_{DOF}} \tag{11}$$

An important ingredient for the Kalman filter algorithm is the error covariance matrices (noise models). In lack of information, we often assume that the noise processes are Gaussian and mutually uncorrelated. Hence for the augmented error covariance matrix (with single loading) we get:

$$\mathrm{E}\left\{ \begin{bmatrix} \underline{w}(k) \\ \gamma(k) \end{bmatrix} \begin{bmatrix} \underline{w}^T(k) & \gamma(k) \end{bmatrix} \right\} = \begin{bmatrix} \underline{\underline{Q}} & \underline{0} \\ \underline{0} & S \end{bmatrix} \delta_{kl} \tag{12}$$

Here, δ_{kl} is the Kronecker delta to ensure that the covariance matrix remains diagonal. We will assume a constant value in the system error covariance matrix $\underline{\underline{Q}}$.

In Eq. (9) we have defined the load as a Gaussian random walk. In order to capture any sharp variation in the load, the associated error covariance S must be increased. Several power of magnitude is needed compared to the values in $\underline{\underline{Q}}$ and $\underline{\underline{R}}$.

The measurement noise is also assumed to provide an error covariance matrix with constant values on the diagonal. That is:

$$\mathrm{E}\left\{ \left[\underline{v}(k)\right] \left[\underline{v}^T(k)\right] \right\} = \left[\underline{\underline{R}}\right] \delta_{kl} \tag{13}$$

The remaining part of the algorithm follows the general linear Kalman filter, but with an update in state matrices for each time step given the wave gauge measurements. [15]

3. Experiment

An experiment campaign was conducted at the wave flume facility at LASIF, Marseille University in France, 2018. The laboratory framework covers a bottom-fixed mono-pile structure

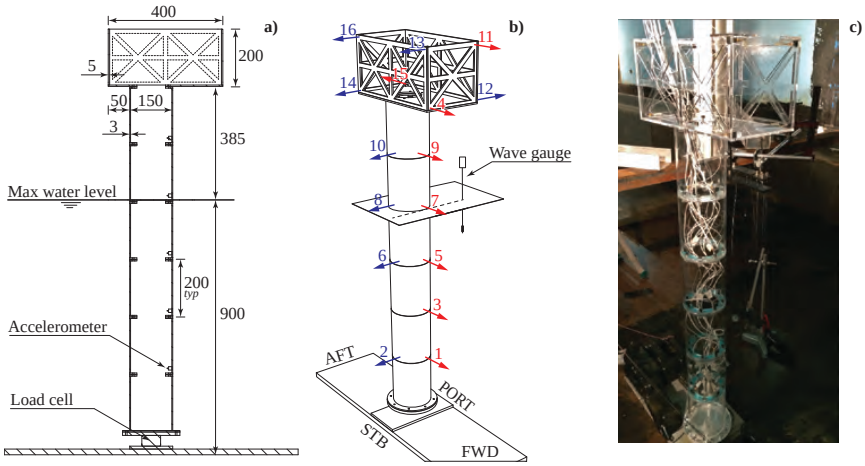

Figure 2: Experimental setup. a) shows the side view cross section including the overall dimensions of the model, b) indicates the sensor position and direction, c) shows a picture from the experiment. Dimensions are in mm. The figure is taken from [16].

subjected to wave loading. Although the model does not descend from any physical (full scale) counterpart, it is roughly scalable as 1/100 given the conditions in the North Sea. The model with key dimensions is shown in Figure 2. The pile is made from hollow sections leaving the inside dry at all times. The sections are bolted together through internal flanges. The model is made from plexiglass and equipped with 16 uniaxial accelerometers (Brüel & Kjær type 4508-B 100 mV/g). Eight of these are facing the incoming waves (red), and eight are facing the transverse direction (blue) as indicated in Figure 2 b). A wave gauge is installed to monitor the surface elevation near the structure. It is positioned at the front of the pile with a transverse offset of 200 mm from the pile centre. The model is attached to an ATI load cell which captures the global loading on the system including dynamic amplification. This is used for verification purposes only. The dynamic characteristics may be seen in Table 1.

A unidirectional random sea is released towards the structure from the front, and the corresponding vibrations are captured by the sensors along with the surface elevation of the passing waves.

Wave Spectrum

The waves are created as a series of random waves generated from a JONSWAP (Joint North Sea Wave Project) wave spectrum. A sample of the wave train is shown in Figure 3 along with the spectrum. The structure is tested for 20 minutes at a sampling rate of 1024 Hz. The spectrum is made using the Welch averaging technique with segments of 32 s and a 50 % overlap [17].

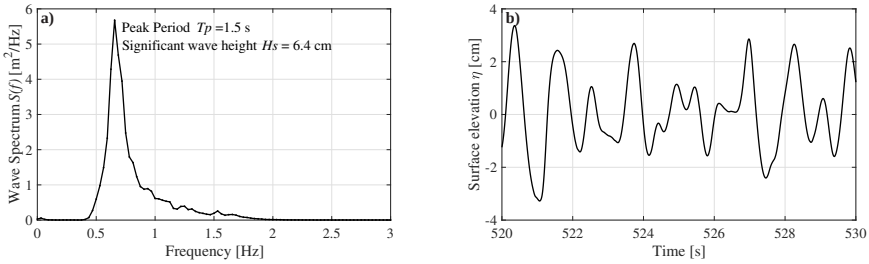

Figure 3: Random sea state: a) shows the wave spectrum of the random waves measured from a wave gauge in close proximity to the pile. b) shows a sample of the unfiltered wave gauge time signal. The significant wave height is calculated as the mean of the 1/3 highest waves using zero down-crossing separation.

Acceleration Spectrum

As a consequence of the random waves, the structure will initiate some vibrations. The vibrations are shown in Figure 4 in both the frequency domain and the time domain. The frequency domain representation is made using the Welch averaging technique with segments of 32 s and a 50 % overlap. The spectra from the 16 accelerometers are decomposed into singular values and the three most significant are shown.

From Table 1 and Figure 3 a) we note that the natural frequency of the structure is well above the main frequency content of the waves and thus expect the response to be mainly quasi-static.

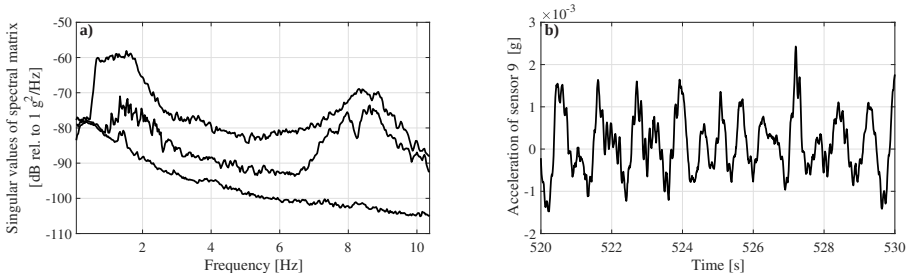

Figure 4: Structural accelerations: a) shows the acceleration spectrum in terms of the singular values [18]. Only the three most significant singular values are shown in descending order. b) shows a sample of the corresponding (unfiltered) accelerations for sensor 9 during the random sea. Sensor 9 is positioned above the water level and is facing the incoming waves.

When we examine the frequency content of the accelerations shown in Figure 4 a), we see how the wave peak frequency f_p is scattered between $1.0f_p$ and $2.5f_p$. The second thing that appears is how the natural frequency is represented in the response at approximately 8.4 Hz. The remaining modes between 35 and 50 Hz are barely visible in the signal.

From the acceleration spectrum in Figure 4 a) it is noted that cross vibrations are present during the experiment as the second singular value near 8.6 Hz corresponds to the first bending mode in the transverse direction. See also Table 1.

Modal Analysis

The acceleration spectrum generated from the one-directional random waves yields a poor basis for operational modal analysis (OMA). Instead, the OMA is based on additional loading, either by including wind or brush strokes by the testing team. The modal analysis is omitted from this paper and the reader may refer to [16] for further details. The first five modes are summarized in Table 1.

Table 1: Estimated modal parameters. See [16] for more details.

Natural frequency f_n [Hz]	Damping ratio ξ_n [%]	Comment on mode shape
8.37	3.7	First bending mode
8.66	3.5	First bending mode, transverse direction
37.6	4.9	Second bending mode
40.3	3.7	First torsional mode
47.0	4.4	Second bending, transverse direction

The experimental mode shapes are scaled and expanded using a surrogate FE model such that the full field deformation of the structure can be estimated. The effect of the hydrodynamic added mass is included as a non-structural mass that only affects the horizontal inertia and not the

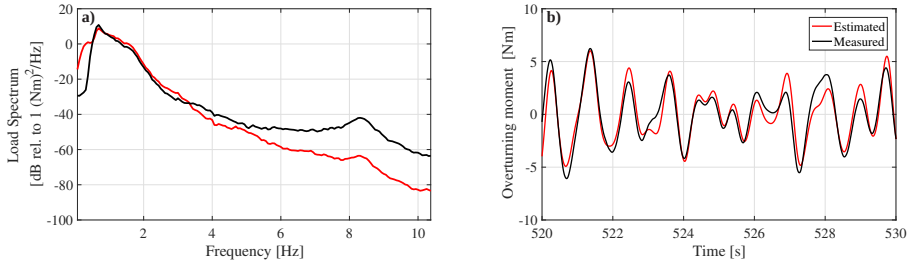

Figure 5: Global loading: a) shows the load spectrum (moment) during the random sea. Red is the estimated load while black is measured by the load cell. b) shows a sample of the corresponding time signal. The load cell data is low-pass filtered at 50 Hz.

torsional. The added mass is included in the updated FE model and is mainly used to scale the mode shapes.

Wave Loading

The global loading on the structure is measured by a load cell at the base. The load cell measures all six degrees of freedom, but we shall confine ourselves to the overturning moment in the direction of the waves. Once again, the spectrum is computed by means of Welch averaging with segments of 32 s and a 50 % overlap, and shown in Figure 5 a). The data from the load cell is contaminated by harmonic noise at 50 Hz. Hence the data shown in Figure 5 has been low-pass filtered to compensate for this. When comparing the time signal in Figure 5 b) and Figure 3 b), we see that the structure experiences the maximum loading before the apparent wave reaches its maximum crest height. When examining the spectrum in Figure 5 a), it is seen that the resonant frequency of the structure is repeated in the reaction forces. This is due to the dynamic interaction between the loading and the system.

4. Results

During random sea, the structural accelerations and wave gauge measurements are recorded and fed into the algorithm. The algorithm then provides a real-time estimate on the wave load (red). The estimated wave load is compared to the measurements from the load cell at the base (black). The comparison is shown in Figure 5 in terms of the overturning moment. We see that the overall trend is captured through the indirect method, although some discrepancies are seen:

When examining the load spectra in Figure 5 a), we see that the estimated spectrum includes some low frequency content that is not seen by the load cell. We expect that this is a result from the performance of the accelerometers at low frequency (< 0.5 Hz).

Next, we observe how the energy is less near the resonant frequency of 8.4 Hz. We recall the objective of the algorithm which is to identify the input, i.e. the wave loading, while it should omit any dynamic amplification from the structure. Since the peak at 8.4 Hz represents a dynamic amplification from the first mode, it also represents a flaw in the identification algorithm as it should not have been represented.

In Figure 5 b), a comparison is made between the estimated input (wave load) and the measured reaction force in the time domain. Again, since the measured force includes the dynamics of the structure and the estimates do not, it is not completely comparable. However, since the primary part of the response is of a quasi-static nature, the difference should be limited and we will not pursue to adjust for this.

When using a real-time algorithm as presented in this paper, it is common to encounter a phase shift in the estimate compared to the measured. Note that the result shown in Figure 5 b) is adjusted for this by an offset of 0.09 s.

5. Discussion

When applying this type of Kalman filter approach for load identification, it is a challenge when only accelerations are available as the state estimates are likely to drift. Filtering and detrending may improve this issue. As an alternative, one can convert an accelerometer into a pseudo displacement sensor through integration in the frequency domain, however, this makes the real-time implementation more challenging.

The performance of the Kalman filter is dependent on the tuning of the noise models, i.e. the error covariance matrices in Eq. (12) and Eq. (13). The parameters chosen for this study are as follows:

$$\underline{\underline{Q}}_{ii} \sim 100, \quad S \sim 10^9 \quad \text{and} \quad \underline{\underline{R}}_{ii} \sim 10 \tag{14}$$

We admit that access to the measured load is very convenient when tuning these parameters for the Kalman filter.

In Eq. (4), we have assumed that the spatial distribution is constant in time apart from the stretching. This is a crude simplification for a random sea as waves with shorter wavelengths will concentrate the load near the surface and vise versa. The spatial distribution could also have been refined in such way that it adds a contribution from a drag dominated scenario and an inertia dominated scenario. This has not been pursued in this paper. In the event that wave breaking or slamming occur near the structure, the frequency content of the accelerations is expected to broaden and hence yield modal activity from higher modes. In order to estimate these loads, more modes are likely needed and possibly another local load model for the impact area. This will be the focus for future study.

6. Conclusion

Through this study, we have experienced the challenges associated with both indirect and direct measurements of wave loading when dealing with both quasi-static and dynamic response. Although challenges remain, we have demonstrated the feasibility of indirect estimation of wave loads on a structure during random seas. The results are based on experimental system identification (OMA) and driven by acceleration measurements. Through simultaneous monitoring of the surrounding sea, the wave loading was constrained to the wetted area of the structure.

We have examined a scenario where the natural frequency of the structure is well above the wave peak frequency. This yields a high portion of quasi-static response. Note that for actual offshore installations, the frequency gap between the peak wave and the structure may be smaller and thus the dynamic response may be larger, e.g. the Valdemar platform in the North Sea, [19].

Acknowledgments

The authors acknowledge the funding received from the Centre for Oil and Gas – DTU/Danish Hydrocarbon Research and Technology Centre (DHRTC).

References

[1] L. Beck, Nu skal 100.000 sensorer midt ude i nordsøen få oliepengene til at sprøjte, Finans, Insigt, (Downloaded from finans.dk on January 31st 2019) (2018).
[2] U. Tygesen, M. Jepsen, J. Vestermark, N. Dollerup, A. Pedersen, The true digital twin concept for fatigue re-assessment of marine structures, Proceedings of the 37th International Conference on Ocean, Offshore and Arctic, ASME (2018a).
[3] U. Tygesen, K. Worden, T. Rogers, G. Manson, E. J. Cross, State-of-the-art and future directions for predictive modelling of offshore structure dynamics using machine learning, Proceedings of the International Modal Analysis Conference, IMAC (2018b).
[4] N. Perisic, P. H. Kirkegaard, U. Tygesen, Load identification of offshore platform for fatigue life estimation, Structural Health Monitoring 5 (2014) 99–109.
[5] N. Perisic, U. Tygesen, Cost-effective load monitoring methods for fatigue life estimation of offshore structures, Proceedings of the International Conferences on Ocean, Offshore and Arctic Engineering OMAE (2014).
[6] J. Jensen, P. H. Kirkegaard, R. Brincker, Modal and wave load identification by ARMA calibration, Journal of Engineering Mechanics (1992).
[7] N. Noppe, A. Iliopoulos, W. Weijtjens, C. Devriendt, Full load estimation of and offshore wind turbine based on SCADA and accelerometer data, Journal of Physics Conference Series 753 (2016).
[8] D. Fallais, S. Voormeeren, E. Lourens, Vibration-based identification of hydrodynamic loads and system parameters for offshore wind turbine support structures, Proceedings of Deep Sea Offshore Wind R&D Conference, EERA DeepWind 2016, Trondheim, Norway (2016).
[9] W. Petersen, O. Øiseth, E. Lourens, Full-scale identification of wave forces exerted on a floating bridge using inverse methods and directional wave spectrum estimation, Mechanical Systems and Signal Processing 120 (2019) 708–726.
[10] K. Maes, W. Weijtjens, E. de Ridder, G. Lombaert, Inverse estimation of breaking wave loads on monopile wind turbines, Ocean Engineering 163 (2018) 544–554.
[11] M. Vigsø, J. Kristoffersen, R. Brincker, C. Georgakis, Indirect wave load estimates using operational modal analysis – preliminary findings, Proceedings of the International Ocean and Polar Engineering Conference, ISOPE (2018a).
[12] E. Lourens, D. Fallais, Full-field response monitoring in structural systems driven by a set of identified equivalent forces, Mechanical Systems and Signal Processing 114 (2019) 106–119.
[13] E. Lourens, E. Reynders, G. De Roeck, G. Degrande, G. Lombaert, An augmented Kalman filter for force identification in structural dynamics, Mechanical Systems and Signal Processing 27 (2012) 446–460.
[14] J. Wheeler, Method for calculating forces produced by irregular waves., Offshore Technology Conference 1 (1969) 83 – 94.
[15] R. Kalman, A new approach to linear filtering and prediction problems, Journal of Basic Engineering 82 (1960) 35–45.
[16] M. Vigsø, T. Kabel, M. Tarpø, R. Brincker, C. Georgakis, Operational modal analysis and fluid-structure interaction, Proceedings of the International Conference on Noise and Vibration Engineering, ISMA (2018b).
[17] P. Welch, The use of fast fourier transform for the estimation of power spectra: A method based on time averaging over short, modified periodograms, IEEE Transactions on Audio and Electroacoustics 15 (1967).
[18] R. Brincker, C. Ventura, Introduction to Operational Modal Analysis, John Wiley and Sons, Ltd, Chichester, West Sussex, UK, 2015.
[19] A. Skafte, U. Tygesen, R. Brincker, Expansion of mode shapes and responses on the offshore platform valdemar, Proceedings of the Internatinoal Modal Analysis Conference IMAC 4 (2014) 35–41.

Chapter 13

Wave load distribution

Paper VII

"Estimating wave load distribution from structural response"

Michael Vigsø and Christos Georgakis

Submitted to Ocean Engineering, 2019 (Under review)

This chapter presents a detailed study of wave load (spatial) distribution during regular wave loading on a flexible structure. The author has performed the ideation, experiments, analysis and the writing of the paper. The paper has been formatted with minor grammatical adjustments to suit this thesis.

Estimating wave load distribution from structural response

Michael Vigsø[a,*], Christos Georgakis[a]

[a] *Aarhus University, Inge Lehmanns Gade 10, 8000 Aarhus, Denmark*

Abstract

Wave loading of offshore structures such as oil rigs and wind turbines are governing for the design of these structures. Since the environmental conditions may change during the lifetime, it is of great interest to evaluate the loads which the structure is exposed to at its current state. Since direct measurements of the loads are often not feasible, operators must rely on indirect methods like vibrations based load identification. In the field of indirect measurements, predicting the distribution of the loading is crucial in determining the magnitude. This paper will focus on this task. By analyzing the response from a miniature platform in a wave flume, a method for mapping the load distribution caused by regular wave loads is outlined. Using the output-only system identification from acceleration measurements of the structure, it is evaluated how accurate the load distribution can be predicted. In the experiment, the load distribution is estimated using both indirect methods (vibration-based) and "direct" methods using a roving set of pressure sensors.

Keywords: Load identification, Pressure distribution, Fluid-structure interaction, Operational modal analysis

1. Introduction

Since structural health monitoring was introduced to the offshore industry in the mid 70s, [1–3] state of the art has undergone major advances. Currently, it has become industry practice to monitor offshore structures on a continuous basis. The primary reason for this monitoring is health assessment / damage detection and also estimating the fatigue damage accumulation [4–7]. These are used for inspection planning and may in principle extend the operational lifetime of the structures. Since the structures often are monitored in terms of response, it is appealing to use this data to evaluate whether the loads, which the structure was designed against, is valid for the actual in-place conditions.

Indirect methods for evaluating the wave loads (on fixed structures) are seen on a couple of occasions in the literature. For instance, Jensen et al. [8, 9] studied the use of ARMA models for identifying wave loads on a cantilever. They assumed that the system could be equivalised as a single-degree-of-freedom system and compared the estimates with analytical results. Maes et al. [10] studied the impulsive loads from breaking waves on a monopile. They used the joint input-state algorithm, [11] and pressure sensors to locally derive the pressure distribution in the splash zone. Vigsø et al. [12, 13] conducted wave flume tests where the wave load spatial distribution was

*Corresponding author

Email addresses: mvigso@eng.au.dk (Michael Vigsø), cg@eng.au.dk (Christos Georgakis)

estimated by merging linear wave theory with wave gauge measurements. Fallais et al. [14] and Perisic et al. [15] did similar research, on a monopile structure, but in a numerical framework. They assumed that the spatial distribution was a known quantity. Generally, for indirect measurements, knowing the spatial distribution is paramount to the success of recreating the input force.

This paper extends the work in indirect measurements of wave loads on offshore structures. Based on a physical experiment conducted in a wave flume at LASIF in Marseille, it is shown how the structural response can be used to derive, not only the phase and magnitude of the load, but also estimate its spatial distribution. We will analyze the response of a miniature structure with similarities to monopile structures in the North Sea. The geometry and dynamic behavior of the structure are causing interaction effects, which makes current load models such as the Morrison equation invalid. The paper will start by outlining the theory of indirect measurements, then followed by the results of direct measurements and in the end, a comparison between the estimated and the measured load will be shown. The study will focus on regular wave loading with coupling effects between the fluid and structure. The direct measurements of the load are done by pressure sensors and a load cell. Due to a limited set of sensors, the approach in mapping the pressure distribution will be based on repetitions where the pressure sensors are repositioned. Since the test focuses on regular waves, and thus the steady-state response, the variations can then be averaged to obtain the full pressure field.

2. Theory

Different approaches exist in indirect load identification, both in the frequency domain and in the time domain. Since the aim of this paper is to analyze the steady-state response, it is convenient to tackle this problem in the frequency domain. We will hence rely on one of the first known methods, which was developed for load identification for military helicopters [16–18]. We start out by assuming that the response from the system will be a linear relations such that

$$\underline{\underline{Y}}(\omega) = \underline{\underline{H}}(\omega)\ \underline{F}(\omega) \tag{1}$$

here, $\underline{\underline{Y}}(\omega)$ is the system response, $\underline{\underline{H}}(\omega)$ is the frequency response function and $\underline{F}(\omega)$ is the load, all represented in the frequency domain. The response is measured by the accelerometers, and the frequency response function is estimated from the modal testing. That leaves the load as the only unknown in this relation, which then can be estimated using inverse methods. Before doing so, we need to establish a frequency response function. From Operational Modal Analysis (OMA), we obtain the modal parameters: mode shapes, damping ratio and natural frequencies. These can be used to synthesize a response function using the modal superposition:

$$\underline{\underline{H}}(\omega) = \sum_{r=1}^{N} \frac{Q_r\, \underline{\phi_r}\, \underline{\phi_r}^T}{j\omega - \lambda_r} + \frac{Q_r^*\, \underline{\phi_r}^*\, \underline{\phi_r}^H}{j\omega - \lambda_r^*} \tag{2}$$

here, $\underline{\phi_r}$ is the mode shape vector, Q_r is a scaling constant, λ_r is the complex pole, all for mode r. Superscript * and ^{H} means the complex conjugate and Hermitian transpose respectively. The poles, λ_r can be written as

$$\lambda_r = -\zeta_r \omega_r \pm j\omega_r \sqrt{1 - {\zeta_r}^2} \tag{3}$$

here, ζ_r is the damping ratio and ω_r is the natural frequency, both for mode r. The scaling constant Q_r is obtained as

$$Q_r = \frac{1}{j\, 2\omega_{dr}\, m_r} \tag{4}$$

where, m_r is the modal mass and ω_{dr} is the damped natural frequency.

Simply pre-multiplying by the inverse response function in Eq. (1) has shown to yield poor estimates on the load [19–22]. This is due to high sensitivity from truncation errors and singularity issues at some frequencies. Now, if a loading scenario constrains the estimation process, it makes the process more stable. If we say that the system is subjected to a single load source, it is convenient to separate the load into a spatial distribution and an associate scaling function.

$$\underline{\underline{Y}}(\omega) = \underline{\underline{H}}(\omega)\ \underline{S_p}\ g(\omega) \tag{5}$$

here, $\underline{S_p}$ is a time invariant spatial distribution of the load and $g(\omega)$ is the corresponding scaling function. When making this formulation, it is essential to note that the distribution is not changing in time, although it can scale to zero.

2.1. Procedure for determining the load distribution

Next, the procedure for predicting the load distribution is outlined. The concept is adopted from [23]. We expect the structure to be inertia dominated, i.e. the maximum and minimum load will appear around the wave zero crossings and, thus, making the assumption on a time-invariant distribution more valid. The procedure is based on systematic guesswork (evaluating a set of likely scenarios) as indicated by the flowchart below.

guess $\underline{S_p}$ (6)

Evaluate the product between the response function and the spatial distribution

$$\underline{c}(\omega) = \underline{\underline{H}}(\omega)\ \underline{S_p} \tag{7}$$

The expression is substituted into Eq, (5) and solved for the scaling constant $g(\omega)$ in a least square manner:

$$\hat{g}(\omega) = \underline{c}(\omega)^{\dagger}\underline{Y}(\omega) \tag{8}$$

In order to evaluate the quality of the guess, the response is synthesize using the estimated distributed and scaling:

$$\underline{\hat{Y}}(\omega) = \underline{\underline{H}}(\omega)\ \underline{S_p}\ \hat{g}(\omega) \tag{9}$$

Compare the synthesized response with the measured response and assess the error.

$$\varepsilon\left(\underline{\hat{Y}}(\omega),\ \underline{Y}(\omega)\right) \tag{10}$$

Change $\underline{S_p}$ until a minimum error is achieved or all likely scenarios are evaluated.

here, ε is an error function between the two signals. For this implementation, the Root Mean Square (RMS) error is used in the time domain. We will return to the actual distributions and results in Section 5.

3. Experimental setup

An experiment campaign was conducted in April 2018 at LASIF (Large Air-Sea Interaction Facility) in Marseille. In the wave flume, a bottom-fixed monopile structure with a box girder topside is positioned. The model, which is flexible, is characterized by having a low mass ratio and a large diameter to wavelength ratio. These combined are expected to yield interaction effects which are hard to predict through analytical methods. The literature on the experimental study of wave load distributions on flexible models is limited. Luhar and Nepf [24] did research in this area, but the dynamics and scale were much different from what is presented in this study as they analyzed seabed vegetation, which engages large deflections. Paulsen and Bredmose et al. [25, 26] studied the wave loads on bottom fixed flexible models similar to this current paper, yet their main focus was the total loading rather than the distribution. Many sources have worked on the dynamic pressure distribution on a cylinder caused by wave diffraction, for example, Neelamani et al. [27] or Akyuldiz [28], but these were focusing a rigid structural system. Marine risers, which are very flexible in nature, are often studied with regards to vortex shedding, e.g. [29, 30]. These structures, however, have a different static system as they are fixed in either both ends or suspended from the top.

Due to the nature of the problem, it is not straightforward to measure the loads directly, when interaction effects occur. This may be why limited experimental work has been carried out in the past. Methods for estimating the effect from a weak coupling on linear systems are seen in [31], where a generalization to the Morison equation is implemented by the relative movement between the fluid and the structure.

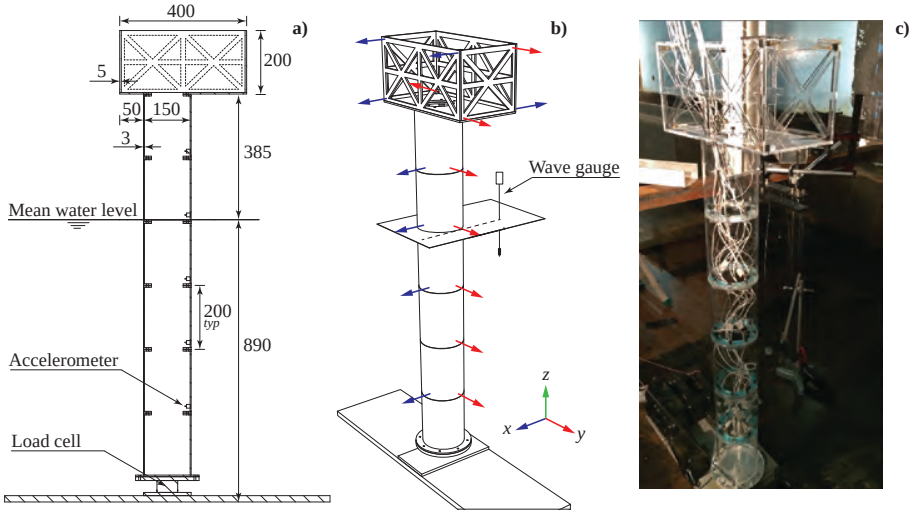

Figure 1: Experimental setup. The figure is a modified reprint taken from [32]. a) shows the overall dimensions of the model (Measurements in mm). b) shows the accelerometer location. c) shows a photo from the experiment prior to water filling.

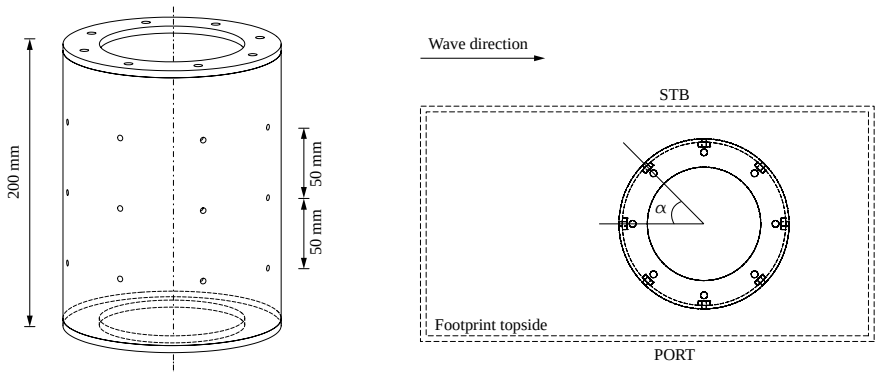

Figure 2: The sketch is showing the pressure sensor array. The section contains 24 mounting holes, eight of which are used at a time. Dummy sensors are installed at slots not used.

3.1. The model

The pile is hollow, circular and made from plexiglass material. The pile remains dry on the inside during the experiment, and this is mainly due to sensor concern. A picture from the experiment can be seen in Figure 1 along with the overall dimensions of the model. As seen, the pile is built from a set of identical 200 mm sections which are bolted together through internal flanges. This makes the sensor installation more manageable, but it also serves another purpose as one section of the pile is made a little different compared to the rest. As seen in Figure 2, this section is perforated such that pressure sensors can be inserted. An array of eight pressure sensors (Kulite XTL-190SM 60 mV/bar) are placed at 45° intervals. The section has more holes than sensors available, and dummies hence blind the unused holes. The model can then be disassembled and the section containing the pressure sensors can be moved up and down as the wave tests are repeated. Once averaging, this provides the full field pressure map during regular waves.

In order to measure the structural response, the model is equipped with 16 uni-axial accelerometers (Brüel & Kjær 4508-B 100 mV/g). Eight of these are facing the incoming wave and eight are facing in the transverse direction. It may be seen from Figure 1 that nine sensors are positioned inside the pile of the model while the remaining seven are positioned at the corners of the topside. For offshore structures, sensor installation below the sea level is uncommon due to maintenance and accessibility on installation.

At the very base, the model is attached to a six-DOF force transducer (ATI Mini-58), which then can measure the global reaction forces. The force transducer is based on strain gauges, i.e., the load is derived from relative movements between the structure and the base.

In front of the pile, a wave gauge is positioned. The wave gauge will give information on the water surface and allow for segmenting the measurement from individual waves.

3.2. The flume

The laboratory facility at the campus of Luminy in Marseille hosts a 40 m long wave flume. The flume is 2.6 m wide and allows for a water depth of 0.9 m. The waves are generated from one end by a piston-type wavemaker. In the opposite end, the waves are passively absorbed by a

permeable beach. The model is placed at approximately 30 m from the wavemaker in the center of the flume. During the experiments, the water temperature was 12°C while the room temperature was at 19°C.

3.3. The tests

The experiment is conducted as a series of repetitive sets which, in the end, is combined to a single conclusion. The tests related to this paper can be grouped into two categories: 1) regular waves and 2) random loading. The random loading should not be confused with random sea state. It is generated by the testing team by brush strokes to any part of the structure above water level. Meanwhile, as the person supplying the brush strokes is standing in waders next to the model, this generates also some activity in the waters. The response from this exercise is used for system identification, i.e., Operational Modal Analysis [33]. The paper, [32], describes in detail the modal identification process and how the modal parameters changed as the flume was filled with water.

The tests regarding the regular waves will be used for load identification. Due to a limited set of pressure sensors, the model must be reconfigured in order to map the full pressure field. This consequently means that the model is build to one configuration, then after a series of wave tests, the model is extracted from the flume, rebuild and then reinserted into the flume for more tests. This is then repeated until sufficient resolution is obtained for the pressure distribution. Between each test, OMA is again performed to ensure that the dynamic properties are not altered unacceptable. The OMA tests each had a duration of 300 s, which corresponds to approximately 2400 times the first natural period.

For each build configuration, two tests of regular waves were conducted. Each test was simulated for approximately 300 s. During the tests, pressure sensors, force transducer and accelerometers were sampling at 2048 Hz while the wave gauge was measuring at 1024 Hz.

3.4. The wave of interest

The wavemaker generates a sinusoidal wave train with a frequency of 0.6 Hz and a wave height of 7 cm. What was obtained in the flume is shown in Figure 3. The figure shows the average wave

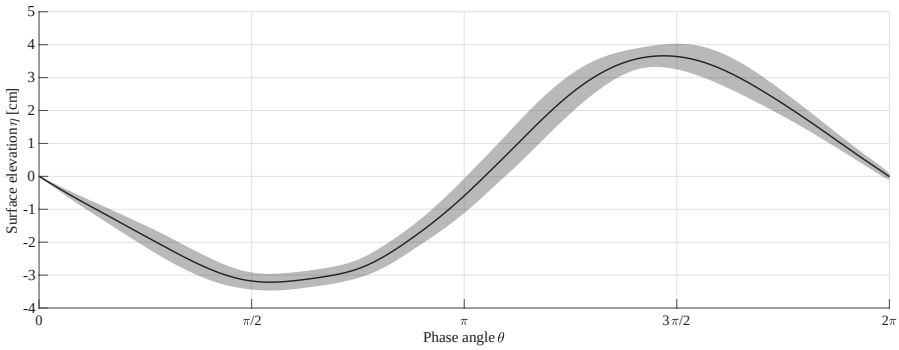

Figure 3: Average wave profile including the uncertainty bound of twice the standard deviation, $\pm\, 2\sigma$. The figure is generated from 1445 waves using the zero-down crossing. Waves with period outliers have been removed prior to the analysis.

Table 1: Characteristic wave.

Parameter	Symbol	Value	Unit
Average water level	d	0.89	m
Average wave height	H	0.069	m
Average wave length	λ	3.88	m
Average wave period	T	1.67	s
Average wave (crest) amplitude	a	0.037	m
Wave number	k	1.62	m^{-1}
Relative wave steepness	H/λ	0.018	-
Relative wave height	H/d	0.078	-
Relative wave length	λ/d	4.36	-
Incident wave length and cylinder diameter ratio	λ/D	25.9	-
Structure mass / displaced mass ratio		0.31	-

profile when waves are separated through zero-down crossing. Only waves at a wave period of $\pm$ 2 % of the average are stored for analysis. Likewise are waves with outlying amplitude omitted. When looking at the average wave profile shown in Figure 3, we note a small asymmetry around the mean water level yielding a wider trough and a steeper crest. The wave parameters can be seen in Table 1.

4. Direct measurements

This section contains the methodology and results for "direct" mapping the load distribution. Recall that the purpose is to estimate the distribution through indirect methods, and hence, the outcome of this section shall be used for comparison and verification purposes.

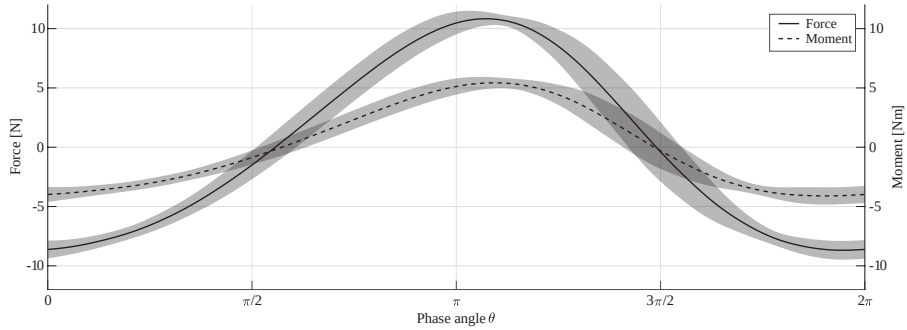

Figure 4: Average mudline loads recorded by the load cell including the uncertainty bound of twice the standard deviation, $\pm$ 2σ.

4.1. Force transducer

First, the measurements obtained from the force transducer will be analyzed. As the regular waves are passing the structure, the reaction forces are measured by the load cell. The data is segmented into individual waves and averaged. The result is shown in Figure 4 in terms of shear force and overturning moment. The data is composed from all tests combined and lowpass filtered at 50 Hz. The maximum load is achieved at a wave phase angle of 1.07π (i.e. close to the wave zero-up crossing) indicating that the structure is likely inertia dominated.

4.2. Pressure sensors

The measurements obtained from the pressure sensors can be used to derive a load distribution, given by the difference in pressure on the front and backside of the pile. If the pressure is integrated over the entire wet surface of the pile, this yields the total wave loads. Since the number of pressure sensors is limited, this will be done stepwise: The pressure sensors are placed in an array covering 360 degrees of the pile at 45-degree intervals. During the regular wave tests, the average pressure variation is thus obtained at a given depth. The pressure from such an exercise can be seen in Figure 5, where the pressure has been interpolated between the sensors. The figure shows the pressure at a constant depth at four different phases of the average wave.

The corresponding line load at this depth is calculated by circumferential integration:

$$f_y(z,t) = \int_0^{2\pi} p(z,t,\alpha)\, r\, \cos\alpha \, \mathrm{d}\alpha \tag{11}$$

$$f_x(z,t) = \int_0^{2\pi} p(z,t,\alpha)\, r\, \sin\alpha \, \mathrm{d}\alpha \tag{12}$$

here, $f_y(z,t)$ is the resulting line load in y direction [N/m], i.e. acting in the direction of the wave and $f_x(z,t)$ is the resulting line load in the transverse direction. $p(z,t,\alpha)$ is the absolute pressure as a function of depth, time and angle, r is the pile radius and α is the angular offset as defined in Figure 2.

The section containing the pressure sensors is now moved up or down, and the test is repeated. Once combined, the load distribution from the waves can be found. Figure 6 shows the pressures

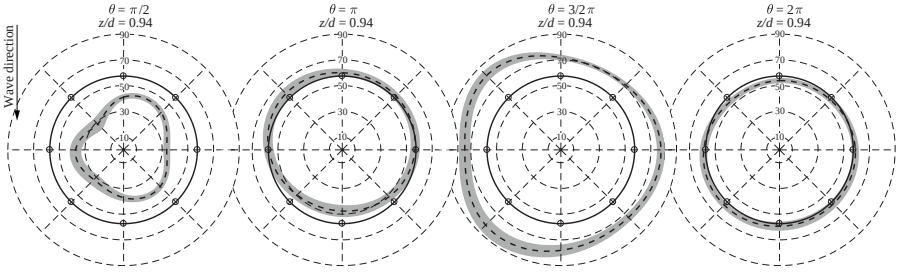

Figure 5: Average pressure variations during the passing of a wave including the uncertainty bound of twice the standard deviation, $\pm\, 2\sigma$. The pressure is measured at a constant depth near the surface. The scale indicates pressure in terms of mm water column. The solid black line indicates the static pressure at still water. Interpolation is performed using a spline function.

at different depths at a given phase angle. The phase shown corresponds to the time of maximum loading. In the right-hand side of the figure, the model is sketched and shows where six different levels are evaluated.

The obtained line load is shown in Figure 7 again at the time of maximum loading. Here the load at the base of the structure has been assumed as a fraction of the nearest measurement. A fraction of 0.9 is used. The line load obtained from the pressure integration is compared with estimates from linear wave theory and the Morison equation [34]. Note that the characteristic wave has a steepness which borderlines the validity range for linear theory, yet the result is shown for reference.

A deviation between the integrated pressure and the analytical result from the Morison equation is evident. As the line load from the analytical approach keeps increasing near the surface, the load measured from the pressure sensors decreases. This effect can be attributed to the fluid-structure interaction. As the structure experiences the highest vibration amplitude away from the floor, the interaction effect also increases. This may also be seen directly from the pressure measurements in Figure 6. If we compare the pressure at $z/d = 0.88$ and $z/d = 0.99$, we see that the restoring pressure on the aft side of the pile is increased near the surface while the driving pressure is nearly

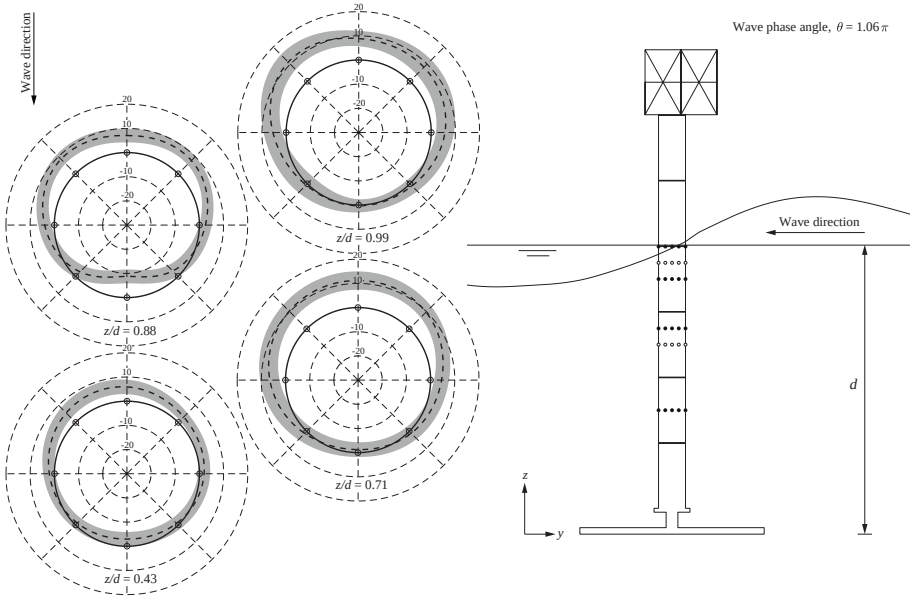

Figure 6: Pressure distribution at maximum loading. Four selected positions are shown on the left-hand side with the mean pressure distribution and an uncertainty bound of twice the standard deviation, $\pm 2\sigma$. Here, the pressure has been normalized to zero pressure at still water level, and the scale consequently shows the absolute variation in mm water column. The right-hand side shows the corresponding surface elevation. Note that the surface elevation has been scaled by a factor 4.

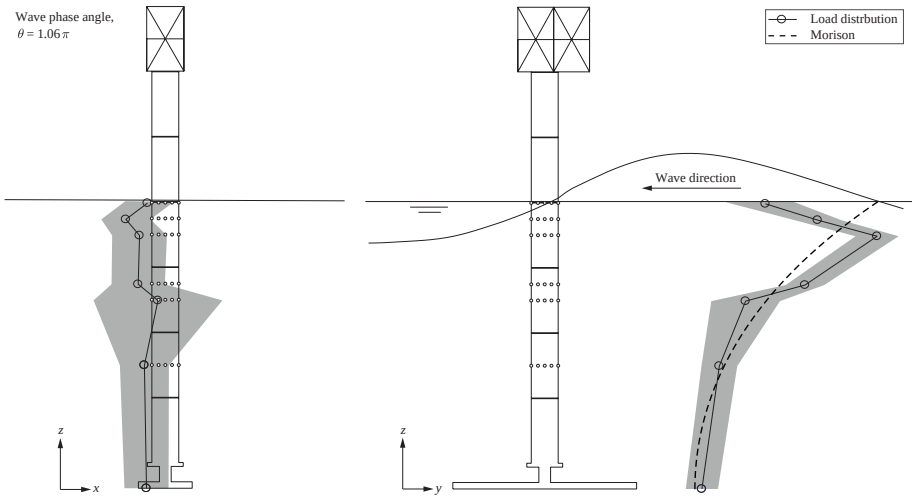

Figure 7: Load distribution calculated from the integrated pressure and shown with linear interpolation at the time of maximum loading. An uncertainty band of $\pm\sigma$ is shown in grey. The dashed line indicates the theoretical wave loading using linear wave theory and the Morison equation ($Cd = 1.3$ and $Cm = 1.9$). Note that the surface elevation has been scaled by a factor 4.

unchanged. This naturally generates a reduced line load. This result is rarely reported for this type of structures, although similar near-surface pressure drop seen in cases of sloshing in flexible container walls [35].

The loads in the transverse direction are subjected to high scatter and do not pose any interest for the future study. We hence aim our attention at the loads parallel to the wave, that is the 'y' direction. The line load is consequently integrated over the wet surface of the model and a global load is derived from pressure sensors and thus making it comparable with the readings from the load cell. The result is shown in Figure 8. Again we note that the maximum loading occurs near the time of zero-up crossing, which indicates inertia dominated loading scenario. It is seen that the scatter in the total load is higher compared to what is measured by the load cell, but the phase, amplitude and point of attack are in good correlation. Here the line load has been linearly extrapolated to the water surface when needed. A comparison of the estimated point of attack during maximum positive and negative wave loading is summarized in Table 3 in Section 6.

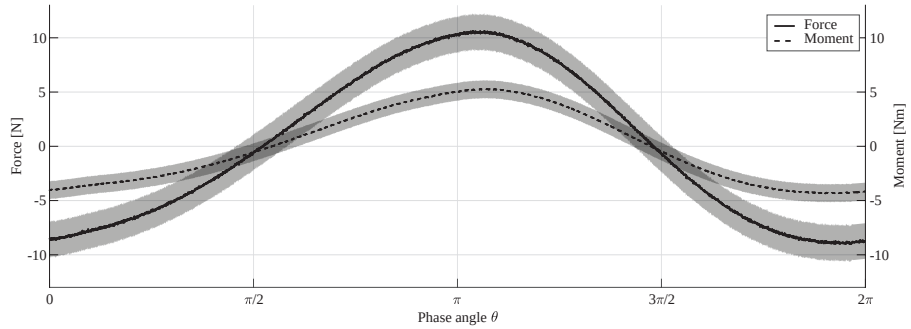

Figure 8: Average mudline loads estimated by integrating the pressure. An uncertainty band of $\pm\sigma$ is shown in grey (Calculated as a sum of uncorrelated variables).

5. Indirect measurements

Now we turn to the indirect estimates. This approach involves a couple of pre-steps before a result can be obtained. We start by noticing that the FRF matrix expressed by Eq. (2) is based on the structural displacements (also known as receptance or dynamic flexibility) and whilst the response is measured in terms of accelerations these must be converted to accommodate the basis of the FRF matrix. The accelerations can be converted to displacements through integration in the frequency domain.

$$\underline{y}(t) \approx \mathcal{F}^{-1}\left(\frac{\mathcal{F}\left(\underline{a}(t)\right)}{-\omega^2}\right) \tag{13}$$

where $\mathcal{F}(\cdot)$ is the Fourier transform, $\mathcal{F}^{-1}(\cdot)$ is the inverse Fourier transform, $\underline{a}(t)$ contains the accelerations and $\underline{y}(t)$ holds the displacements. In practice, this operation requires a highpass filter to avoid drift caused by noise near DC. Here a threshold of 0.5 Hz is applied.

The response during wave action is shown in Figure 9. Here, the typical structural acceleration response is shown for three passing waves. The figure shows the accelerations measured in the forward-aft direction at approximately still water level. As seen, the structure yields vibration at a higher frequency than the waves. This frequency corresponds to the first natural frequency of the structure.

5.1. System identification

The response from the 'pseudo' random loading can be used for the purpose of system identification if we assume a stationary process. Operational modal analysis can be applied in this context [33]. Many different identification techniques exist for this job, and any one of these can be used. For this study, the time domain poly-reference technique is used. We will not go into details with the method, but a general description is outlined so that the basic principle is clear.

The correlation function matrix is made from the response during random loading

$$\underline{\underline{R}}(\tau) = \mathrm{E}\left[\underline{y}(t)\ \underline{y}^T(t+\tau)\right] \tag{14}$$

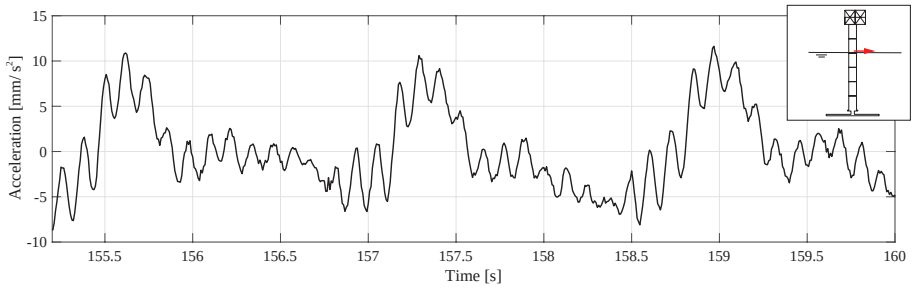

Figure 9: Forward-aft accelerations measured at the mean water line as indicated by the red arrow in the top-right corner (Positive acceleration is in the aft direction). The figure shows the time series for three successive waves. Oscillation at 8.4 Hz is seen which corresponds to the first natural frequency of the structure. Note that the signal has been decimated from 2048 to 128 Hz.

These are treated as free decays of the system and the poly-reference technique by Vold [36] can be applied. The block Hankel matrices are formed, and the autoregressive coefficients can be obtained by a least-square approach. Finally, the AR coefficients are fed into a companion matrix from which an eigenvalue decomposition grants the poles and mode shapes of the system. Please see [32] for the detailed analysis.

Although OMA (in principle) does not require any artificial excitation of the structure and thus being a very convenient method for modal testing, one major drawback persists. This drawback concerns the scaling of the mode shapes and consequently the modal mass. Some methods exists to overcome this issue experimentally e.g. [37, 38]. However, in the present study, a Finite Element (FE) model is used to aid the scaling issue. The model is made from simple Bernoulli beam elements and updated to reflect the behavior of the physical model. The FE model suits as a surrogate model which can be used both for mass normalization and expansion of the experimentally obtained mode shapes. The effect from the hydrodynamic added mass is included as a static contribution to the translational degrees of freedom so that it does not affect the torsional modes [39]. The hydrodynamic added damping is assumed to be included in the estimated modal damping and is not processed further. The expansion makes it possible to interpolate the response between the sensors, which yields a higher resolution during the load identification. The expansion is done using the principles of SEREP [40] using five modes. The frequency response function is subsequently established using the same five modes, i.e., the modes up till 60 Hz, see e.g. Figure 14. The modal parameters from the FE model and the OMA is summarized in Table 2.

Table 2: Modal parameters obtained from the FE model and the OMA.

Mode	1	2	3	4	5
FE frequency [Hz]	8.37	8.65	37.0	39.6	50.1
OMA frequency [Hz]	8.37	8.66	37.6	40.3	47.0
OMA damping [%]	2.7	2.1	4.9	3.7	4.4
Modal assurance criterum [41] [-]	0.99	0.99	0.96	0.91	0.87

5.2. Result from an equivalent point load

We will now turn to the load identification process. The procedure outlined in Section 2.1 states that the spatial distribution ($\underline{S_p}$) must be guessed. We will open this guesswork by using a brute force approach. It is hence assumed that the wave loading can be approximated as an equivalent point load. Systematically, starting the bottom of the pile and moving upwards, we will make a guess on the position of this point load. An error is evaluated from each guess, and the minimum

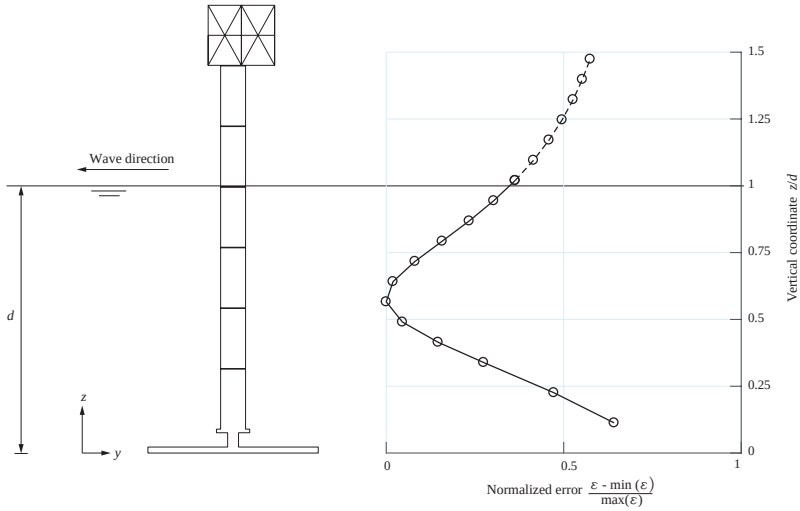

Figure 10: Normalized error chart. Every point in the chart corresponds to the position of an equivalent point load. The minimum error corresponds to the most likely point of attack. The estimates above the water level are included for the sake of completeness, although these could have been filtered away beforehand.

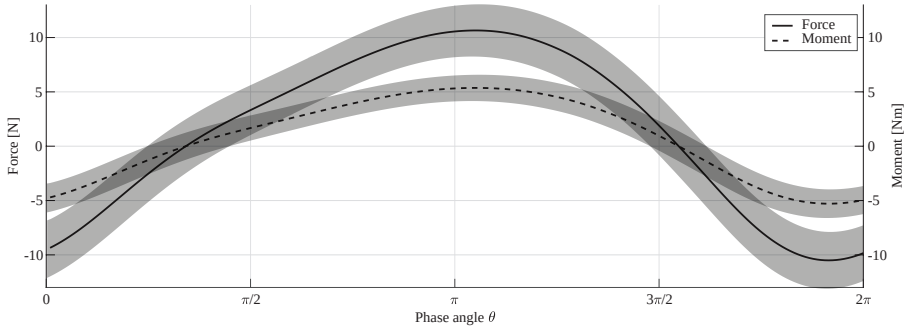

Figure 11: Average mudline loads estimated using the structural response (accelerations). An uncertainty band of $\pm\sigma$ is shown in grey. The result is based on an equivalent point load located at the 0.504 m from the seabed. This corresponds to the minimum error in Figure 10.

error hence corresponds to the most likely position. Figure 10 shows the results from this. Here it should be noted that the resolution of the model has been increased through the modal expansion, thus allowing for interpolation between sensors. The wave load magnitude and phase can now be obtained from the product between the spatial distribution and its corresponding scaling function. The load is again averaged over one wave period, and the result is showed in Figure 11.

5.3. Result from distributed loads

The results from the equivalent point load showed a very distinct minimum at a distance of 0.504 m from the bottom. The scenarios are now expanded to evaluate a series of distributed loads. Four different distributions are evaluated. These are sketched in Figure 12 along with the equivalent point load. All of the distributions span the area between the seabed and mean water level. Distribution b) is a constant load over the entire water column which yields a centroid below a). Distribution c) is a trapezium yielding the same centroid as the point load in a). Distribution d) is a triangle which yields a centroid above a). Distribution e) is the result obtained from the pressure sensors. This is included for reference only as the pattern is an unlikely guess. The same procedure is carried out to evaluate if a more detailed load distribution can be foreseen in this given study. The RMS errors are shown in Figure 13. As seen from the error bars, it is not possible to definitive pick one distribution as a better alternative to the point load.

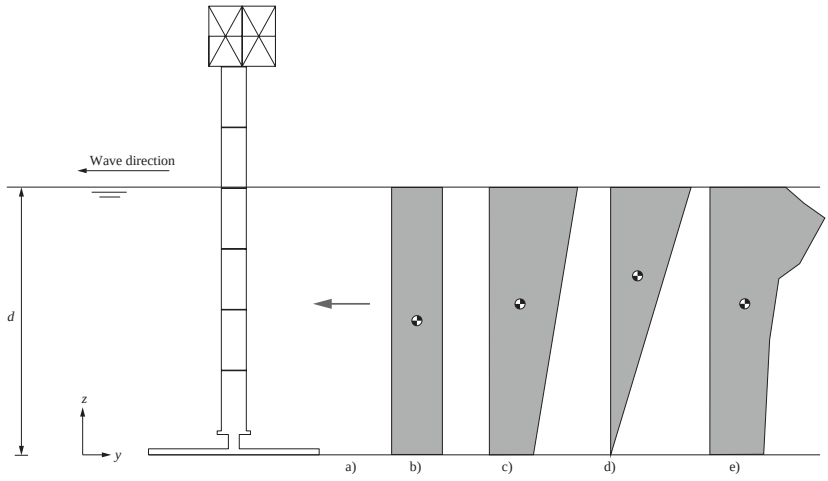

Figure 12: Different load distributions. a) is the point load estimated from Figure 10. b) is a uniform distribution over the wetted area. c) is a trapezium-shaped distribution with the same point of attack as in a). d) is a triangle ranging from zero at the seabed to unity at mean water level. Finally, c) is the distribution obtained from the pressure sensors in Figure 7.

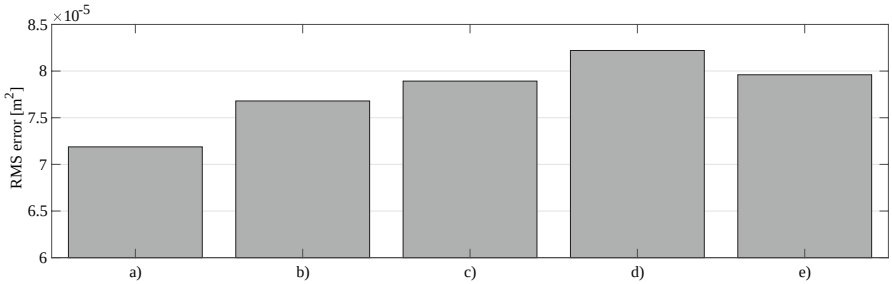

Figure 13: RMS error from different load distributions. For reference, the errors associated with the point loads in Figure 10 are ranging between 7.2×10^{-5} and 14×10^{-5} m^2 thus making all of these good candidates in comparison.

6. Discussion

The estimated variation in load during an averaged wave are evaluated using three different approaches; force transducer, pressure integration and acceleration data. The estimates have similar phase and amplitude although the scatter varies. The estimated point of attack during the maximum loading is summarized in Table 3. Here we see that the loads are well in phase while deviations of $\pm 4\,\%$ exists on the estimated point of attack. For the indirect method, it was assumed that the spatial distribution is time-invariant. This may sound like a crude assumption considering the wave runup during wave crest. However, since the structure is inertia dominated (maximum loading at wave zero-crossing), it can be used as a reasonable estimate.

Table 3: Measured and calculated point of attack (PoA) for the three different approaches.

		Max positive load		Max negative load	
	Calculation	PoA	Phase	PoA	Phase
Load cell	$M_x(t)/F_y(t)$	0.499 m	1.07π	0.472 m	1.94π
Pressure sensors	$\int_0^{d+\eta} f_y(z,t)\ z\ \mathrm{d}z / \int_0^{d+\eta} f_y(z,t)\ \mathrm{d}z$	0.518 m	1.06π	0.500 m	1.95π
Accelerometers	$\min(\varepsilon)$	0.504 m	1.06π	0.504 m	1.92π

The loading obtained from the pressure sensors is based on several tests where the sensors are moved around. In order to move the section containing the pressure sensors, the model needs to be disassembled and rebuild into a new configuration. This alteration causes deviations in the dynamics of the model, which may cause uncertainty to the results. It has been assumed that this effect is neglectable for the purpose of measuring the pressure field. In order to quantify the deviations between each build operational modal analysis was conducted each time the model was reassembled. The scatter in natural frequency and damping estimates can be seen in Figure 14 for each build. The clusters within each build are obtained by a sliding bandpass filter in the frequency domain. System identification is performed as the filter moves. The estimates are filtered and sorted according to the modal assurance criterium [41]. Note that only sensors attached to the topside are kept once the model was disassembled the first time.

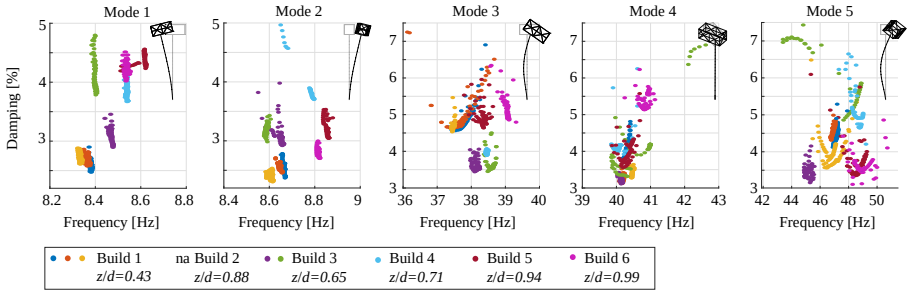

Figure 14: Cluster diagram of identified modal parameters. The z/d value in the legend indicates the relative position of the pressure sensors. Note that build configuration number two was not subjected to random loading, thus modal parameters are not available. The mode shapes shown in the corner are taken from the FE model.

7. Conclusion and future work

In this paper, we have studied the wave load distribution from regular wave loading on a flexible structure. This study was based on the axiom that "all good comes to those who average." A finite amount of pressure sensors was prohibiting a detailed mapping of the pressure field around the structure during the waves. This was remedied by a roving group of sensors and repetitions of the test which allowed for an averaged result. The pressure was integrated to yield a line load distribution and a total load caused during one wave period. The result from this was compared with the measurements from a force transducer at the base, and the result showed good agreement.

It was found that due to the coupling between the structure and the waves, traditional methods for evaluating the loads were inadequate. Instead, a different approach using indirect methods was evaluated. By using the structure accelerations, an equivalent point load was estimated. Both the location and amplitude of the estimated load were in good agreement with the direct measurements. It was evaluated whether a more detailed load distribution could be obtained from the indirect method; however, for this experimental setup, this was not possible. In the end, the effect from noise, modelling and truncation errors made it difficult to distinguish between the presented distributions. Although the indirect method gave good result in terms of the averaged variation, the scatter obtained is more significant compared to the direct measurements.

The results from pressure sensor integration are also subjected to scattering compared to the load cell. Small misalignments between test repetitions could be masking local effects from the interaction, so to instead PIV (Particle Image Velocimetry) or DIC (Digital Image Correlation) could have been an alternative approach. This, however, requires a substantially different experimental setup.

The model was constructed in segments which allowed for sensor installation at any point desirable. But with this, many sources of non-linearities are likewise introduced. If the model could be simplified, it would reduce the amount of uncertainty in the study. In addition, if a fixed model could be analyzed in parallel, it could be used for verification of the influence of flexibility.

Acknowledgments

The authors acknowledge the funding received from the Centre for Oil and Gas – DTU/Danish Hydrocarbon Research and Technology Centre (DHRTC). The staff from Luminy, Marseille are appreciated for their effort during the experiment campaign. Here, especially Hubert Branger and Christopher Luneau should be mentioned. Assistance from PhD students from Aarhus University should also be acknowledged. Here, the help from Thomas Kabel and Julie Kristoffersen is much appreciated.

References

[1] R. Begg, A. Mackenzie, C. Dodds, O. Loland, Structural integrity monitoring using digital processing of vibration signals, Proceedings of the Offshore Technology Conference, Houston, Texas (1976).

[2] O. Loland, C. Dodds, Experiences in developing and operating integrity monitoring systems in the North Sea, Proceedings of the Offshore Technology Conference, Houston, Texas (1976) 313–319.

[3] R. Nataraja, Structural integrity monitoring in real seas, Proceedings of the Offshore Technology Conference, Houston, Texas (1983) 221–228.

[4] D. Augustyn, U. Tygesen, M. Ulriksen, J. Sørensen, Data-driven design and operation of offshore wind structures, Proceedings of the International Ocean and Polar Engineering Conference, ISOPE (2019).

[5] U. Tygesen, M. Jepsen, J. Vestermark, N. Dollerup, A. Pedersen, The true digital twin concept for fatigue re-assessment of marine structures, Proceedings of the 37th International Conference on Ocean, Offshore and Arctic, ASME (2018a).

[6] U. Tygesen, K. Worden, T. Rogers, G. Manson, E. J. Cross, State-of-the-art and future directions for predictive modelling of offshore structure dynamics using machine learning, Proceedings of the International Modal Analysis Conference, IMAC (2018b).

[7] C. Devriendt, F. Magalhaes, W. Weijtjens, G. De Sitter, A. Cunha, P. Guillaume, Structural health monitoring of offshore wind turbines using automated operational modal analysis, Structural Health Monitoring 13 (2014) 644–659.

[8] J. Jensen, P. H. Kirkegaard, R. Brincker, Modal and wave load identification by ARMA calibration, Journal of Engineering Mechanics (1992).

[9] J. Jensen, P. H. Kirkegaard, R. Brincker, Modal and wave load identification by ARMA calibration, Fracture and Dynamics R9035 (27) (1990).

[10] K. Maes, W. Weijtjens, E. de Ridder, G. Lombaert, Inverse estimation of breaking wave loads on monopile wind turbines, Ocean Engineering 163 (2018) 544–554.

[11] K. Maes, Q. Smyth, G. De Roeck, G. Lombaert, Joint input-state estimation in structural dynamics, Mechanical Systems and Signal Processing 70-71 (2016) 445–466.

[12] M. Vigsø, J. Kristoffersen, R. Brincker, C. Georgakis, Indirect wave load estimates using operational modal analysis – preliminary findings, Proceedings of the International Ocean and Polar Engineering Conference, ISOPE (2018).

[13] M. Vigsø, R. Brincker, C. Georgakis, Identifying wave loads during random seas using structural response, Proceedings of the International Ocean and Polar Engineering Conference, ISOPE (2019).

[14] D. Fallais, S. Voormeeren, E. Lourens, Vibration-based identification of hydrodynamic loads and system parameters for offshore wind turbine support structures, Proceedings of Deep Sea Offshore Wind R&D Conference, EERA DeepWind 2016, Trondheim, Norway (2016).

[15] N. Perisic, P. H. Kirkegaard, U. Tygesen, Load identification of offshore platform for fatigue life estimation, Structural Health Monitoring 5 (2014) 99–109.

[16] N. Giansante, R. Jones, N. Calapodas, Determination of in-flight helicopter loads, Journal of the American Helicopter Society 27 (3) (1982) 58–64.

[17] F. Bartlett, W. Flannelly, Model verification of force determination for measuring vibratory loads, Journal of the American Helicopter Society 24 (2) (1979) 10–18.

[18] W. Flannelly, F. Bartlett, T. Fonsberg Jr, Laboratory Verification of Force Determination, A Potential Tool for Reliability Testing, Kaman Aerospace Corporation, Old Windsor Road, Bloomfield Conn., 1977.

[19] M. Vigsø, R. Brincker, C. Georgakis, The effect of modal truncation and spatial distribution in load identification, Proceedings of the International Operational Modal Analysis Conference, iomac (2019).

[20] B. Dobson, E. Rider, A review of the indirect calculation of excitation forces from measured structural data, Proceedings of the Institution of Mechanical Engineers, Part C: Mechanical Engineering Science 204 (1990) 69–75.
[21] N. R. Maddox, On the number of modes necessary for accurate response and resulting forces in dynamic analyses, Journal of Applied Mechanics 42 (1975) 516–517.
[22] K. Stevens, Force identification problems - an overview, Proceedings of the SEM Spring Conference on Experimental Mechanics (1987) 838–844.
[23] M. Vigsø, M. Tarpø, J. Hansen, R. Brincker, C. Georgakis, Scenario based approach for load identification, Proceedings of the International Modal Analysis Conference, IMAC (2018) 117–125.
[24] M. Luhar, H. Nepf, Wave-induced dynamics of flexible blades, Journal of Fluids and Structures 61 (2016) 20–41.
[25] H. Bredmose, J. Mariegaard, B. Paulsen, B. Jensen, S. Schløer, T. Larsen, ..., A. Hansen, The wave loads project, DTU Wind Energi E (2013) No. 0045.
[26] H. Bredmose, P. Slabiak, L. Sahlberg-Nielsen, F. Schlütter, Dynamic excitation of monopiles by steep and breaking waves. experimental and numerical study, Proceedings of the 32nd International Conference on Ocean, Offshore and Arctic Engineering, ASME (2013).
[27] S. Neelamani, V. Sundar, C. Vendhan, Dynamic pressure distribution on a cylinder due to wave diffraction, Ocean Engineering 16 (1989) 343–353.
[28] H. Akyildiz, Experimental investigation of pressure distribution on a cylinder due to the wave diffraction in a finite water depth, Ocean Engineering 29 (2002) 1119–1132.
[29] F. Huarte, P. Bearman, J. Chaplin, On the force distribution along the axis of a flexible circular cylinder undergoing multi-mode vortex-induced vibrations, Journal of Fluids and Structures 22 (2006) 897–903.
[30] F. H. L. Gonzales, Numerical prediction of the modal response of flexible cylinders in cross-flow with a current dependent form of damping, Journal of Fluids and Structures 18 (2013) 370–380.
[31] S. Anagnostopoulos, Dynamic reponse of offshore platform to extreme waves including fluid-structure interaction, Engineering Structures 4 (1982) 179–185.
[32] M. Vigsø, T. Kabel, M. Tarpø, R. Brincker, C. Georgakis, Operational modal analysis and fluid-structure interaction, Proceedings of the International Conference on Noise and Vibration Engineering, ISMA (2018).
[33] R. Brincker, C. Ventura, Introduction to Operational Modal Analysis, John Wiley and Sons, Ltd, Chichester, West Sussex, UK, 2015.
[34] J. Morison, M. O'Brien, J. Johnson, S. Schaaf, The force exerted by surface waves on piles, Petroleum Transactions, American Institute of Mining Engineers (1950) 149–154.
[35] S. Hashemi, M. Saadatpour, M. Kianoush, Dynamic behavior of flexible rectangular fluid containers, Thin-Walled Structures 66 (2013) 23–38.
[36] H. Vold, J. Knudrat, G. Rocklin, R. Russell, A multi-input modal estimation algorithm for mini-computers, SAE International Congress and Exposition Technical Paper 820194 (1982).
[37] M. Khatibi, M. Ashory, A. Malekjafarian, Mass-stiffness change method for scaling of operational mode shapes: Experimental results, Proceedings of the International Modal Analysis Conference, IMAC (2010) 1569 – 1577.
[38] R. Brincker, P. Andersen, A way of getting scaled mode shapes in output only modal testing, Proceedings of the International Modal Analysis Conference, IMAC (2003) 141–145.
[39] N. Barltrop, A. Adams, Dynamics of fixed marine structures, 3rd Edition, Butterworth-Heinemann, UK, 1991.
[40] J. O'Callahan, P. Avitabile, R. Riemer, System equivalent reduction expansion process, Proceedings of the International Modal Analysis Conference, IMAC (1989).
[41] R. Allemang, The modal assurance criterion (MAC): Twenty years of use and abuse, Journal of Sound and Vibration 37 (2003) 14–23.

Chapter 14

Breaking waves

Paper VIII

"Estimating loads from breaking waves using operational modal analysis"

Michael Vigsø and Christos Georgakis

Published in Proceedings of the 39th International Conferences on Ocean, Offshore and Arctic Engineering, OMAE, Fort Lauderdale, FL, 2020
(Peer reviewed)

This chapter presents a study of loads from breaking waves on a cantilever structure. The load identification is performed using the frequency domain method and the content is exclusively an application study. The author has performed the ideation, experiments, analysis and the writing of the paper. The paper has been formatted with minor grammatical adjustments to suit this thesis.

Estimating loads from breaking waves using operational modal analysis

Michael Vigsø[a,*], Christos Georgakis[a]

[a] *Aarhus University, Inge Lehmanns Gade 10, 8000 Aarhus, Denmark*

Abstract

Load effects from breaking waves on offshore structures may be a driving point for the design. It is hence important to assess the likelihood of occurrence along the magnitude of the loads in the event of an impact. Traditionally, loads are predicted using wave theory combined with a load model such as the Morison. This paper features an alternative approach in determining the loads from wave breaking. It is demonstrated how the structural response can be used for (indirectly) estimating the magnitude of the loads caused by wave breaking. The theory is applied to an experimental setup in a wave flume, where a flexible model is subjected to loads from breaking waves. The dynamic properties are mapped using operational modal analysis and it is consequently shown that the loads can be identified using the vibration measurements.

Keywords: Load identification, Breaking waves, Operational modal analysis

1. Introduction

Breaking waves may be a severe loading scenario for marine structures. Local pressures may rise to extreme levels and, thus, drive the design of the structures. Unexpected, large, and breaking waves is a frightening phenomenon to those at sea. History provides cases of fatal consequences, for instance, the COSL Innovator in 2015 at the Troll field in Norway, where a large wave slammed into the rig and caused severe damages and the death of one worker [1].

Now, much uncertainty exists when predicting the magnitude of the loads caused by breaking waves. The type of wave breaking (plunging, spilling, collapsing, or surging) is the most critical for the loads. However other things like air entrapment or fluid/structure interaction may also be important for the load effects. When determining the loads from breaking waves one may seek help from the guidelines by the Norske Veritas (DNV), which yields the possibility of adding a slamming term to the Morison equation. The amplitude coefficients for the slamming load are subjected to much disagreement among the community of fluid research. The estimates are most often derived from laboratory experiments where scaling effects of unknown magnitude may alter the application for large, deep water structures. Now, another approach is to monitor the response of a structure. Using load identification techniques, it is then possible to decode the response and thus obtaining an estimate on the external loads.

Allow this paper to showcase the principles of load identification in the context of breaking waves. The theory used is already presented by Vigsø et al. [2–5], thus, leaving the main focus

*Corresponding author

Email addresses: mvigso@eng.au.dk (Michael Vigsø), cg@eng.au.dk (Christos Georgakis)

Published in the Proceedings of the Int'l Conferences on Ocean, Offshore and Arctic Engineering, OMAE
This paper has been formatted to suit this thesis *March 2020*

of this study to be application in the case of impulsive loads caused by the wave breaking. Load identification from breaking waves has also been studied by Maes et al. [6] although they used another method compared to what will be presented in this paper, [7]. They solved the inverse problem in state space using a Kalman filter and pressure sensors were used to locally derive the pressure distribution in the splash zone.

2. Theory

The method used in this study is referred to as "transfer path analysis" or "pseudo inverse method" [8]. It operates in the frequency domain which means that the complete response history must be recorded before the load identification can be performed. The theory for establishing the load identification algorithm corresponds to the one given by Vigsø et al. [2]. We assume linear behavior and establish a relation between the input and the output for any discrete frequency, also known as a frequency response function (FRF).

$$\underline{Y}(\omega) = \underline{\underline{H}}(\omega)\underline{F}(\omega) \tag{1}$$

where, $\underline{F}(\omega)$ is the load, $\underline{\underline{H}}(\omega)$ is the frequency response function, and $\underline{Y}(\omega)$ is the response measurements, all given in the frequency domain. Once the response function is established, its inverse can be premultiplied to the response and, thus, leaving an estimate on the input. The inverse operation is sensitive in nature and care must be taken to avoid unphysical estimates [3, 9]. To mitigate, the load is first split into a spatial distribution $\underline{S_p}$ and a scaling function $g(\omega)$. Assuming that only a single load source is present, we have:

$$\underline{F}(\omega) = \underline{S_p}\, g(\omega) \tag{2}$$

Here, it is provided that the spatial distribution is time-independent. The expression for the load is now substituted into Eq. (1) and an estimate for the scaling function is:

$$\hat{g}(\omega) = \left(\underline{\underline{H}}(\omega)\underline{S_p}\right)^{\dagger} \underline{Y}(\omega) \tag{3}$$

Finally, the load estimate is obtained as:

$$\underline{\hat{F}}(\omega) = \underline{S_p}\, \hat{g}(\omega) \tag{4}$$

The spatial distribution of wave loading is complex when wave breaking is present. Different components will be present at the same time i.e., inertia forces, drag forces, along with the slamming. Many load models may be used in this case, but to simplify, we assume that the load is effectively approximated as a concentrated point load near the mean water level.

3. Experimental setup

A cantilever plexiglass model is placed in a wave flume at the facilities at LASIF in Marseille. Figure 1 shows a picture from the experimental setup. The pile of the model is Ø150 mm and the topside measures $400 \times 200 \times 200$ mm. The mean water level in the tank is 900 mm and the model extends 585 mm above the waterline. The model is equipped with 16 uniaxial accelerometers, where eight are facing the incoming wave and the remaining eight are facing in the transverse direction. The accelerometers are distributed along the inside of the pile and in the corners of the topside. These are used for measuring the impact response of the structure and for system identification

purposes. The accelerometers used are Brüel & Kjær type 4508-002 1000 mV/g. The sensor layout is sketched in Figure 2, but the reader may refer to [10], or [11] for the detailed description of the model. A wave gauge is positioned next to the model such that the wave profile can be documented. The model is placed on a six-DOF ATI load cell and fixed to the base of the flume. The load cell is only used for verifying the estimated loads. The experiment is split into two consecutive stages; system identification and later load identification from the breaking waves.

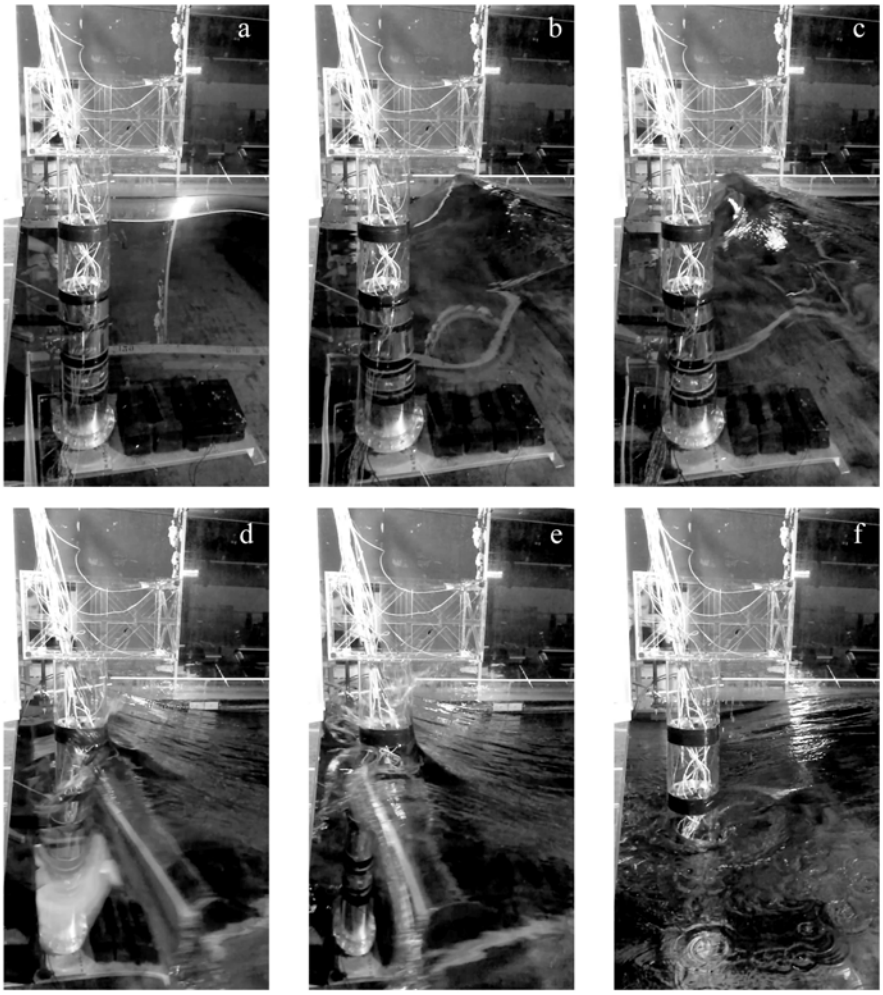

Figure 1: Pictures from the wave impact experiment. Picture a - f is given in chronological order and show the structure before, during, and after the wave impact. The points a - f are also represented in Figure 3, which shows the associated time history of the surface elevation.

3.1. System identification

The frequency response function is synthesized from a set of modal parameters. The modal parameters may be obtained from experimental system identification techniques. In this case, the concepts of operational modal analysis (OMA) are utilized [12, 13]; Artificial random excitation is hence applied (brush strokes to the structure and sloshing of the water) and the structural acceleration response is recorded. The sampling rate is 2 kHz and the response is recorded for 15 minutes. The response spectrum is shown in Figure 2 in terms of singular values. The modes are extracted using time-domain poly reference [14] using a sliding band-pass filter. The detailed system identification procedure is given in paper [10]. By default, OMA does not yield any scaling information on the mode shapes. This is important information for establishing the response function. To mitigate this, a finite element (FE) model is established and updated. The FE model will now aid the scaling and interpolation of the modes shapes obtained from the OMA.

Table 1: Modal parameters used in establishing the frequency response function with an uncertainty bound for each parameter. The mode shapes are mass normalized yielding unity modal mass.

Mode		1	2	3	4	5
Natural frequency [Hz]	±2%	8.37	8.66	37.6	40.3	47.0
Damping ratio [%]	±40%	2.7	2.1	4.9	3.7	4.4
Modal mass [-]	±10%	1	1	1	1	1

Table 1 summarizes the modal parameters extracted from the data. We do acknowledge poles in the spectra above 50 Hz, but the identification of the modes is unstable and a confident match with the FE model is not possible. We, hence, truncate the response function to include modes up till 50 Hz, which covers five. The modal parameters given in Table 1 are naturally subjected to some variations/uncertainties. The consequences in load estimates due to an uncertain system

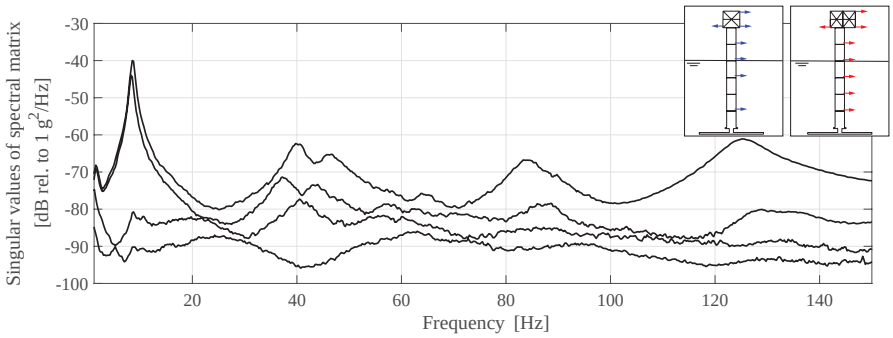

Figure 2: Singular values of the spectral density from random loading. The four first singular values are shown. The spectrum is computed using the Welsh averaging technique with a block size of 2^{13} samples corresponding to four seconds. The sketches in the upper right corner show the distribution of the sensors. Red are facing the incoming wave and the blue are facing in transverse direction.

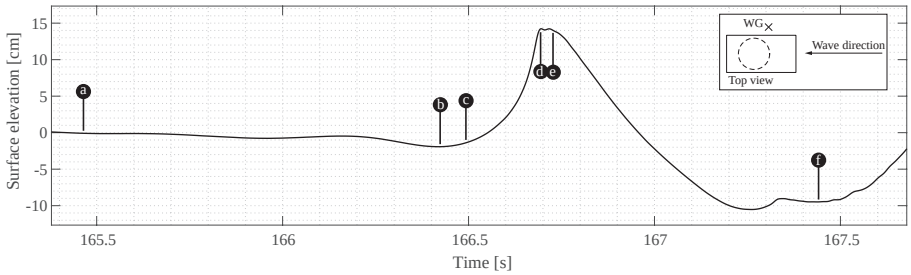

Figure 3: Wave profile during the breaking wave impact. The surface elevation is measured by a wave gauge (WG) located at the front of the pile with transverse offset of 20 cm as indicate in the top right corner. The points *a* - *f* corresponds to the pictures given in Figure 1.

identification should instinctively be evaluated. The second column shows the span which we assess should be evaluated. The FRF matrix is thus established for any combination and a load is identified for each. This more computationally demanding, but it provides a valuable confidence band around the load estimate.

3.2. Breaking wave

The wavemaker is set to generate a series of focused waves in order to provoke wave breaking. The identification algorithm presumes no information on the type of waves and the details of the wave generation is also omitted. The time history of the surface elevation may be seen in Figure 3. The exact position of the wave gauge is at the pile front with a transverse centreline offset of 20 cm. This means that wave runup on the pile is not visible in the time history.

4. Results

Since the model is somewhat flexible, the input load will differ from the load measured by the load cell at the base. I.e., when the model experiences an impulse, the model will afterward oscillate at its natural frequencies. These oscillations are interpreted as external loads by the load cell at the base. The estimated input load is thus immediately transferred to the base using the FE model to provide an estimated reaction force. It is now possible to compare the estimated reaction force to the measured reaction force. The comparison is given in Figure 4, which shows the shear force and overturning moment. The solid black line provides the measurements from the load cell while the grey area spans the indirect estimate given variations in the modal parameters. Please be aware that the load cell data is unfiltered. This maintains the harmonic disturbance in the signal at 50 Hz as seen by the ripples, especially in the shear force.

Firstly, we note that the overall trend is captured by the indirect method. The uncertainty in modal parameters provides a range for the load estimate and it is seen that the estimate easily varies with $\pm 20\%$ given our confidence in the system identification. The identification of the load in the wake of the impulse is not as well determined. After the time of impact, the reaction force estimate is much dominated by the properties of the FE model. If the transfer function between the input forces and the reaction forces contains errors this yields more uncertainty to the conclusions.

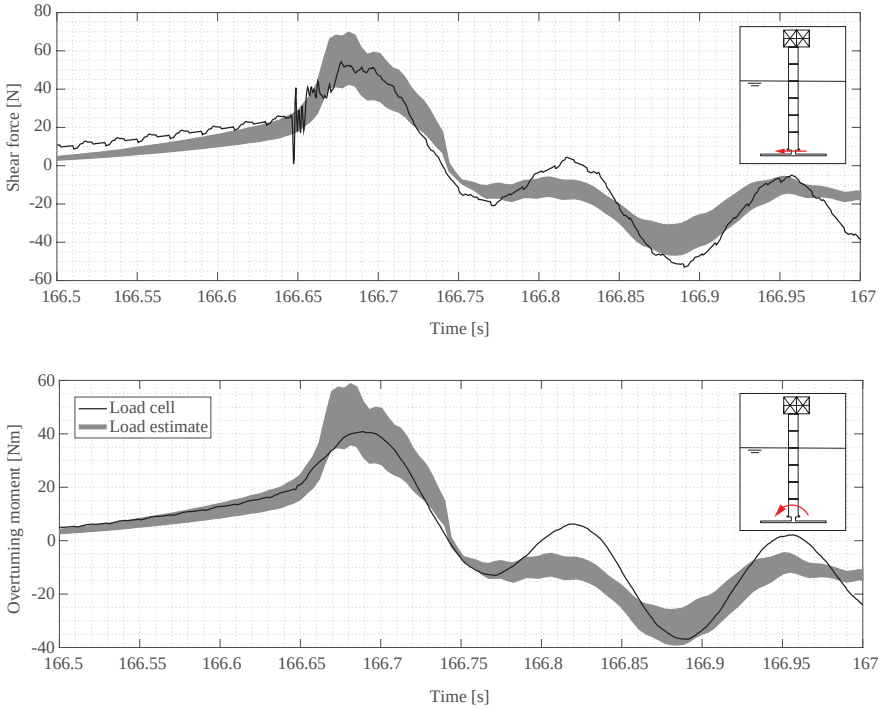

Figure 4: Identified mudline loads during wave impact. The solid black lines are the direct measurements from the load cell while the grey areas indicate the estimates using the indirect method and accounting for the uncertainty in the modal parameters.

5. Conclusion

We have applied a linear theory on a case that is likely nonlinear and shown that the load can be indirectly approximated using the system response. A uncertainty bound on the load estimate is shown. The uncertainty band originates from variations in the estimated modal parameters; here the natural frequencies were varied by ±2%, the damping ratio was varied by ±40%, and finally, the scaling of the mode shapes was varied by ±10%. Although it is not directly seen from the presented results, the variations of the mode shape scaling showed the most significant effect in the load estimate.

Acknowledgments

The authors acknowledge the funding received from the Centre for Oil and Gas – DTU/Danish Hydrocarbon Research and Technology Centre (DHRTC). The help from co-workers at Aarhus University; Thomas Kabel, Marius Tarpø, and Julie Kristoffersen is also much appreciated.

References

[1] I. Ollestad, T. Andersen, N. Orma, S. Zachariassen, Investigation of an incident with fatal consequences on coslinnovator, 30 december 2015, Petroleumstilsynet report (2016) Activity number 418005005.

[2] M. Vigsø, J. Kristoffersen, R. Brincker, C. Georgakis, Indirect wave load estimates using operational modal analysis – preliminary findings, Proceedings of the International Ocean and Polar Engineering Conference, ISOPE (2018).

[3] M. Vigsø, R. Brincker, C. Georgakis, Evaluating the effect of modelling errors in load identification using classical identification methods, Shock and Vibration 2019 (2019) Article ID 9490760.

[4] M. Vigsø, R. Brincker, C. Georgakis, The effect of modal truncation and spatial distribution in load identification, Proceedings of the International Operational Modal Analysis Conference, iomac (2019).

[5] M. Vigsø, M. Tarpø, J. Hansen, R. Brincker, C. Georgakis, Scenario based approach for load identification, Proceedings of the International Modal Analysis Conference, IMAC (2018) 117–125.

[6] K. Maes, W. Weijtjens, E. de Ridder, G. Lombaert, Inverse estimation of breaking wave loads on monopile wind turbines, Ocean Engineering 163 (2018) 544–554.

[7] K. Maes, Q. Smyth, G. De Roeck, G. Lombaert, Joint input-state estimation in structural dynamics, Mechanical Systems and Signal Processing 70-71 (2016) 445–466.

[8] W. Flannelly, F. Bartlett, T. Fonsberg Jr, Laboratory Verification of Force Determination, A Potential Tool for Reliability Testing, Kaman Aerospace Corporation, Old Windsor Road, Bloomfield Conn., 1977.

[9] K. Stevens, Force identification problems - an overview, Proceedings of the SEM Spring Conference on Experimental Mechanics (1987) 838–844.

[10] M. Vigsø, T. Kabel, M. Tarpø, R. Brincker, C. Georgakis, Operational modal analysis and fluid-structure interaction, Proceedings of the International Conference on Noise and Vibration Engineering, ISMA (2018).

[11] M. Vigsø, R. Brincker, C. Georgakis, Identifying wave loads during random seas using structural response, Proceedings of the International Ocean and Polar Engineering Conference, ISOPE (2019).

[12] R. Brincker, C. Ventura, Introduction to Operational Modal Analysis, John Wiley and Sons, Ltd, Chichester, West Sussex, UK, 2015.

[13] C. Rainieri, G. Fabbrocino, Operational modal analysis of civil engineering structures, Springer, New York, 2014.

[14] H. Vold, J. Knudrat, G. Rocklin, R. Russell, A multi-input modal estimation algorithm for mini-computers, SAE International Congress and Exposition Technical Paper 820194 (1982).